

UC Berkeley

UC Berkeley Electronic Theses and Dissertations

Title

Elemental and isotopic separation by diffusion in geological liquids

Permalink

<https://escholarship.org/uc/item/1ms755hj>

Author

Watkins, James Mervin

Publication Date

2010

Peer reviewed|Thesis/dissertation

Elemental and isotopic separation by diffusion in geological liquids

by

James Mervin Watkins

A dissertation submitted in partial satisfaction of the

requirements for the degree of

Doctor of Philosophy

in

Earth and Planetary Science

in the

Graduate Division

of the

University of California, Berkeley

Committee in charge:

Professor Donald J. DePaolo, Chair

Professor Michael Manga

Professor M. Steven Shackley

Fall 2010

Elemental and isotopic separation by diffusion in geological liquids

Copyright 2010

by

James Mervin Watkins

Abstract

Elemental and isotopic separation by diffusion in geological liquids

by

James Mervin Watkins

Doctor of Philosophy in Earth and Planetary Science

University of California, Berkeley

Professor Donald J. DePaolo, Chair

Chemical speciation in molten silicates is of broad interest for understanding thermodynamic and transport properties. However, it is difficult to elicit the nature of dissolved species in silicate liquids, let alone the role that speciation plays in the diffusion process. This dissertation is about chemical diffusion in silicate melts; it combines experiments with isotopic measurements to infer the physical mechanisms of cation diffusion and the role that diffusion plays in producing isotope effects in nature.

Diffusion of calcium (Ca) between natural volcanic liquids in diffusion-couple experiments leads to $^{44}\text{Ca}/^{40}\text{Ca}$ variations of ca. 5‰ due to a mass dependence of Ca diffusion coefficients. The efficiency of Ca isotope separation by diffusion varies with bulk liquid composition and depends also on the magnitude and direction of aluminum (Al) gradients. Some Ca isotopic fractionations seem to arise solely from gradients in Al. These observations indicate that isotopic discrimination by diffusion reflects the mass difference between isotopically-substituted molecular species, and there is evidence for at least one Ca-bearing and one Ca-Al-bearing diffusing species in the volcanic liquids that were studied. The inferred existence of a Ca-Al complex is consistent with the additional observation that Ca diffuses slowly since it is inferred that Ca atoms interact strongly with their nearby Si and Al “solvent” molecules in the liquid.

The third part of this thesis describes Ca diffusion between silicate liquids of simplified chemical composition. Results from these experiments indicate that the efficiency of diffusive separation of Ca isotopes is systematically related to the normalized diffusivity - the ratio of the mobility of the cation (D_{Ca}) to the mobility of the liquid matrix (D_{Si}). A similar dependence is observed for Fe, Li, and Mg isotopes, and in aqueous solutions. This empirical result provides a predictive tool that can be used to understand diffusive isotopic effects in a wide variety of geologic environments and a basis for a more comprehensive theory of isotope separation in liquid solutions. A conceptual model is presented for the relationship between diffusivity and liquid structure that is consistent with available data.

To my family back in Wisconsin.

Contents

List of Figures	v
List of Tables	x
1 General introduction	1
1.1 General introduction to chemical diffusion	2
1.1.1 The diffusion equation	2
1.1.2 Comment on Fick's first law	3
1.2 Diffusion in different media	4
1.2.1 Diffusion in a gas	4
1.2.2 Diffusion in a liquid	5
2 Diffusion-controlled crystal growth in natural rocks	7
2.1 Introduction	7
2.2 Background	7
2.2.1 Qualitative description of spherulite growth	7
2.3 Samples	8
2.3.1 Sample descriptions	8
2.3.2 Sample preparation	9
2.4 FTIR measurements	10
2.5 Results	10
2.6 Interpretation	11
2.7 Model for spherulite growth	12
2.8 Results	13
2.9 Discussion	16
2.9.1 On what timescales do spherulites grow?	17
2.9.2 At what degree of undercooling do spherulites begin to grow?	19
2.9.3 Do spherulites grow below the glass transition?	19
2.9.4 Why doesn't spherulite growth lead to runaway heating?	21
2.9.5 Why are spherulites spherical?	21
2.10 Conclusions	22

3	Isotope separation by diffusion in natural molten silicates	23
3.1	Introduction	23
3.1.1	Speciation and silicate liquid structure	23
3.1.2	Diffusion in silicate liquids	24
3.2	Mass dependence on diffusivity	25
3.2.1	Diffusive isotopic fractionation	26
3.3	Approach	26
3.4	Results	27
3.4.1	Major-element diffusion profiles	27
3.4.2	Calcium isotope profiles	32
3.5	Discussion	32
3.5.1	Interpretation of basalt-rhyolite experiments	32
3.5.2	Interpretation of ugandite-rhyolite experiments	34
3.5.3	Diffusive isotopic fractionation and speciation	35
3.6	Theoretical Considerations	37
3.6.1	General multicomponent diffusion model	37
3.6.2	Simplified multicomponent diffusion model	38
3.7	Numerical calculations	39
3.7.1	Model versus measured oxide profiles	39
3.7.2	Model versus measured Ca isotope profiles	41
3.8	Discussion	42
3.8.1	Physical explanation for mass discrimination by diffusion	42
3.8.2	Silicate melt structures and diffusing components	44
3.8.3	Thermal gradients in the experiments	45
3.9	Summary and conclusions	47
3.10	Code validation	48
4	Isotope separation by diffusion in synthetic molten silicates	50
4.1	Introduction	50
4.2	Experiments	50
4.3	Results	51
4.3.1	Major-element diffusion profiles	51
4.3.2	Ca and Mg isotope profiles	51
4.4	Analysis	56
4.4.1	Model for the elemental diffusion profiles	56
4.4.2	Model for the isotope ratio profiles	57
4.4.3	Comparison between model and measured isotope profiles	57
4.5	Discussion	58
4.5.1	Isotope separation by diffusion in silicate melts	58
4.5.2	Isotope separation by diffusion in aqueous solutions	58
4.6	Summary and conclusions	61
4.7	Comment on multicomponent diffusion models	62

5	Chemical, Tracer and Soret diffusion	65
5.1	Isotopic exchange superimposed on chemical diffusion	65
5.1.1	Modification of Fick's first law for isotopes	65
5.1.2	Model results	66
5.1.3	Summary and future work	67
5.2	The mechanisms of chemical versus tracer diffusion	68
5.3	Soret isotope separation in a silicate liquid	69
5.3.1	Experiments	69
5.3.2	Theory	70
5.3.3	What causes isotope separation in a thermal gradient?	71
A	Diffusion couple experiments	73
A.1	Sample assembly	73
A.2	Piston cylinder	74
A.3	Electron microprobe analysis	74
A.4	Wafering and dissolution	76
A.5	Cation exchange columns	77
A.6	Mass spectrometry	77
B	User's guide to the Ca double spike	78
B.1	Running your sample in the mass spectrometer	78
B.2	Spike subtraction	80
C	Additional data tables	83

List of Figures

2.1	(a) Photograph of a spherulitic obsidian from Tequila volcano. Spherulites ranging in size from 1.0 to 8.0 mm in diameter are distributed homogeneously throughout. (b) CL image showing fibrous alkali-feldspar crystals enclosed by oblate cristobalite masses within an individual spherulite. (c) Thin section image showing spherulites cross-cutting subtle flow bands.	9
2.2	FTIR transect between two spherulites of different size illustrating the expulsion of water into the surrounding melt or glass during spherulite growth.	10
2.3	Cathodoluminescence image of a spherulite (upper left) and electron microprobe element maps on the same spherulite. Dark regions correspond to relatively low concentrations. Note the relative enrichment in Na and depletion in K and Si at the spherulite boundary.	11
2.4	Schematic diagram summarizing the 1D spherulite growth and water diffusion model. The dark black line represents actual (time-dependent) water concentration and the dashed line represents the initial water concentration. The width of the vertical gray bar represents an increase in spherulite radius from R to $R + dR$, and the water within this region is removed and fluxed into the new boundary at $R + dR$. The model assumes perfectly efficient water expulsion.	12
2.5	Model calculations showing the evolution of water concentration away from spherulite boundaries assuming two different spherulite growth laws. Note the different scales for the x- and y-axes. The linear growth law (2.5a) leads to narrow profiles with a progressive build-up of water at the edge of the spherulite whereas the diffusion-controlled growth law (2.5b) leads to wider profiles and nearly steady values of water concentration at the spherulite edge.	14
2.6	Comparison between measured water concentration profiles and model calculations. Figures (a) and (c) show results for two different spherulites using a linear growth law (i.e., $u_r \sim D_{OH}$). Figures (b) and (d) show results for two different spherulites using a diffusion-controlled growth law (i.e., $u_r \sim (D_{OH}/t)^{1/2}$). Clearly, indistinguishable results can be obtained using either growth law for a spherulite of given radius. Dark curves represent initial conditions for post-growth model (see text).	15

2.7	Data versus model profiles after post-growth diffusion of water is included. Initial conditions are bold profiles in figure 2.6. The timescales correspond to the lower bound of the experimentally determined D_{OH} (i.e., $T=400^{\circ}\text{C}$; Zhang and Behrens, 2000). The same duration of post-growth diffusion provides comparable fits to the profiles for both large and small spherulites, which is expected assuming a common closure temperature for spherulites from a given locality.	16
2.8	Time required to grow a spherulite of given radius at various fixed temperatures assuming a diffusion-controlled growth law and using a proportionality constant of $a=1.0$. The shaded region at the top of the graph encompasses the range of possible ages for the host obsidian (Lewis-Kenedi et al., 2005) and the dashed line indicates the size of the largest spherulite analyzed in this study. For spherulites to grow appreciably on cooling timescales, they must form at temperatures above about 400°C	18
2.9	Temperature-dependence of diffusivities for various chemical species in obsidian. Dark line for H_2O is from equation 12 in Zhang and Behrens (2000) and grey lines for H_2O are from obsidian hydration experiments (see Freer, 1981). All other lines are from the compilation by Freer (1981). The main point is that major- and trace-element diffusivities appear to be insensitive to the glass transition in melts of rhyolitic composition (region shown in grey).	20
3.1	Major-element diffusion profiles from a basalt-rhyolite diffusion couple experiment. The asymmetry in each of profiles reflects a decrease in diffusivity with increasing silica content. Overall, the profiles are relatively simple, monotonic diffusion profiles except Na_2O and Al_2O_3 , which exhibit uphill diffusion. Note the Al_2O_3 contrast between starting liquids is small.	29
3.2	Major-element diffusion profiles from a ugandite-rhyolite diffusion couple experiment. Overall, the profiles are more complicated than those in figure 3.1, with uphill diffusion of Na_2O , K_2O , and CaO (see inset) due to, presumably, diffusive coupling to Al_2O_3 . Note that unlike the basalt-rhyolite experiments, there is a large Al_2O_3 gradient going from right to left.	30
3.3	Ca isotope profiles from three sets of experiments. The initial interface between starting liquids is given by the vertical dashed line. The grey horizontal bar shows the initial isotopic composition. Corresponding CaO diffusion profiles are shown below each plot. The high values of $\delta^{44}\text{Ca}$ in the rhyolite in (e) and (f) is interpreted as evidence for diffusive coupling of Ca to Al (see text).	31
3.4	Major-element profiles from each of the diffusion couple experiments cast in terms components used in the Bottinga and Weill (1972) viscosity model. The post-run profiles for CaO and CaAl_2O_4 are compared to the Ca isotope profiles presented in figure 3.3. In the basalt-rhyolite experiments (3.4a and 3.4b), the gradients in both Ca species are unidirectional whereas in the ugandite-rhyolite experiments (3.4c and 3.4d), there are gradients in Ca species in both directions.	36

3.5	Model versus measured diffusion profiles for SiO_2 , Al_2O_3 , and CaO from the three sets of experiments. The model assumes three-component diffusion and includes diffusive coupling of CaO to Al_2O_3 . Diffusivity parameters for the model profiles are given in each panel in units of mm^2/s . Despite the relative simplicity of the model, a reasonable fit can be achieved for CaO , which is then used to generate the Ca isotopic profiles in figure 3.6.	40
3.6	Model versus measured Ca isotope profiles for the three sets of experiments (labeled a, b, and c). Despite the relative simplicity of the model, the overall shape and magnitude of the fractionations are reproduced. The disagreement between model and data on the rhyolite end of the capsules may be related to the misfit in the same region of the Al_2O_3 profiles in figure 3.5.	41
3.7	Diffusivities of Ca , Al , and Si (calculated from our diffusion model) as a function of melt viscosity (calculated using the model of Bottinga and Weill (1972) across a ugandite-rhyolite diffusion couple. Also shown are D_{Li} (from RDDW) and D_{Eyring} (using $l=1.4\text{\AA}$, the diameter of an oxygen anion) for the same experimental conditions. The ratio of D_{cation}/D_{Eyring} depends on the cation as well as melt viscosity, which can explain the diffusive isotopic fractionations observed (see text).	43
3.8	Results from an experiment to test temperature gradients across the diffusion couples. Basalt was placed in the experimental assembly exactly the way the basalt-rhyolite couples were. The data suggest that a the linear gradients we observe in the mafic end of our diffusion couples can be attributed in part to a temperature gradient of about 15°C (Richter et al., 2008). There are no discernible isotopic fractionations due to temperature gradients in the top half of the capsules (i.e., the rhyolite end).	46
3.9	Model results using two different numerical algorithms: (1) finite differences coded by J.M. Watkins using MATLAB and (2) Lattice Boltzmann (LB) coded by C. Huber using C++. These solutions were obtained using a slightly different input parameter for the Ca-Al coupling: $D_{Ca-Al}=5 \mu\text{m}^2/\text{s}$ in the finite differences solution versus $D_{Ca-Al}=7 \mu\text{m}^2/\text{s}$ in the LB solution. This small discrepancy aside, the numerical schemes give nearly indistinguishable results, which we take to be a strong indication that the model results in this chapter are accurate.	49
4.1	Diffusion profiles of major cations between two simplified molten silicate compositions along the albite-anorthite (AB-AN) join as measured by electron microprobe. Solid lines are model diffusion profiles and the dashed lines represent the starting concentrations and initial condition for the diffusion model. The diffusivity D_i of each of the major cations is roughly constant across the diffusion couple, as evidenced by the observed symmetry in each of the profiles about the initial interface between starting liquids.	52
4.2	Same as figure 4.1 except here the starting compositions lie along the albite-diopside (AB-DI) join.	53

4.3	Calcium and magnesium isotope separation by diffusion in the AB-AN and AB-DI experiments. The initial isotopic composition is denoted by the grey horizontal line. Solid lines are model isotope profiles used to quantify the efficiency of isotope separation E , which is related to the ratio of isotopic diffusion coefficients (D_2/D_1).	54
4.4	The observed relationship between the efficiency of isotope separation E and the mobility of the diffusing cation (D_{cation}) relative to the mobility of the liquid matrix ($D_{solvent}$) in aqueous solutions (small symbols) and silicate liquids (large symbols). The subscript solvent refers to H ₂ O in aqueous solutions and Si (or SiO ₂) in silicate liquids.	59
4.5	Results from model diffusion profiles that allow for diffusive coupling between chemical components. Two different sets of parameters (i.e., diffusion matrices) provide nearly identical fits to the measured profiles. This shows that the solution to the multicomponent diffusion problem based on one experiment is under-constrained.	63
5.1	Model results using equation 5.6 applied to the AB-AN and AB-DI diffusion couples. The dashed line is for $D_s=D_c$ and results are indistinguishable from those in chapter 4. The solid line shows the result for $D_s \geq D_c$, which can explain the observation that isotope ratio profiles are more “evolved” than elemental diffusion profiles.	67
5.2	Calcium isotope separation in a temperature gradient. The bulk composition of the system is tholeiitic basalt. The isotopic composition, which was uniform prior to the experiment, varies systematically with temperature. The dashed curve is a third-order polynomial fit with no physical basis and only serves as a guide to the eye.	70
A.1	Photograph of a post-run diffusion couple. The example here is from experiment DF-8.	74
A.2	Three parallel microprobe transects from DF-5 showing that chemical diffusion in our experiments can be regarded as unidimensional.	75
A.3	Photograph of a post-run diffusion couple after sectioning. The example at left is from experiment DF-8. The wafers on the right are actually from DF-2 but are representative of typical wafers; three wafers are shown to illustrate how their physical appearance varies in going from the felsic to the mafic liquid. These three wafers still have a lot of graphite from the capsule affixed to them. Much of this graphite is removed by abrasion prior to dissolution of the silicate portion.	76
B.1	Screen capture showing the raw data for two different Ca isotope ratios. . .	79
B.2	Screen capture showing the corrected data for two different Ca isotope ratios. This is a “good run” in which the corrected 40/44 values show uniform scatter about a mean value.	79

B.3 Screen capture showing the corrected data for two different Ca isotope ratios. This is a "bad run" in which the corrected 40/44 values vary systematically with time. 80

List of Tables

3.1	Differences in isotope diffusivities for Ca, Mg, and Li obtained in basalt-rhyolite interdiffusion experiments.	26
3.2	Bulk composition and Ca isotope composition of starting materials used in diffusion couple experiments. Major element abundances are shown both in terms of oxide components as well as in terms of species used in the Bottinga and Weill (1972) viscosity model.	28
3.3	Initial and experimental conditions for each of the diffusion-couple experiments. RB2 and RB3 are from RDDW. All other experiments were performed in this study.	28
3.4	Ca isotope measurements measured on wafers from four diffusion couple experiments. Also shown are the distances along the Ca diffusion profile associated with the center point of each wafer. Uncertainties in $\delta^{44}\text{Ca}$ are within $\pm 0.15\%$	33
4.1	Targeted versus measured bulk compositions of starting materials used in diffusion couple experiments. The difference between the target (or calculated) compositions and those measured by electron microprobe is not an important factor for the purposes of this study.	51
4.2	Ca and Mg isotope compositions measured on post-run diffusion couples.	55
4.3	Values and associated references used in the compilation of figure 4.4.	60
C.1	FTIR data for the two spherulitic glasses discussed in chapter 2.	84

Acknowledgments

I first need to thank my three Ph.D. advisors: Don DePaolo, Michael Manga, and Chris Huber. Don, I have so many things for which to thank you, but most of all your generosity. In short, you provided every resource possible to make my dissertation a success. Michael, you have so many qualities that I admire, not least of which is your availability and responsiveness on a day-to-day basis. For this, among other things, I am tremendously grateful. Chris, you were my officemate, best friend, and a tower of support and advice throughout graduate school. Thank you so much for everything.

During the past 5 years I had many interactions with the other occupants of the fourth floor of McCone Hall. Marilyn Saarni was invaluable in making things (including my computer) run smoothly. Tom Owens and Shaun Brown were patient and taught me everything I know in the chemistry lab. Tim Teague helped me in all things related to sample preparation as well as geology arts & crafts. Kent Ross did much of the electron probe work in this thesis and shared his vast knowledge of world history and music history. Matt Cataleta helped design and build several experimental apparatuses. I also appreciate the stimulating discussions I've had with my other committee members Steve Shackley and Chi Wang.

I want to mention how grateful I am to the administrative staff in our department. Margie Winn, Micaelee Ellswhyte, and Dawn Geddes were always helpful, professional, and a pleasure to chat with.

I feel indebted to many of the graduate students who overlapped with me at Berkeley. Those in the Manga and DePaolo groups were particularly influential. Karrie Weaver and Megan Smith showed me the ropes early on. Mark Wenzel and Vicky Lee set an example for how to be a professional. Sarah Brownlee and Leah Morgan were true friends from the very beginning. Chris Huber, Gilead Wurman, Claudia Jones, Jenny Druhan, Brook Peterson, and Laura Nielsen were wonderful officemates. And finally Leif Karlstrom, Max Rudolph, Edwin Kite, and Amanda Thomas - your office was a reliable haven for sharing scientific curiosity.

I want to acknowledge the post-docs Justin Simon, Joe Dufek, and Tim Creyts, each of whom set an example that I aspire to follow. Thank you for your generosity with your time and expertise. In addition I learned a lot from working on projects with three undergraduates: Jian Gong, Charles Kang, and Matt Gonzales. The enjoyment I received from all of these collaborations cemented my desire to become an academic.

Lastly I wish to thank my family back in Wisconsin (to whom this thesis is dedicated) for constant love, support, and understanding.

Chapter 1

General introduction

This thesis is aimed at understanding the physical mechanisms of one of the most fundamental processes in nature: chemical diffusion. Chemical diffusion is the net transport of mass through the random motions of countless atoms, molecules and particles. It is in reality an enormously complicated physical process, and yet, theories that describe chemical diffusion can be relatively straightforward. The first chapter serves two purposes: (1) it introduces chemical diffusion from a theoretical perspective and (2) it poses the important questions which serve to motivate the studies discussed in chapters 3, 4 and 5.

Chapter 2 illustrates a practical aspect of diffusion modeling. In the simplest case (and after initial and boundary conditions are defined) a measured diffusion profile depends on two things: (1) the mobility of a chemical component and (2) time. Therefore, with knowledge of the mobility, or diffusivity, of a chemical component, simplified models of chemical diffusion can be used to infer timescales of geological processes. In chapter 2 we show how measured water diffusion profiles and known diffusion rates of water in rhyolitic glasses can be used to determine timescales of spherulite growth in obsidian. This work was published in *Contributions to Mineralogy and Petrology*.

Chapters 3 and 4 focus on the actual physical mechanisms of diffusion and isotope separation in silicate melts. Over the past decade, there has been growing interest in measuring isotopic variations in a wider variety of elements and with ever-increasing spatial resolution. Interpreting these subtle variations has required a closer look at the actual physical mechanisms of isotope separation and how molecular-scale transport processes affect isotopic distributions. In chapter 3 we show that chemical diffusion can give rise to measurable isotope fractionations because random molecular motions are mass dependent. The results show that the magnitude of this mass dependence seems to depend on how strongly coupled a cation is to its nearest neighbors as it diffuses through the liquid. In other words, the apparent mass difference between isotopes seems to reflect the mass difference between isotopically-substituted chemical species. The implication is that isotope diffusion can be used as a tool for inferring speciation and diffusion mechanisms in silicate liquids. This work was published in *Geochimica et Cosmochimica Acta*.

Chapter 4 is a study in which we measured diffusive isotopic fractionations in simplified chemical systems. These experiments revealed a clear relationship between cation mobility versus liquid matrix mobility and the efficiency of isotope separation by diffusion

for a given cation. From this study we obtained several things: (1) a mechanistic explanation for the variability of isotope separation by diffusion in terms of liquid structure and dynamics at the molecular scale, (2) an explanation for the observation that isotope separation by diffusion is more efficient in silicate liquids at 1450°C than in aqueous solutions at 25°C, and (3) predictions for where to expect large diffusive isotope effects in nature. This work is currently under review in *Geochimica et Cosmochimica Acta*.

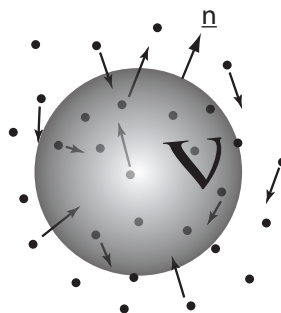
Chapter 5 discusses several additional interesting aspects of chemical diffusion that arose from our interpretation of the experimental results in chapters 3 and 4. This chapter is one of several works in progress and it touches upon some of the future directions of this research.

1.1 General introduction to chemical diffusion

1.1.1 The diffusion equation

The chemical diffusion equation describes the change in concentration of a chemical species with time at a particular location. There are many ways to derive the diffusion equation and the version that follows is both accessible and succinct¹

Imagine an arbitrary volume V of any shape and within which there are an arbitrary number of particles. By mass balance we can say that the change in concentration, or



amount, of particles within this volume V is equal to the flux of particles integrated over the surface of the volume. That is,

$$\int_V \frac{\partial C}{\partial t} dV = - \oint_S (J \cdot \bar{n}) dS, \quad (1.1)$$

where dV is a volume element, J is the flux (particles/cm²/s) and \bar{n} is the unit vector normal to and pointing outward from the surface of the volume. This model does not account for changes in material properties as diffusion occurs such as chemical reactions, which may create (autocatalytic reactions) or remove (non-autocatalytic reactions) any number of the particles.

¹This derivation is from Prof. Zohdi's notes for his finite-element methods course.

Using the divergence theorem the surface integral can be made into a volume integral:

$$\int_V \frac{\partial C}{\partial t} dV = - \int_V \nabla \cdot J dV, \quad (1.2)$$

The next step is to rewrite the flux J in terms of concentration. In non-equilibrium thermodynamics, a chemical flux is driven by a gradient in chemical potential. Since chemical potential is not easy to measure, gradients in chemical potential are often approximated as gradients in concentration. Fick's first law is an oft-adhered-to approximation that states that the fluxes and forces are linearly related (see next section); that is

$$J = -D\nabla C. \quad (1.3)$$

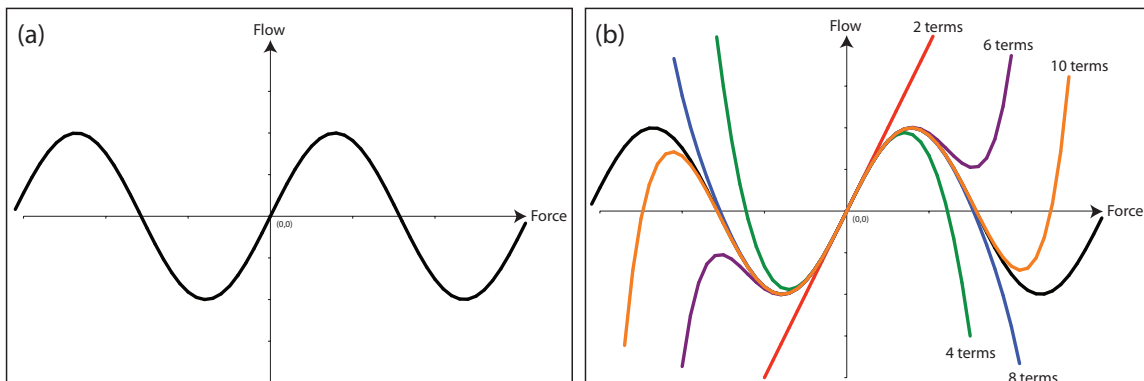
The constant of proportionality D is the diffusion coefficient. Here it is written as a scalar quantity, which assumes that the diffusing medium is isotropic. Finally, since dV in equation 1.2 is arbitrary, we can remove the integral signs to get a differential equation:

$$\frac{\partial C}{\partial t} = \nabla \cdot (D \cdot \nabla C) \quad (1.4)$$

This is the general form of the chemical diffusion equation, which serves as a basis for discussion in subsequent chapters. It assumes that fluxes and forces are linearly related, and in this case, the force is assumed to be the gradient in the concentration of the diffusing species. The diffusion coefficient D is where most of the complication comes into play when modeling the process of chemical diffusion. The diffusivity of an element or species depends on the physical properties of the diffusing medium; it may vary spatially in an anisotropic material and it may depend on variables such as temperature, pressure and chemical composition. Most models of diffusion invoke simplifying assumptions about D in order to make diffusion problems manageable. In each of the subsequent chapters, the simplifying assumptions on D are discussed according to each problem.

1.1.2 Comment on Fick's first law

Fick's first law postulates that the flux (or flow) of a quantity is linearly related to a driving force. In practice, this empirical relationship holds when driving forces are relatively small, and from a theoretical standpoint, the linear relationship between flows and forces can be recognized as a truncation of higher order terms in a Taylor series expansion. To see how this works, we begin with the statement that in general the functional form relating flows and forces could be anything. For illustrative purposes, consider a relationship that is sinusoidal (figure 1.1.2a). The curve passes through the origin because *when there is no force there is no flow*. Let's also take it for granted that any function can be written as an infinite sum of terms in a power series. The idea behind the Taylor series is that for a continuous function that can be infinitely differentiated, you can approximate this function in the neighborhood of a known coordinate pair using a fewer number of terms. The Taylor series expansion about the point (0,0) is



$$f(x) = f(0) + f'(0)x + \frac{f''(0)}{2!}x^2 + \frac{f'''(0)}{3!}x^3 \dots \quad (1.5)$$

The exact value of $f(x)$ at $x=0$ is given by the first term. For $x^2 \ll 1$, the first two terms provide a good approximation to $f(x)$ because close to $(0,0)$ the function is approximately linear. The extent to which the Taylor series is a good approximation of $f(x)$ can be seen by comparing the true function to the Taylor series result using an increasing number of terms from equation 1.5. Figure 1.1.2b shows that the higher order terms become increasingly important for evaluating $f(x)$ as you move further and further from $(0,0)$. The main point of all this is that *close to equilibrium, flows and forces are linearly related* (to a good approximation).

1.2 Diffusion in different media

1.2.1 Diffusion in a gas

The simplest treatment of diffusion applies to particles in an ideal (i.e., monatomic and dilute) gas because the identity of the diffusing species is known and potential interactions between particles can be neglected. From kinetic theory the diffusivity is the product of the root mean speed v_{rms} of particles and the mean free path l between collisions:

$$D = l \cdot \underbrace{\left(\frac{RT}{m} \right)^{1/2}}_{v_{rms}} \quad (1.6)$$

Note that the diffusivity is inversely proportional to the square root of particle mass. Since diffusivity varies inversely with mass, one might anticipate from equation 1.6 that lighter isotopes diffuse faster than heavy isotopes, and by an amount that is proportional to the square root of the inverse mass ratio between the isotopes:

$$\frac{D_2}{D_1} = \left(\frac{m_1}{m_2} \right)^{1/2} \quad (1.7)$$

This is referred to as the *square-root-of-mass law* and is only valid, strictly speaking, for systems in which the assumptions of kinetic theory apply. In other systems such as non-dilute gases, liquids, and solids, equation 1.7 serves as a useful reference from which to compare the mass dependence on diffusion coefficients.

1.2.2 Diffusion in a liquid

In condensed systems chemical diffusion is much more complicated. The main reason for this is that the diffusing species have non-negligible potential interactions with their nearest neighbors. Intermolecular potentials are theoretically complex because they depend on the shape and rotation of molecules whose identities are often unknown or are not well defined in liquid systems. In cases where the diffusing species are unknown, it is customary to define a basis set of chemical components and to allow the flow of a component to be driven by concentration gradients in any of the other components. That is, we can (and should) generalize Fick's first law as

$$J_i = \sum_{j=1}^{n-1} D_{ij} \nabla C_j \quad (1.8)$$

where D_{ij} is a matrix of diffusion coefficients. If diffusion of each component i is independent of all other components, then D_{ij} is a diagonal matrix. Generally, this is not the case and the off-diagonal elements of D_{ij} specify the extent of diffusive coupling between the chosen components.

In contrast to theories of diffusion in an ideal or dilute gas, there is no simple scaling law that describes the relationship between diffusivity and mass in liquids because isotopic substitution affects translational and rotational mobility differently (McLaughlin, 1960). When rotation does not contribute significantly to momentum transfer, molecular motion can be described by the linear equation of motion

$$F_\alpha = m \frac{dv_\alpha}{dt} \quad (1.9)$$

where F_α is the net central force acting on a molecule due to the potential field of its neighbors and v_α is the linear velocity. For spherically symmetric molecules such as cyclohexane and methane, and in which only central forces matter, equation 1.9 is expected to adequately describe molecular motion and the ratio of transport coefficients has been shown to be in agreement with the square root of mass law (i.e., equation 1.7; McLaughlin (1960)).

If, on the other hand, rotational motion is important for momentum transfer, the angular equation of motion is needed for describing changes in momentum due to non-central forces:

$$G_\alpha = I_{\alpha\beta} \frac{d\omega_\beta}{dt}, \quad (1.10)$$

where G_α is the torque on a molecule from forces due to neighboring atoms, $I_{\alpha\beta}$ is the inertia tensor, and ω_β is the angular velocity. Rotational and translational motions of molecules are not independent; a change in torque can arise from translation of a nearby molecule or a change in force can arise from rotation of nearby molecule. This translational-rotational coupling is associated with molecular anisotropy and its effect on transport coefficients depends on intermolecular forces, which are theoretically complex (Weingartner et al., 1989). Broadly speaking, however, it is clear that isotope substitution will affect m and $I_{\alpha\beta}$ differently and the resulting influence on diffusion coefficients will vary depending on the importance of rotational motion. For anisotropic molecules such as water and benzene, the ratio of isotope-specific molecular diffusion coefficients does not agree with the square root of mass law but is in better agreement when mass is replaced with the principal moments of inertia (McLaughlin, 1960; Weingartner et al., 1989):

$$\frac{D_2}{D_1} = \left(\frac{I_{1,\gamma}}{I_{2,\gamma}} \right)^{1/2}, \quad (1.11)$$

where γ refers to any of the principal axes x, y, and z.

In cases where equation 1.11 might apply, one first needs detailed information on the structure of the diffusing species. The principal moments of inertia are known or can be calculated for simple organic molecules (e.g., Holz et al., 1996) and self diffusion NMR measurements show that the isotope effect on translational and rotational diffusion tends more towards a square-root of the moment of inertia law when there is strong translation-rotation coupling (e.g., Holz et al., 1996; Hardy et al., 2001). In silicate liquids, however, the picture is not as simple because diffusion occurs through rapid chemical exchanges instead of molecular mechanisms of motion (Stebbins, 1995). In other words, even the very definition of speciation in silicate liquids is ambiguous. This motivates two questions: (1) what are the diffusing species in silicate liquids? and (2) what kinds of isotope effects can arise due to diffusion in silicate liquids? These questions, which are addressed in chapters 3, 4 and 5, pertain to understanding the material properties of silicate melts and understanding isotope variability due to mass-dependent processes in nature.

Chapter 2

Diffusion-controlled crystal growth in natural rocks

2.1 Introduction

This chapter is an example of how a diffusion model can be used to infer the timescale of a geological process. In geochemistry this is a relatively common practice. In this study, however, we also show how diffusion data and modeling can be used to infer crystal growth mechanisms.

2.2 Background

Spherulites are polycrystalline solids that develop under highly non-equilibrium conditions in supercooled liquids (Keith and Padden, 1963). Natural spherulites are commonly found in rhyolitic obsidian and have evoked the curiosity of petrologists for more than a century (e.g., Judd, 1888; Cross, 1891). Over the past several decades, numerous studies on spherulite morphology (Keith and Padden, 1964a; Lofgren, 1971a), kinetics of spherulite growth (Keith and Padden, 1964b; Lofgren, 1971b), disequilibrium crystal growth rates and textures (Fenn, 1977; Swanson, 1977), and field observations (Martin and McKinney, 1988; Swanson et al., 1989; Manley and Fink, 1987; Manley, 1992; Davis and McPhie, 1996; MacArthur et al., 1998) have shed light on the conditions and processes behind spherulite nucleation and growth. Despite the long-standing interest, several fundamental questions persist. For example: On what timescales do natural spherulites form? At what degree of undercooling do spherulites begin to grow? Can spherulites grow below the glass transition? Why doesn't spherulite growth lead to runaway heating? And, why are spherulites spherical? In this chapter, we revisit these questions and contribute a new quantitative approach for estimating spherulite growth rates.

2.2.1 Qualitative description of spherulite growth

Spherulites in rhyolitic obsidian are composed primarily of alkali feldspar and SiO_2 polymorphs. Spherulites are often mm-scale, but are known to range from submicroscopic

to m-scale (e.g., Smith et al., 2001). They may be randomly distributed and completely isolated, or nucleate preferentially to form clusters or trains (e.g., Davis and McPhie, 1996). Within a deposit, spherulitic textures and relationships may vary widely owing to local differences in emplacement temperature, flow depth, cooling rate, and surface hydrology (Manley, 1992; MacArthur et al., 1998). Despite these complexities, the fact that spherulites occur almost exclusively in glasses seems to require conditions that yield slow nucleation rates yet relatively rapid crystal growth rates.

As a melt cools below the liquidus temperature (T_{eq}) for a given crystalline phase, an energy barrier must be overcome in order for the new phase to nucleate and grow. Just below T_{eq} , this energy barrier is finite and decreases with decreasing temperature. A certain amount of undercooling is always necessary to nucleate a solid phase (Carmichael et al., 1974), where the degree of undercooling (ΔT) is the difference between the equilibrium temperature (T_{eq}) and the actual magmatic temperature T . In siliceous lavas, atomic mobility is sluggish and large ΔT can be achieved prior to nucleation. Once nucleation does occur, crystal growth proceeds and crystal growth rates are dictated by a competition between the magnitude of ΔT and atomic mobility.

Large undercoolings promote rapid crystallization, but are also associated with lower magmatic temperatures and slower elemental diffusivities. For crystals growing from a melt or glass of different composition, crystal growth rates are limited by the ability of melt components to diffuse towards or away from the crystallizing front. In the case of spherulites, it has been shown that certain major- and trace-elements are rejected by crystallizing phases and concentrated at the spherulite-glass interface (Smith et al., 2001).

Since the mineral phases that compose rhyolitic spherulites are nominally anhydrous, water is also rejected from the crystalline region. Among incompatible melt species, water is perhaps the most extensively studied because of its pronounced effects on magma viscosity and major-element diffusion coefficients. As a result, methods for determining water concentrations in rhyolitic glasses have been developed over the past 25 years (e.g., Stolper, 1982; Newman et al., 1986; Zhang et al., 1997) using Fourier Transform Infrared Spectroscopy (FTIR). The goal of our measurements is to use FTIR to resolve water concentration gradients at the spherulite-glass interface with high spatial resolution (see Castro et al., 2005) to better understand the growth history of spherulites.

2.3 Samples

2.3.1 Sample descriptions

The spherulites analyzed in this study are from a hand sample of a rhyolitic vitrophyre that lies in the Quaternary Tequila volcanic field, western Mexico. Lavas that range in composition from basalt to rhyolite surround an andesite stratovolcano that formed about 200 kyr ago (Lewis-Kenedi et al., 2005). The rhyolites and obsidian domes are among the earliest erupted units, ranging in age from 0.23 to 1.0 Ma (Lewis-Kenedi et al., 2005).

Figure 2.1 is a photograph of the obsidian hand sample used in this study. The matrix is a dark glass that has not undergone post-magmatic hydration. It contains some visible but subtle flow bands reflecting shear flow of magmatic parcels containing variable

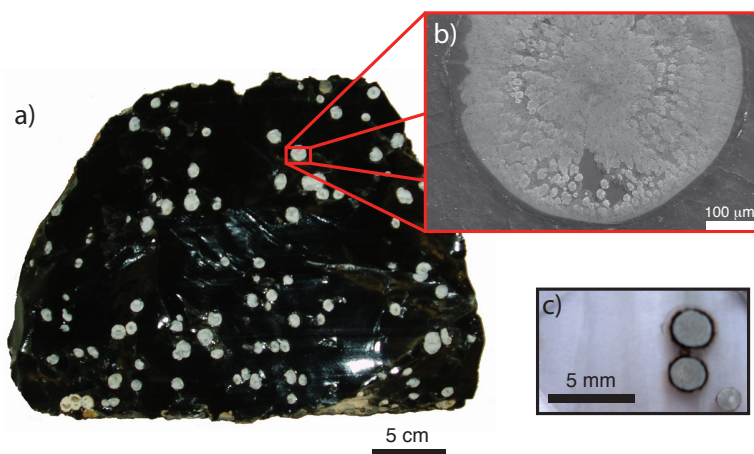


Figure 2.1: (a) Photograph of a spherulitic obsidian from Tequila volcano. Spherulites ranging in size from 1.0 to 8.0 mm in diameter are distributed homogeneously throughout. (b) CL image showing fibrous alkali-feldspar crystals enclosed by oblate cristobalite masses within an individual spherulite. (c) Thin section image showing spherulites cross-cutting subtle flow bands.

microlite content (Gonnermann and Manga, 2003). Isolated, light grey spherulites cross-cut flow bands and exhibit a range of sizes that are distributed homogeneously.

Individual spherulites are host to three crystalline phases: $\sim 55\text{-}65\%$ (by volume) feldspar fibers, $\sim 30\text{-}40\%$ oblate cristobalite masses, and $<1\%$ Fe- and Ti-oxides. The feldspar fibers are arranged in a radial habit about a central nucleus and are enclosed by the cristobalite masses. X-ray diffraction patterns indicate the feldspar is some form of alkali feldspar, but an exact determination could not be made. There is also a significant amount of void space due to the $\sim 10\%$ volume contraction associated with crystallization, which we neglect in our calculations.

2.3.2 Sample preparation

Four rectangular billets ($\sim 21\text{ mm} \times 38\text{ mm}$) of spherulitic obsidian were cut from a hand sample (figure 2.1) to be prepared for FTIR analysis. Each billet was ground down until at least one spherulite was sectioned through its center. The surface with the spherulite was polished to $\sim 0.25\ \mu\text{m}$. The polished surface was mounted on a glass slide with epoxy and the billet was cut to a thickness of $\sim 300\ \mu\text{m}$. The grinding and polishing procedure was repeated on the opposite surface to obtain a doubly polished wafer. Each of the samples was of uniform thickness ($\pm < 5\%$ as determined by a digital micrometer with a precision of $\pm 2\ \mu\text{m}$) so that infrared absorption data could be compared throughout the sample. Polished surfaces were necessary for minimizing infrared scattering and obtaining quality absorbance data.

2.4 FTIR measurements

Water concentration measurements were made by synchrotron-source Fourier Transform Infrared Spectroscopy (FTIR) at the Advanced Light Source at Lawrence Berkeley National Laboratory. The instrument used was a Nicolet 760 FTIR spectrometer interfaced with a Spectra-Tech Nic-Plan IR microscope capable of spot sizes of 3-10 μm (Martin and McKinney, 1998). Transects were oriented perpendicular to spherulite rims and measurements were made on the surrounding glassy matrix. Total water concentrations were determined from the intensity of the 3570 cm^{-1} peak (Newman et al., 1986), which reflects the abundance of hydrous species (X_{OH}) including molecular water (HOH). Hereafter, we refer to all hydrous species collectively as “water”. Analytical error is estimated to be $\pm 0.005\text{ wt.}\%$ based on repeated measurements.

2.5 Results

Figure 2.3 shows data from a transect between two adjacent spherulites. At the rim-matrix interface of each spherulite, there is a local maximum in water content that decreases with distance into the surrounding matrix to background levels ($\sim 0.115\text{ wt.}\%$ in this case). Similar profiles were measured on seven spherulites ranging in size from 1.7 mm to 5.2 mm in diameter.

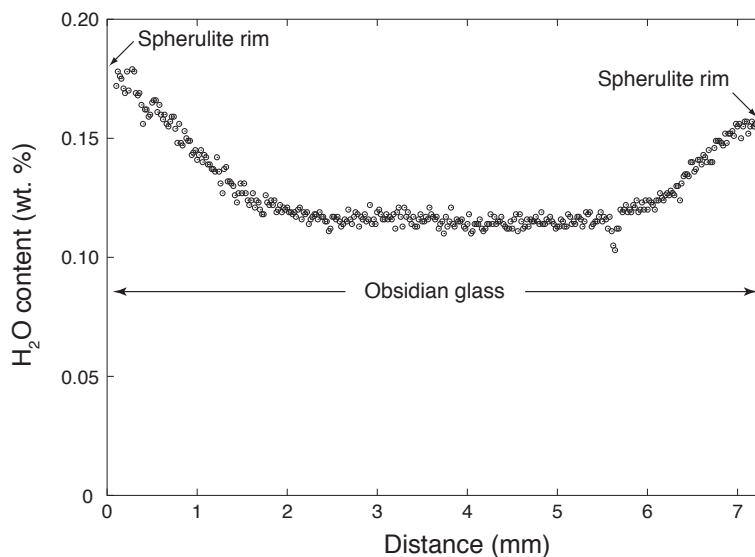


Figure 2.2: FTIR transect between two spherulites of different size illustrating the expulsion of water into the surrounding melt or glass during spherulite growth.

One of the samples was also analyzed using a Cameca SX-51 electron microprobe to characterize major-element variations. Due to the similarity in bulk composition between spherulites and their host, gradients in major elements could not be resolved quantitatively

within detection limits. However, qualitative variations are resolved through detailed WDS x-ray mapping for three major elements taken on an individual spherulite (figure 2.3). A close look at the rim-matrix interface reveals a relative depletion in crystallizing components K and Si and concomitant enrichment in Na.

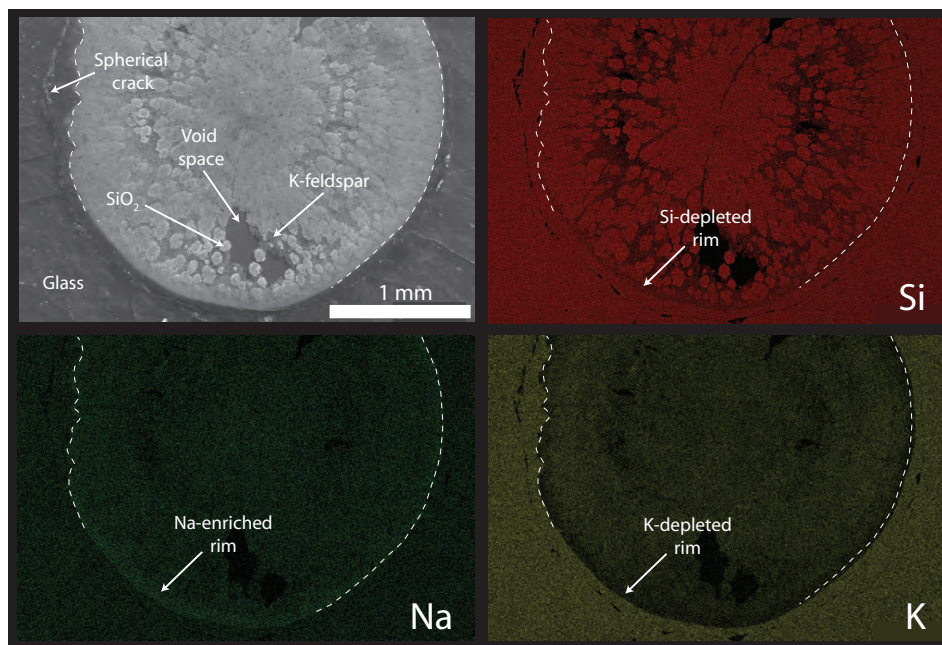


Figure 2.3: Cathodoluminescence image of a spherulite (upper left) and electron microprobe element maps on the same spherulite. Dark regions correspond to relatively low concentrations. Note the relative enrichment in Na and depletion in K and Si at the spherulite boundary.

2.6 Interpretation

Spherulite growth from a liquid or glass of different composition requires diffusion of crystal-forming components, which become depleted over diffusive lengthscales around the crystallizing region. Figures 2.2 and 2.3 clearly illustrate this process and confirm that impurities are not trapped within crystals or interstitial voids. The outward rejection of water induces a concentration gradient down which water diffuses into the surrounding matrix, resulting in profiles like that shown in figure 2.2.

For four of the seven spherulites analyzed, the data were clean enough to demonstrate that greater than 95% of the water from the volume occupied by the spherulite could be accounted for in the water diffusion profile. This is noteworthy because it provides a stoichiometric relationship between the moles of water removed and moles of sanidine (or cristobalite) crystallized within the spherulite volume, thus allowing water rejection and diffusion to be used as a proxy for spherulite growth.

2.7 Model for spherulite growth

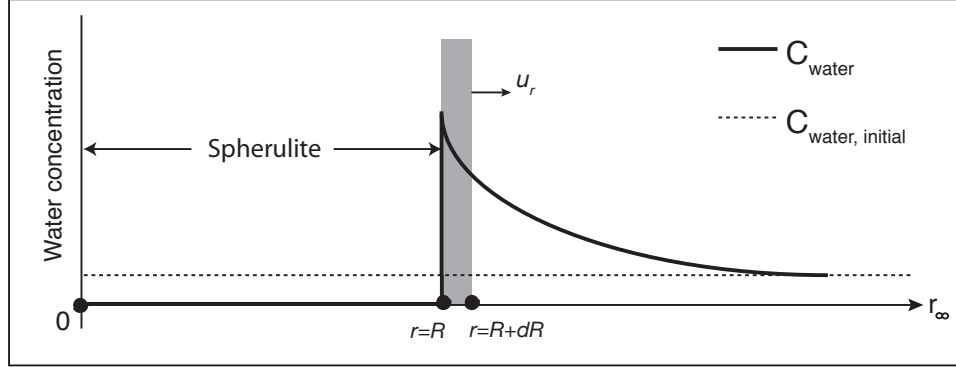


Figure 2.4: Schematic diagram summarizing the 1D spherulite growth and water diffusion model. The dark black line represents actual (time-dependent) water concentration and the dashed line represents the initial water concentration. The width of the vertical gray bar represents and increase in spherulite radius from R to $R + dR$, and the water within this region is removed and fluxed into the new boundary at $R + dR$. The model assumes perfectly efficient water expulsion.

With each increment of spherulite growth, a known amount of water is expelled ahead of the advancing crystalline front. In this way, water diffusion into the matrix is in competition with the propagating spherulite boundary. Here we present a model that tracks the expulsion and diffusion of water during spherulite growth in the reference frame of the expanding spherulite rim. In this reference frame, profiles such as those in figure 2.2 can be modeled by solving numerically the advection-diffusion equation:

$$\frac{\partial C}{\partial t} - \bar{u} \cdot \nabla C = \nabla \cdot (D_{OH} \cdot \nabla C) \quad (2.1)$$

where C is the concentration of water, \bar{u} is the velocity of the growing interface, and $D_{OH}(C, T, P)$ is the diffusivity of water in rhyolite melt or glass. Zhang and Behrens (2000) showed that $D_{OH}(C, T, P)$ varies linearly with water concentration at low total water contents (less than about 2 wt.%), and we account for this effect in our model. However, we do not include variations in $D_{OH}(C, T, P)$ with temperature and pressure - a simplifying assumption discussed later. Taking advantage of the spherical symmetry of spherulites, equation 2.1 can be simplified and expressed as a function of the radial distance only:

$$\frac{\partial C}{\partial t} - u_r \frac{\partial C}{\partial r} = D_{OH}(r) \left(\frac{\partial^2 C}{\partial r^2} + \frac{2}{r} \frac{\partial C}{\partial r} \right) \quad (2.2)$$

where D_{OH} is updated at the beginning of each timestep. The velocity of the interface u_r ($u_r = dR/dt$ where R is the radius of the spherulite) is given by the choice of spherulite growth law. Keith and Padden (1963) found experimentally that at constant temperature,

spherulites in polymer liquids generally grow according to a linear growth law whereby u_r is constant and R scales linearly with time:

$$u_r = n \cdot D_{OH} \quad (2.3)$$

where n is a free parameter that represents the competition between spherulite growth and water diffusion.

A possible alternative is a diffusion-controlled growth law (Granasy et al., 2005), whereby the radius scales with time as $t^{1/2}$:

$$u_r = a \cdot \left(\frac{D_{OH}}{t} \right)^{1/2}, \quad (2.4)$$

where a is a free parameter analogous to n in the linear case.

The appropriate boundary conditions for this problem are: (1) fixed concentration of water far from the growing interface and (2) time-dependent concentration of water at the rim-matrix interface that is related to the flux of water expelled during each increment of growth. The second boundary condition is implemented by ensuring mass conservation:

$$\int_{R(t)}^{R_\infty} (C(r, t) - C_\infty) r^2 dr = \frac{1}{3} C_\infty R(t)^3 \quad (2.5)$$

where $C(r, t)$ is the concentration of water at a distance r from the center of the spherulite, R is the spherulite radius, and C_∞ represents the background concentration of water at some distance R_∞ into the surrounding matrix. Equation 2.5 states that the water represented under the diffusion profile is equal to 100% of the water that once occupied the spherulite volume. Any difference between these two values is used to update $C(R, t)$ after each timestep so that the equality is true.

2.8 Results

The temporal evolution of model water concentration profiles depends strongly on the choice of growth law. Figure 2.5 compares model profiles using both the linear growth law (2.5a) and the diffusion-controlled growth law (2.5b) as a function of spherulite radius (i.e., time). In the linear regime, the concentration of water at the growing spherulite boundary increases progressively with time. This is a consequence of the spherical geometry, wherein the volume of water expelled increases with each (constant) growth increment dR . By contrast, in the diffusion-controlled regime, the diffusion of water counterbalances the time-dependent growth increment dR such that the concentration of water at the spherulite boundary remains relatively constant with time.

Figure 2.6 compares model results to measured profiles from two spherulites of different size. The two profiles are representative of those measured in this study and include the largest and smallest spherulites examined. Figures 2.6a and 2.6b correspond to data from a spherulite of radius 0.86 mm, while figures 2.6c and 2.6d correspond to data

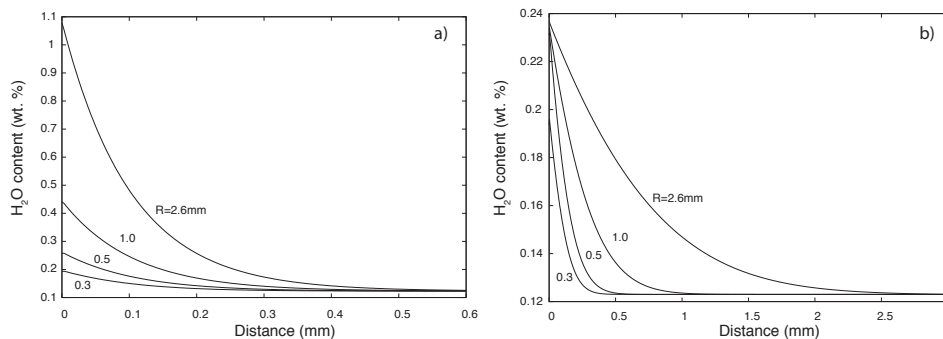


Figure 2.5: Model calculations showing the evolution of water concentration away from spherulite boundaries assuming two different spherulite growth laws. Note the different scales for the x- and y-axes. The linear growth law (2.5a) leads to narrow profiles with a progressive build-up of water at the edge of the spherulite whereas the diffusion-controlled growth law (2.5b) leads to wider profiles and nearly steady values of water concentration at the spherulite edge.

from a spherulite of radius 2.6 mm. The figures on the left (2.6a and 2.6c) assume linear growth whereas the figures on the right (2.6b and 2.6d) assume diffusion-controlled growth. Although the agreement between model curves and measured profiles is not very satisfying, it is clear that an equally good (or, for that matter, equally poor) fit can be achieved using either growth law for a given spherulite. However, there is one important distinction between the two growth models. Figures 2.6a and 2.6c show that a smaller coefficient n is required in going from the smaller to the larger spherulite. In contrast, figures 2.6b and 2.6d show that a larger coefficient a is required in going from the smaller spherulite to the larger spherulite. The significance of this is discussed in the next section.

A striking feature of all measured water concentration profiles is the flattening they exhibit near the rim-matrix interface, which may be attributed to post-growth diffusion of water. In order to account for this effect, we use the bold profiles from figure 2.6 as the initial condition for the post-growth model, and, as $dR/dt=0$, equation 2.2 reduces to the diffusion equation with no-flux boundary conditions (i.e., water is not allowed to diffuse back into the spherulite). Results are summarized in Figure 2.7 for the small and large spherulite. The duration of post-growth diffusion (in years) depends on D_{OH} (i.e., temperature), and the values quoted in figure 2.7 arbitrarily assume $T=400^{\circ}\text{C}$. A lower temperature would simply require more prolonged post-growth diffusion in order to achieve an identical fit. The two most important points that arise from figure 2.7 are: (1) the agreement between measured and model profiles is markedly improved with inclusion of post-growth diffusion, and (2) the same duration of post-growth diffusion is required to fit profiles for both large and small spherulites.

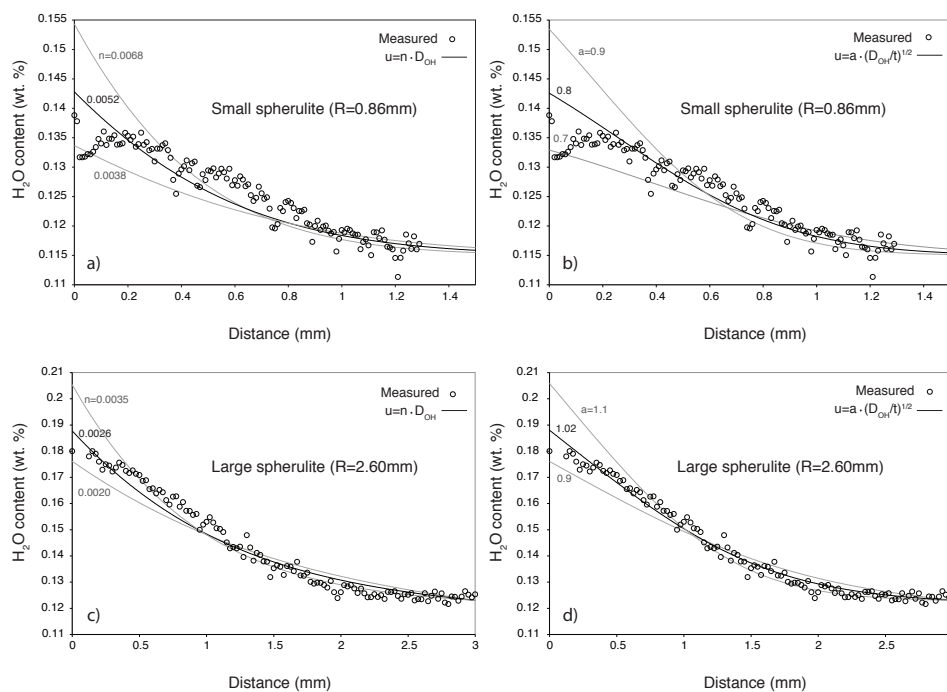


Figure 2.6: Comparison between measured water concentration profiles and model calculations. Figures (a) and (c) show results for two different spherulites using a linear growth law (i.e., $u_r \sim D_{OH}$). Figures (b) and (d) show results for two different spherulites using a diffusion-controlled growth law (i.e., $u_r \sim (D_{OH}/t)^{1/2}$). Clearly, indistinguishable results can be obtained using either growth law for a spherulite of given radius. Dark curves represent initial conditions for post-growth model (see text).

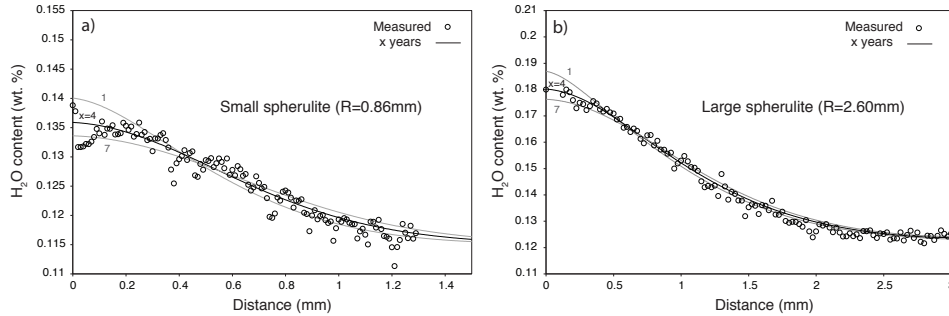


Figure 2.7: Data versus model profiles after post-growth diffusion of water is included. Initial conditions are bold profiles in figure 2.6. The timescales correspond to the lower bound of the experimentally determined D_{OH} (i.e., $T=400^{\circ}\text{C}$; Zhang and Behrens, 2000). The same duration of post-growth diffusion provides comparable fits to the profiles for both large and small spherulites, which is expected assuming a common closure temperature for spherulites from a given locality.

2.9 Discussion

The distinction between linear and diffusion-controlled growth laws is important as it pertains to several questions presented earlier about natural spherulites. Keith and Padden (1964b) studied spherulite growth kinetics under isothermal conditions in a range of polymer liquids and found that impurities often become trapped in the interstices of the crystalline region. Under these circumstances, impurities do not influence subsequent crystal growth and spherulite growth rates are linear in time (Keith and Padden, 1964b). However, the linear growth law breaks down when rejected species are sufficiently mobile. That is, when diffusion of impurities occurs on the same timescale as crystal growth rates, the concentration of impurities at the crystalline interface increases progressively. As a consequence, spherulite growth rates decrease with spherulite size owing to the reduction in local concentrations of crystallizing components. Hence, we interpret the observation of rejected impurities outside the crystalline volume as evidence in itself for nonlinear growth kinetics. As discussed by Keith and Padden (1964b), the onset of nonlinear growth is favored by reducing the molecular weight of the impurity or by increasing the crystallization temperature to reduce the driving force for crystallization and to enhance impurity diffusivities. Water, the impurity of interest for natural spherulites, satisfies these conditions: it is relatively mobile, depresses the rhyolite liquidus, and enhances the diffusivity of other melt components.

An additional argument can be made for diffusion-controlled growth from the results presented in figures 2.6 and 2.7. The model curves in figure 2.7 indicate that both spherulites experienced the same duration of post-growth diffusion of water, and hence, stopped growing at the same time or temperature. Intuitively, one would expect that the larger spherulite began growing earlier at higher temperatures - a possibility that is not explicitly accounted for in our model. Note, however, that we assume constant a , n , and

D_{OH} (constant with respect to temperature). Of these parameters, D_{OH} is the only one that is likely to change with temperature during spherulite growth. The observed differences in a and n between spherulites may thus represent changes in D_{OH} with temperature. In the diffusion-controlled growth model, a larger a translates into a higher average D_{OH} (i.e., temperature) for the larger spherulite ($a=1.02$) versus the smaller spherulite ($a=0.8$), consistent with the expectation stated above. In contrast, if we assume a linear growth law, comparable fits between the larger spherulite ($n=0.0026$) and smaller spherulite ($n=0.0052$) correspond to lower temperatures (i.e., slower average growth rate) for the larger spherulite, which is difficult to reconcile with the assumption that both spherulites stopped growing at the same temperature. Indeed, using a slightly different modeling approach, Castro et al. (2008) found that larger spherulites experienced higher average growth rates than smaller spherulites. In their paper, however, this result was attributed to size-dependent growth rates versus our suggestion here that this reflects different temperature histories (i.e., temperature-dependent growth rates).

Diffusion-controlled growth also has implications for the size distribution of spherulites. For instance, we should expect a greater abundance of larger spherulites because rapid initial growth allows smaller spherulites to catch up in size to those earlier-forming, larger spherulites. Qualitatively, this seems to be the case for our samples. However, no attempt was made to statistically analyze spherulite sizes because of the limited size of our hand sample and the challenge of sectioning spherulites through their center.

2.9.1 On what timescales do spherulites grow?

Using water rejection as a proxy for crystallization rates, it is possible to calculate timescales for spherulite growth. This requires knowledge of the diffusivity of water (D_{OH}) during spherulite formation, and one obvious shortcoming of the model is the assumption that D_{OH} is fixed in a rhyolite undergoing cooling. Nevertheless, we calculate isothermal spherulite growth rates to bracket the true timescales for spherulite formation. Using D_{OH} in rhyolite at conditions relevant to our samples (~ 0.1 wt.% water and 0.1 MPa; Zhang and Behrens (2000)), the time required to grow a spherulite of given radius comes from the scaling relationship

$$t \sim \frac{R^2}{D_{OH}} \quad (2.6)$$

where R is the final radius of the spherulite. Results are summarized in figure 2.8, which shows the time required for a spherulite to reach a given radius at various fixed temperatures. For simplicity, these calculations assume that D_{OH} is not dependent on water concentration. We justify this by noting that these values are within a factor of 2 to the values we calculate from our full advection-diffusion model for radii greater than about 1 mm.

According to the diffusion-controlled growth model, a spherulite of 2.6 millimeters requires ~ 300 days at 800°C , ~ 10 years at 600°C , or ~ 300 years at 400°C . These timescales are consistent with spherulites forming at temperatures above 600°C in parts of lava flows that cool on the order of years to decades in heat flow models that assume instantaneous emplacement of lava followed by static cooling (Manley, 1992; Manley and Fink, 1987). At temperatures below about 400°C , diffusion-controlled growth is extremely sluggish and we consider $T=400^\circ\text{C}$ an approximate lower bound for spherulite growth during cooling. This

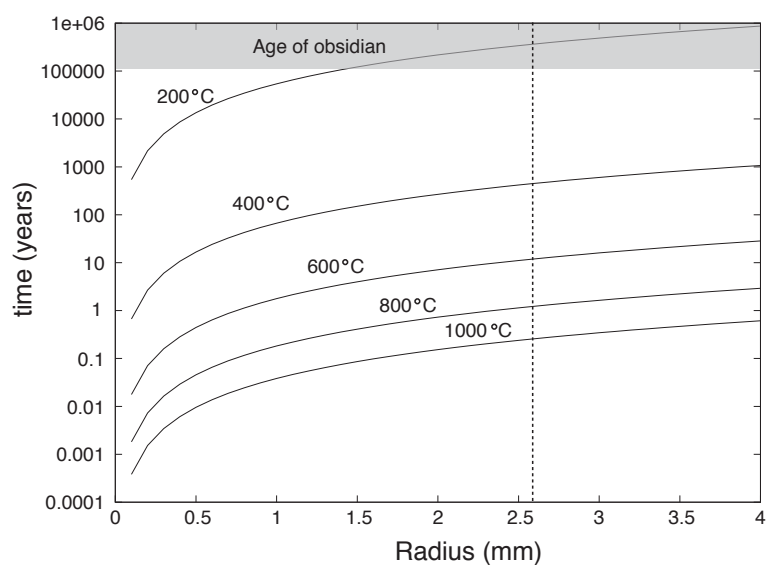


Figure 2.8: Time required to grow a spherulite of given radius at various fixed temperatures assuming a diffusion-controlled growth law and using a proportionality constant of $a=1.0$. The shaded region at the top of the graph encompasses the range of possible ages for the host obsidian (Lewis-Kenedi et al., 2005) and the dashed line indicates the size of the largest spherulite analyzed in this study. For spherulites to grow appreciably on cooling timescales, they must form at temperatures above about 400°C.

can explain the absence of macroscopic spherulites along quench margins where rapid cooling has minimized the duration of high temperature growth rates. Of course, better estimates for timescales of spherulite growth require additional constraints on the temperature of spherulite formation and the cooling history of their host.

2.9.2 At what degree of undercooling do spherulites begin to grow?

Emplacement temperatures for rhyolite vary considerably (790°C–925°C; Carmichael et al., 1974). At the time of emplacement, an anhydrous rhyolite lava may be significantly undercooled, as the liquidus in this system is $\sim 1000^\circ\text{C}$ (Ghiorso and Sack, 1995). Owing to nucleation lag times, which may be on the order of tens of years (Manley, 1992), the degree of undercooling at which nucleation actually occurs is difficult to constrain. Nevertheless, textural relationships can provide a first-order estimate. For example, crystal morphologies have been shown to correlate with the degree of undercooling in the $\text{NaAlSi}_3\text{O}_8\text{-KAlSi}_3\text{O}_8\text{-H}_2\text{O}$ system (Fenn, 1977). Feldspars grown in this system formed as (1) isolated tabular crystals at low undercoolings ($\Delta T < 40^\circ\text{C}$), (2) coarse, open spherulites at moderate undercoolings ($\Delta T \sim 75\text{-}145^\circ\text{C}$), and (3) fine, closed spherulites at higher undercoolings ($\Delta T \sim 245\text{-}395^\circ\text{C}$) (Fenn, 1977). This latter group of textures corresponds to the spherulites pictured in Figure 2.1. From this information, a minimum ΔT on the order of 150°C (corresponding to a maximum $T = 850^\circ\text{C}$) seems reasonable for the onset of spherulite growth, providing a minimum growth time of ~ 100 days. Larger ΔT associated with longer nucleation lag times are certainly possible and are probably common given that spherulites are generally smaller than the cooling timescales of decades would otherwise allow.

2.9.3 Do spherulites grow below the glass transition?

The glass transition signals an abrupt change in the physical properties of a melt, namely a change from liquid-like to solid-like behavior. The temperature at which this takes place depends on composition and cooling rate. For anhydrous rhyolite, the glass transition temperature (T_g) lies somewhere between 620°C and 750°C (based on values in Swanson et al. (1989); Manley (1992); Westrich et al. (1988)), and it has been suggested that T_g may provide a minimum temperature for spherulite growth (Ryan and Sammis, 1981; Manley, 1992; Davis and McPhie, 1996). Indeed, certain field observations such as deformation of spherulites (Martin and McKinney, 1988), boudinage of flow bands by spherulites (Manley, 1992; Stevenson et al., 1994), and inflation of lithophysal cavities (Swanson et al., 1989) suggest that spherulite growth takes place in melts above T_g . However, these features are not always observed. The spherulites used in this study, for instance, are undeformed and cross cut flow bands, raising the possibility that they grew, at least in part, below the glass transition.

Since we assume that spherulite growth is governed by diffusion of components across spherulite boundaries, the question of whether spherulites grow below T_g is really a question of how elemental diffusivities are affected by the glass transition. Based on the study by Zhang and Behrens (2000), the diffusivity of water appears to vary smoothly across the glass transition. Figure 2.9 shows diffusivities for other various chemical species in

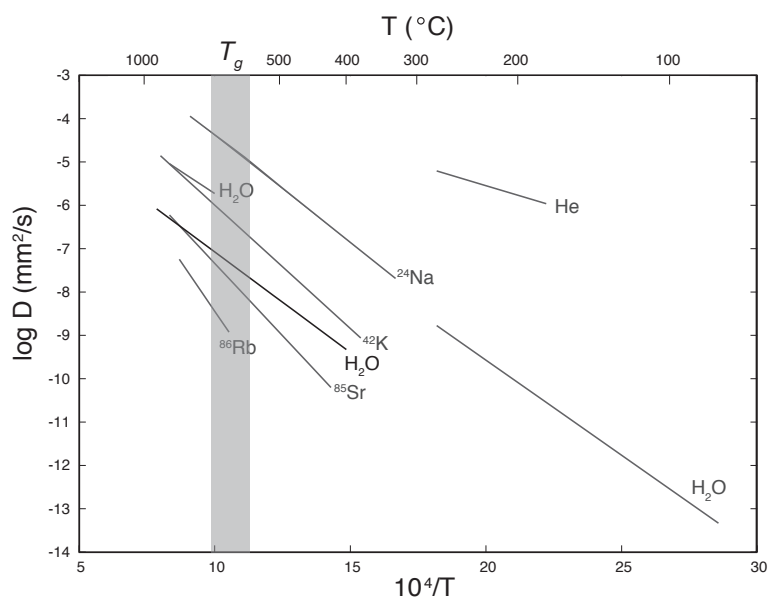


Figure 2.9: Temperature-dependence of diffusivities for various chemical species in obsidian. Dark line for H_2O is from equation 12 in Zhang and Behrens (2000) and grey lines for H_2O are from obsidian hydration experiments (see Freer, 1981). All other lines are from the compilation by Freer (1981). The main point is that major- and trace-element diffusivities appear to be insensitive to the glass transition in melts of rhyolitic composition (region shown in grey).

rhyolitic obsidian as a function of temperature. Across the range of possible glass transition temperatures, there is no evidence for significant changes in the diffusivity mechanisms for any of the components shown. This is consistent with the notion that rhyolite liquids are structurally similar to rhyolite glasses, as evidenced by only minor changes ($\sim 5\%$) in heat capacity across the glass transition (Neuvill et al., 1993). Hence, there is no reason to believe that the glass transition represents an abrupt barrier to spherulite growth. However, it is apparent from the diffusion-controlled growth model that growth rates become prohibitively slow below about 400°C .

2.9.4 Why doesn't spherulite growth lead to runaway heating?

An issue we have not yet addressed is the release and transport of latent heat as spherulitic crystallization progresses (cf. Lofgren, 1971a). Diffusion of latent heat into the surrounding matrix could insulate growing spherulites, prolonging their exposure to elevated temperatures. Latent heat could also, in principle, lead to increased growth rates and the release of more latent heat in a positive feedback loop (Carmichael, pers. comm.). Obviously, this runaway heating does not take place since almost all spherulite-bearing rocks are vitrophyric. In order to explain this, we again turn to diffusion-controlled growth. We have already shown that spherulite growth is limited by the mobility of chemical species, and that spherulite growth rates proceed on the same timescale as water diffusion rates. A maximum D_{OH} of about 10^{-6} mm^2/s in rhyolite corresponds to $T=850^\circ\text{C}$. This is seven orders of magnitude lower than thermal diffusivity in obsidian, which is on the order of 10^{-1} mm^2/s over the temperature range $0\text{-}800^\circ\text{C}$ (Riehle et al., 1995). Hence, latent heat is carried away long before it can influence spherulite growth rates.

2.9.5 Why are spherulites spherical?

Natural spherulites are host to multiple crystalline phases with very different individual morphologies (figure 2.1). On the whole, however, spherulites are almost perfectly spherical. The simplest explanation is that their host glass or melt is homogeneous, thus offering no preferred direction in which to grow. As we noted earlier, however, some spherulites cross cut bands of textural and compositional heterogeneities (Gonnermann and Manga, 2003). An alternative explanation can be found by invoking sufficiently rapid diffusion of water.

As spherulites grow outwards and water is rejected into the surrounding matrix, there is a local reduction in the relative abundance of crystal-forming components. Since water content decreases with distance (over diffusion lengthscales) from the spherulite rim, any crystalline protrusion will grow into a melt at a higher supersaturation (i.e., higher undercooling) and respond by growing faster. This runaway effect can lead to dendritic crystals or cellular morphologies (Kirkpatrick, 1975). However, there is an increase in surface energy associated with breaking the spherical symmetry of a growing spherulite. The stability of a spherical interface with finite surface tension is determined by a competition between growth rate and diffusion rate. At low growth rates, surface tension and diffusion act to maintain a minimum surface energy configuration (i.e., spherical). With increasing growth rate, however, there comes a critical point described by the Mullins-Sekerka instabil-

ity at which diffusion and surface tension can no longer prohibit dendritic growth (Mullins and Sekerka, 1963; Langer, 1980). As one might expect, the transition from spherical to dendritic morphology depends on the diffusion length over which the crystallizing components are depleted. Qualitatively, for large diffusion lengths the increase in supersaturation surrounding a protrusion is minor compared to the rest of the spherulite. This notwithstanding, we attribute the sphericity of spherulites in our samples to the high mobility of water relative to the reaction rate under the conditions at which these crystals grew.

2.10 Conclusions

Water concentration profiles adjacent to spherulite rims provide information about the growth history of spherulites in rhyolitic vitrophyres. We have shown that these profiles can be modeled assuming a combination of diffusion-controlled spherulite growth kinetics and post-growth diffusion of water. Qualitatively, this model can resolve temperature differences at which different spherulites grew and it accounts for why spherulites are spherical. We find that the glass transition is not a barrier to spherulite growth because chemical diffusivities are not sensitive to this transition. Furthermore, because thermal diffusivities are much greater than chemical diffusivities, spherulite crystallization does not lead to runaway heating and complete crystallization or devitrification of rhyolitic vitrophyres.

Our model also provides timescales for spherulite growth. Swanson (1977) was the first to show that crystals can grow to large sizes (mm-scale) on surprisingly short timescales (on the order of days) in systems with more than one phase. We have inferred that this holds true in the natural setting where spherulites can grow to large sizes on the order of days at eruptive temperatures. However, spherulite growth rates decrease exponentially with temperature and become prohibitively slow at temperatures below about 400°C.

Lastly, we emphasize that the results presented here are based on spherulites from a single locality. A similar approach applied to spherulites from elsewhere will be useful in the future. In particular, we would like to compare timescales of during- and post-growth diffusion of water between spherulites that experienced different cooling histories. Information such as this may lead to an explanation for how and when spherulite growth and water diffusion become decoupled.

Chapter 3

Isotope separation by diffusion in natural molten silicates

3.1 Introduction

This study was motivated by the idea that diffusive isotopic fractionations might provide information on the size and stoichiometry of diffusing species in silicate liquids. Natural silicate liquids can be viewed as concentrated solutions of roughly ten major elements distributed among various dissolved chemical species. The nature of these dissolved species is of broad interest for understanding thermodynamic and transport properties of silicate liquids (e.g., Navrotsky et al., 1989; Ghiorso et al., 1983; Hess, 1995; Ghiorso et al., 2002; Halter and Mysen, 2004), and yet, it is difficult to define the actual chemical constituents in a melt because of the disordered and dynamic nature of silicate liquid structures. Our focus in this work is on the relationship between liquid structure and isotopic diffusion. In particular, we are interested in whether the relative mobility of isotopes reflects the relative mobility of isotopically-distinct complexes, and if so, how does this fit into the emerging picture of silicate liquid structure and dynamics?

3.1.1 Speciation and silicate liquid structure

The main structural units in silicate materials are silica and alumina tetrahedra that are either isolated or are linked together by bridging oxygen atoms to form chains, rings, sheets, and three-dimensional networks of $(\text{Al,Si})\text{O}_x$ structural units (Calas et al., 2006; Henderson et al., 2006). In the liquid state, these aluminosilicate structures do not move as long-lived, well-defined molecular units, but are constantly reorganizing through rapid breaking and re-forming of bridging oxygen bonds (Stebbins, 1995). The definition of chemical “species” in silicate liquids thus becomes ambiguous, since it depends on the interconnectivity as well as the longevity of aluminosilicate networks, and the strength with which the other cations (e.g., Fe, Mg, Ca, Na, K) are bonded to them. This ambiguity makes it difficult to parameterize the configurational entropy of silicate liquids and represents a major obstacle for producing an accurate general model for their thermodynamic properties (e.g. Hess, 1995; Ghiorso et al., 2002). There is a long history of research on

the molecular-scale structures of silicate liquids and glasses (see Mysen and Richet, 2005, for a recent synthesis). A variety of spectroscopic and diffraction techniques are used to probe structures in glasses and liquids, and each is sensitive to the structure at different length and time scales. X-ray scattering and absorption probe structures as they appear on timescales of about 10^{-16} s and the resulting spectra for a given element are sensitive to the local bonding environment up to length scales of about 10\AA (e.g., bond distance, bond angle, coordination number, and connectivity to the first few neighboring atoms; Brown et al., 1995). Vibrational spectra (e.g., Infrared and Raman) probe interatomic bonding environments averaged over timescales of about 10^{-12} s and have been used to identify chemical species with lifetimes greater than this value (McMillan and Wolf, 1995). Nuclear-magnetic resonance (NMR) methods probe local chemical environments up to about 10\AA over timescales ranging from 10^{-4} to about 10^{-8} s (Stebbins, 1995). The timescale relevant for diffusion is the reciprocal of the typical jump frequency (Dingwell, 1990), which is on the order of 10^{-8} s, and therefore closest to the timescale for NMR. Despite the extensive and detailed information available on silicate liquid structure, there is still considerable uncertainty surrounding the size and lifetimes of polymeric structures in silicate liquids (Lee and Stebbins, 2006). And as Henderson et al. (2006) recently noted, this “intermediate range structural order, involving organization at nanometer and longer length scales, is still a major challenge but must be of critical importance to kinetics of crystal nucleation and diffusive transport.”

3.1.2 Diffusion in silicate liquids

Diffusion data is usually presented and modeled in terms of simple oxide components, despite the fact that the oxides cannot be the actual diffusing entities. There is a substantial literature on diffusion in silicate liquids, but in particular Dingwell and Webb (1989), Dingwell (1990, 2006), Kress and Ghiorso (1993), and Chakraborty et al. (1995) address the relationships between melt structure or speciation and diffusion. More often, chemical changes due to diffusion are regarded as the result of transport of either oxide or elemental species.

In many cases it is difficult to use diffusion data to infer the existence or composition of multi-atom complexes in silicate liquids. Our approach concerns the effect of diffusion on isotopic fractionation of the major elements of silicate liquids. The only significant difference between isotopes (e.g. ^{44}Ca and ^{40}Ca) is mass. Hence if it is observed that there is a difference in the diffusion coefficients of two isotopes of an element, resulting in isotopic fractionation, it is reasonable to infer that this is due to a difference in the mass of the diffusing *species*. Previous studies have shown that chemical diffusion of Ca, Mg, K, Li, and other minor elements in silicate liquids produces isotopic fractionation because lighter isotopes of an element tend to diffuse slightly faster than heavier isotopes (Baker, 1989; Leshner, 1994; Richter et al., 2003). However, there has not been a systematic investigation of the dependence of isotopic fractionation on liquid composition. This chapter is devoted to the idea that such an approach might open a new window for understanding diffusion mechanisms in the context of liquid structure and dynamics.

3.2 Mass dependence on diffusivity

There is no general theory that predicts how diffusivity should vary with mass in liquids. In a dilute gas with mean molecular mass M , the kinetic theory model predicts a power law relationship between diffusivity and the reduced mass μ of isotopically distinct species and that the power law exponent is equal to 1/2 (Mills and Harris, 1976):

$$\frac{D_2}{D_1} = \left(\frac{\mu_1}{\mu_2} \right)^{1/2}, \quad (3.1)$$

where

$$\mu_i = \frac{\mu_i M}{\mu_i + M} \quad (3.2)$$

In the limit that $M \gg \mu_i$, this reduces to commonly used square-root of mass law:

$$\frac{D_2}{D_1} = \left(\frac{m_1}{m_2} \right)^{1/2}. \quad (3.3)$$

In the solid-state diffusion literature, this equation with a power law exponent of 1/2 is used as a reference and the mass dependence on diffusivity is discussed in terms of the efficiency of isotope separation E , which is defined as (Schoen, 1958)

$$E = \frac{D_2/D_1 - 1}{(m_1/m_2)^{1/2} - 1}, \quad (3.4)$$

where $E=1$ when equation 3.3 is true. The magnitude of deviations from the $m^{-1/2}$ dependence can be used to infer diffusion mechanisms using crystal lattice models (Rothman and Peterson, 1965). In some cases these mechanisms are discussed in terms of the number and masses of other atoms whose motions are correlated with the movement of the atom of interest. This is essentially a description of diffusive coupling and its effect on the isotopes – a concept that should also apply to isotope diffusion in liquids. In liquid systems, the approach taken in the geochemical sciences is to assume a power law relationship akin to equation 3.3 but generalized as

$$\frac{D_2}{D_1} = \left(\frac{m_1}{m_2} \right)^\beta. \quad (3.5)$$

where it is observed that the power law exponent β is always some value less than 1/2 in aqueous solutions (e.g., Richter et al., 2006; Bourg and Sposito, 2007, 2008), and silicate liquids (Richter et al., 1999, 2003, 2008). This is similar to equation 3.4 and one can easily convert between the two through the relationship that $E=2\beta$.

Calculations of E and/or β implicitly assume that a power law relationship exists between diffusivity and mass in condensed systems and that the mass of the diffusing species m_1 is that of the isotope itself. In pure metals, this is perhaps unambiguous, but in silicate liquids it is not. The general interpretation for values of $E < 1$ is that the movement of the atoms of interest (of masses m_1 and m_2) is correlated with the movements of other atoms,

and the value of E can be estimated if the number and masses of the other atoms involved are known. Rothman and Peterson (1965) give the following more general expression for E :

$$E' = \frac{2\ln(D_2/D_1)}{\ln(nm + m_1)(nm + m_2)}, \quad (3.6)$$

where m and n are the average mass and the number, respectively, of the other species whose motions are correlated with those of the tracer atoms during diffusion. This general formula can allow one to speculate about whether diffusion involves larger complexes in the liquid phase, and how large those complexes might be. For example, if the motion of Ca were correlated with that of an AlO_4 tetrahedral unit (mass 91), then the ratio of the diffusivities of ^{44}Ca and ^{40}Ca would appear to correspond to masses of 135 and 131 (for $E=1$) rather than to masses 44 and 40.

3.2.1 Diffusive isotopic fractionation

Richter et al. (2003) (hereafter RDDW) and Richter et al. (2008) observed isotopic fractionation of Ca, Mg, and Li as a result of interdiffusion between a mid-ocean ridge (tholeiitic) basalt and rhyolite. Using a chemical diffusion model, RDDW determined the ratio of the diffusivities of ^{44}Ca and ^{40}Ca to be $D_{44}/D_{40}=0.993$, the diffusivities of ^7Li and ^6Li to be $D_7/D_6=0.967$ and the diffusivities of ^{26}Mg and ^{24}Mg to be $D_{26}/D_{24}=0.996$. The uncertainties on these numbers are not precisely defined, but they are roughly ± 0.0015 .

Isotopic system	D_2/D_1	β	Reference	$(nm+m_1)^*$
$^{44}\text{Ca}/^{40}\text{Ca}$	0.993	0.075	Richter et al. (2003)	278
$^{26}\text{Mg}/^{24}\text{Mg}$	0.996	0.05	Richter et al. (2008)	249
$^7\text{Li}/^6\text{Li}$	0.967	0.215	Richter et al. (2003)	15

Table 3.1: Differences in isotope diffusivities for Ca, Mg, and Li obtained in basalt-rhyolite interdiffusion experiments.

Table 3.1 summarizes the results of the Richter et al. (2003, 2008) experiments on silicate liquids, and includes the values of β , as well as numbers derived from equation 3.6 for the value of $(nm+m_1)^*$, which assumes $E'=1$ and is therefore a maximum for this parameter. For Ca and Mg, the derived values for $(nm+m_1)^*$ are substantially larger than the atomic mass of the light isotope and suggestive that the movement of these species is correlated with the movement of at least 5-6 other atoms in the liquids. In contrast, the value of $(nm+m_1)^*$ for Li is not much larger than the atomic mass of Li, and in fact requires $n < 1$ if m is to represent the mass of a major element. This suggests that for Li, the diffusing species is probably the Li atom, and its movements are not strongly correlated with the movement of other species in the liquid.

3.3 Approach

If a complex like CaAl_2O_4 were important for diffusion, it would imply that diffusion of Ca and Al be strongly coupled. In addition, one might expect that if there are

multiple Ca-bearing complexes, each complex should have a different effect on the mass discrimination of Ca during diffusion.

The experiments of Richter et al. (2003, 2008) were done using the same compositions of basalt and rhyolite in all cases. The basalt is a tholeiitic mid-ocean ridge composition and the rhyolite is a calc-alkaline composition (Table 3.2). As we noted earlier, these experiments provide interesting insights on the possible structure of silicate liquids, and more information may be accessible by varying the compositions of the liquids. For example, more Mg-rich and Al-poor liquids would have fewer Al-Si-O complexes and therefore fewer bridging oxygen atoms between (Al,Si)O₄ tetrahedra.

To test how mass discrimination by diffusion is related to silicate liquid structures, we performed experiments similar to those of Richter et al. (2003, 2008) using different starting compositions for the mafic endmember (Table 3.2). In our first two experiments, we chose a Hawaiian basalt composition (H36B; Hofmann and Magaritz, 1977) rather than the tholeiitic basalt used by RDDW. In subsequent experiments, we replaced basalt with ugandite (U105), chosen for its lower silica content, lower Al, higher Mg and alkalis, and because it is presumably less polymerized than tholeiitic basalt. As described below, both series of experiments produced Ca isotopic effects that are significantly different from those observed by RDDW.

3.4 Results

A total of four diffusion couple experiments were measured for chemical diffusion profiles by electron microprobe and sectioned for Ca isotope analysis. Here, we compare and contrast major-element profiles and Ca isotope measurements between the basalt-rhyolite experiments in RDDW, two basalt-rhyolite experiments from this study, and two ugandite-rhyolite experiments from this study. The bulk composition and Ca isotope composition for each starting material is shown in Table 3.2.

3.4.1 Major-element diffusion profiles

Figures 3.1 and 3.2 are major-element diffusion profiles for the basalt-rhyolite and ugandite-rhyolite experiments, respectively. All of the profiles exhibit asymmetry that comes from the dependence of diffusivities on composition (primarily silica content). In figure 3.1 there is so-called “uphill diffusion (i.e., diffusion of a species against its own concentration gradient) exhibited by Na₂O and Al₂O₃, the latter having only a minor concentration contrast between starting materials. The rest of the oxides show generally simple monotonic diffusion profiles. The concentration profiles for the Kilauea basalt-rhyolite experiment are similar to those measured by RDDW in their basalt-rhyolite experiments.

Several of the profiles from the ugandite-rhyolite experiment (Figure 3.2) differ markedly from those in the basalt experiment. For instance, there is strong uphill diffusion and/or sharp gradients exhibited by each of the oxides associated with feldspar formula units (K₂O, Na₂O, SiO₂ and Al₂O₃). An inset in the CaO profile shows that CaO also exhibits uphill diffusion. Note that unlike the basalt experiments there is a relatively large Al₂O₃ concentration gradient that is opposite the gradient of CaO.

Starting compositions				
Weight per cent	SUNY MORB* tholeiitic basalt	H36B** tholeiitic basalt	U105 (XRF) ugandite	LCO (WDS) rhyolite
SiO ₂	49.75	49.68	40.56	75.94
TiO ₂	1.63	2.59	5.02	0.11
Al ₂ O ₃	16.07	12.7	8.04	12.89
Fe ₂ O ₃	-	-	-	-
FeO	9.49	11.05	12.21	0.81
MnO	-	0.17	0.20	0.04
MgO	8.56	9.46	11.81	0.11
CaO	10.80	10.79	12.65	0.75
Na ₂ O	2.89	2.31	2.47	2.96
K ₂ O	0.18	0.48	3.71	5.48
P ₂ O ₅	-	-	0.44	-
LOI	-	-	2.13	-
Total	99.37	99.23	99.81	99.09
<hr/>				
Mole per cent				
KAIO ₂	0.26	0.67	4.97	7.71
NaAlO ₂	6.29	4.89	4.98	6.33
CaAl ₂ O ₄	7.36	5.39	0	0.87
MgAl ₂ O ₄	0	0	0	0.18
SiO ₂	55.85	54.22	42.59	83.76
TiO ₂	1.38	2.13	3.97	0.09
FeO	8.91	10.09	10.72	0.75
MgO	14.33	15.39	18.49	0
CaO	5.63	7.23	14.23	0
Na ₂ O	0	0	0.05	0
K ₂ O	0	0	0	0
<hr/>				
$\delta^{44}\text{Ca}^\ddagger$	-0.22	-0.33	-0.41	-0.28

* Richter et al. (2003)

** Hofmann and Magaritz (1977)

‡ Uncertainties in $\delta^{44}\text{Ca}$ are within $\pm 0.15\%$.

Table 3.2: Bulk composition and Ca isotope composition of starting materials used in diffusion couple experiments. Major element abundances are shown both in terms of oxide components as well as in terms of species used in the Bottinga and Weill (1972) viscosity model.

Starting compositions			Temperature	Pressure	Duration	Ramp rate	Capsule length (post-run)
Mafic	Felsic		(°C)	(Gpa)	(hrs)	(°C/min)	(mm)
RB-2	SUNY MORB	Obsidian	1450	1.3	15.7	75	~8
RB-3	SUNY MORB	Obsidian	1450	1.2	12.0	75	~8
DF-5	Kilauea basalt	Obsidian	1450	1.0	12.0	150	6.98
DF-9	Kilauea basalt	Obsidian	1450	1.0	12.0	150	7.25
DF-8	Ugandite	Obsidian	1450	1.0	24.0	150	8.4
DF-11	Ugandite	Obsidian	1450	1.0	12.0	150	7.12

Table 3.3: Initial and experimental conditions for each of the diffusion-couple experiments. RB2 and RB3 are from RDDW. All other experiments were performed in this study.

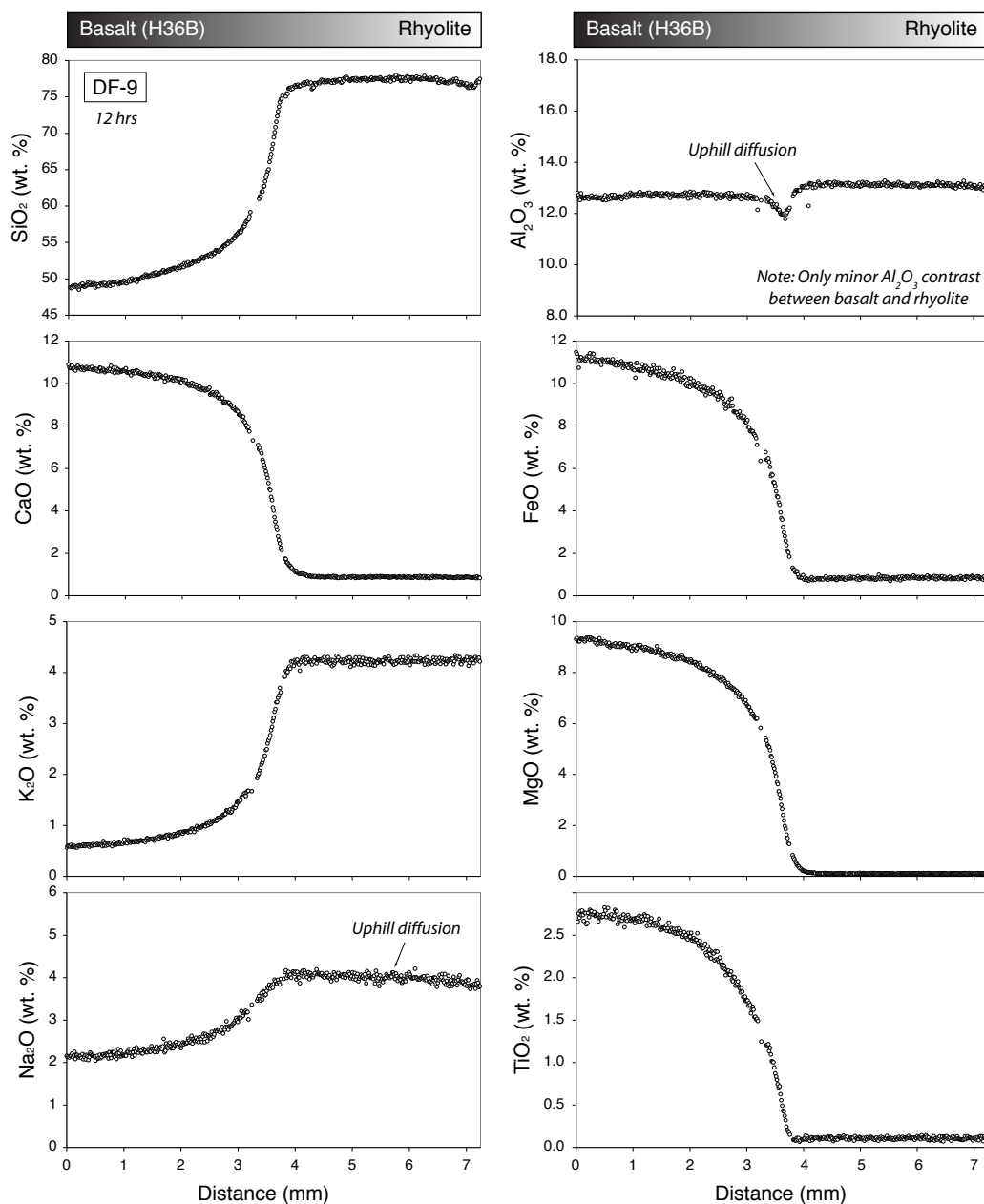


Figure 3.1: Major-element diffusion profiles from a basalt-rhyolite diffusion couple experiment. The asymmetry in each of profiles reflects a decrease in diffusivity with increasing silica content. Overall, the profiles are relatively simple, monotonic diffusion profiles except Na₂O and Al₂O₃, which exhibit uphill diffusion. Note the Al₂O₃ contrast between starting liquids is small.

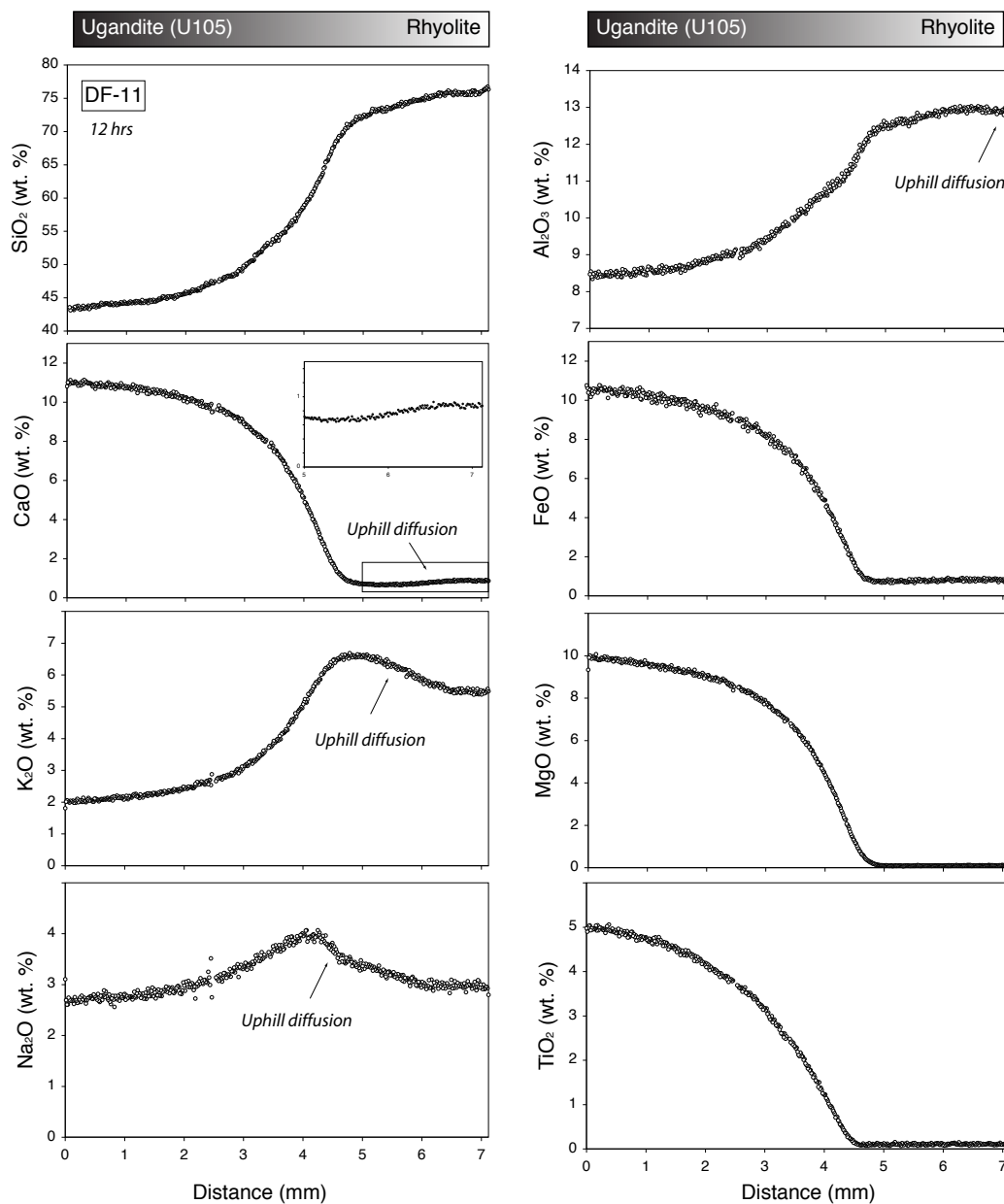


Figure 3.2: Major-element diffusion profiles from a ugandite-rhyolite diffusion couple experiment. Overall, the profiles are more complicated than those in figure 3.1, with uphill diffusion of Na_2O , K_2O , and CaO (see inset) due to, presumably, diffusive coupling to Al_2O_3 . Note that unlike the basalt-rhyolite experiments, there is a large Al_2O_3 gradient going from right to left.

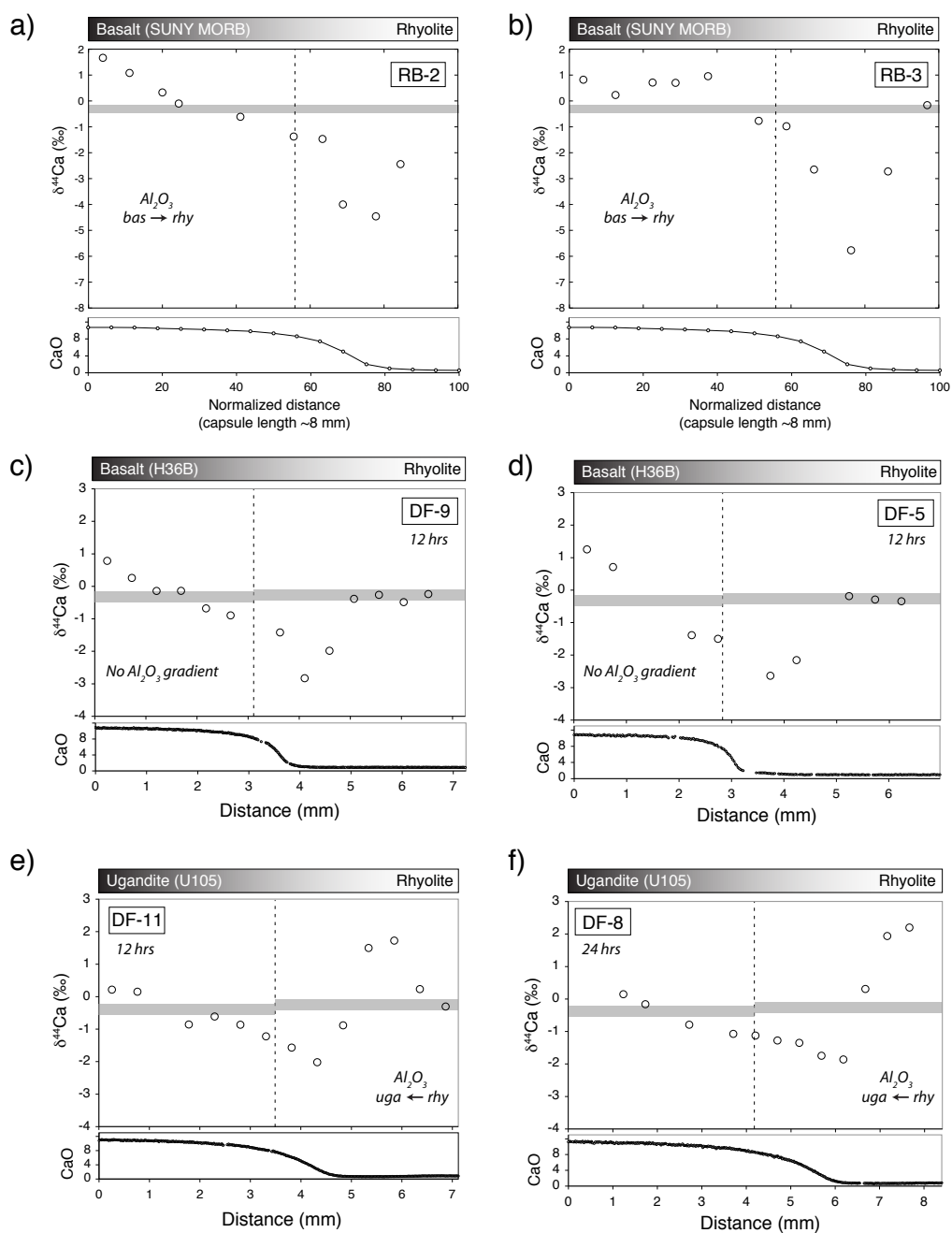


Figure 3.3: Ca isotope profiles from three sets of experiments. The initial interface between starting liquids is given by the vertical dashed line. The grey horizontal bar shows the initial isotopic composition. Corresponding CaO diffusion profiles are shown below each plot. The high values of $\delta^{44}\text{Ca}$ in the rhyolite in (e) and (f) is interpreted as evidence for diffusive coupling of Ca to Al (see text).

3.4.2 Calcium isotope profiles

Post-run Ca isotope profiles were measured across each diffusion couple and large fractionations from the initial Ca isotope composition were observed for each experiment. All Ca isotope measurements are reported in Table 3.4. Figures 3.3a and 3.3b show the Ca isotope profile and corresponding Ca diffusion profile from RDDW. In their two experiments (RB2 and RB3) the minimum in $\delta^{44}\text{Ca}$ is about 5 to 6‰ lower than the starting compositions, and the isotopic effects extend nearly to the end of the capsule on the rhyolite side. For comparison, figures 3.3c and 3.3d show results from this study for our Kilauea basalt-rhyolite diffusion couples run under the same conditions but with a different, yet still tholeiitic, basalt composition. Overall, the profile has a similar shape, but the minimum $\delta^{44}\text{Ca}$ is less extreme at -3‰. In addition, our experiments were loaded with a thicker section of rhyolite and it can be seen that the Ca isotopic composition is uniform throughout the rhyolite end of the charge where the rhyolite Ca concentration has been unaffected by diffusion of Ca from the basalt.

Figures 3.3e and 3.3f show results from ugandite-rhyolite experiments run for 12-hours and 24-hours, respectively. In these experiments, the minimum in $\delta^{44}\text{Ca}$ is only about -2‰. There is also a large increase in $\delta^{44}\text{Ca}$ that developed on the rhyolite side of the capsule beyond the diffusion front of Ca from the ugandite. In the 24-hour run (figure 3.3f), the increased $\delta^{44}\text{Ca}$ extends to the end of the capsule. In all of the experiments, there are linear gradients in $\delta^{44}\text{Ca}$ on the mafic side of the capsule with a total range of about 2 to 4 units. A similar linear gradient is observed in one of the RDDW runs (RB-2), and in a run where Mg isotopes were measured (Richter et al., 2008).

3.5 Discussion

3.5.1 Interpretation of basalt-rhyolite experiments

In all of the experiments, isotopes of calcium become fractionated by chemical diffusion as the lighter isotope (^{40}Ca) diffuses slightly faster than the heavy isotope (^{44}Ca). In the basalt-rhyolite experiments, this explains the main features of the measured profiles: (1) Ca has diffused from the basalt end, leaving the basalt isotopically heavier (2) the isotopic composition at the rhyolite end is unchanged because Ca has not diffused into or out of that region, and (3) the isotopic effects are enhanced on the rhyolite side because the rhyolite initially has very little Ca. In the simplest model to describe the diffusion effects (used by RDDW), the minimum in $\delta^{44}\text{Ca}$ should depend only on the initial Ca concentration contrast and the relative diffusivities of the isotopes (i.e., β in equation 3.5).

In the first study of this type, (Richter et al., 1999) measured diffusive isotope fractionations of Ca between synthetic basalt and synthetic rhyolite and found a value for β of between 0.05 and 0.08. Because those values are similar to the values deduced from the natural basalt-rhyolite experiments in RDDW, it was suggested that $\beta=0.075 (\pm 0.025)$ may be a general feature of silicate liquids, independent of liquid composition. However, in our basalt-rhyolite experiments (figures 3.3c and 3.3d), the minimum $\delta^{44}\text{Ca}$ of -3‰ translates to $\beta=0.035\pm 0.005$, which is significantly different. This result suggests that the relative Ca isotope diffusivities are sensitive to slight changes in liquid composition.

Basalt-Rhyolite experiments			Ugandite-Rhyolite experiments		
Sample (wafer no.)	Distance (mm)	$\delta^{44}\text{Ca}$ (‰)	Sample (wafer no.)	Distance (mm)	$\delta^{44}\text{Ca}$ (‰)
DF5-1	6.727	-	DF8-1	8.153	-
DF5-2	6.229	-0.34	DF8-2	7.659	2.20
DF5-3	5.730	-0.29	DF8-3	7.165	1.94
DF5-4	5.232	-0.19	DF8-4	6.671	0.31
DF5-5	4.734	-	DF8-5	6.176	-1.86
DF5-6	4.235	-2.16	DF8-6	5.682	-1.74
DF5-7	3.737	-2.64	DF8-7	5.188	-1.35
DF5-8	3.239	-2.47	DF8-8	4.694	-1.27
DF5-9	2.741	-1.50	DF8-9	4.200	-1.12
DF5-10	2.242	-1.39	DF8-10	3.706	-1.07
DF5-11	1.744	-	DF8-11	3.212	-
DF5-12	1.246	-	DF8-12	2.718	-0.79
DF5-13	0.747	0.71	DF8-13	2.224	-
DF5-14	0.249	1.25	DF8-14	1.729	-0.16
DF9-1	7.005	-	DF8-15	1.235	0.15
DF9-2	6.525	-0.24	DF8-16	0.741	-
DF9-3	6.042	-0.49	DF8-17	0.247	-
DF9-4	5.558	-0.26	DF11-1	6.865	-0.29
DF9-5	5.075	-0.39	DF11-2	6.357	0.25
DF9-6	4.592	-1.99	DF11-3	5.848	1.74
DF9-7	4.108	-2.83	DF11-4	5.340	1.51
DF9-8	3.625	-1.42	DF11-5	4.831	-0.87
DF9-9	3.138	-	DF11-6	4.323	-2.00
DF9-10	2.658	-0.90	DF11-7	3.814	-1.56
DF9-11	2.175	-0.68	DF11-8	3.305	-1.20
DF9-12	1.692	-0.14	DF11-9	2.797	-0.85
DF9-13	1.208	-0.14	DF11-10	2.288	-0.59
DF9-14	0.725	0.26	DF11-11	1.780	-0.85
DF9-15	0.242	0.78	DF11-12	1.271	-
			DF11-13	0.763	0.17
			DF11-14	0.254	0.23

Table 3.4: Ca isotope measurements measured on wafers from four diffusion couple experiments. Also shown are the distances along the Ca diffusion profile associated with the center point of each wafer. Uncertainties in $\delta^{44}\text{Ca}$ are within ± 0.15 ‰.

One notable difference between the SUNY MORB and H36B starting materials is in the Al content. In RB2 and RB3, the basalt has a higher concentration of Al_2O_3 than the rhyolite, so the Al concentration gradient between the basalt and the rhyolite (table 3.2) is in the same direction as the CaO concentration gradient. In DF5 and DF9, the Al_2O_3 concentration gradient between the basalt and rhyolite is negligible (figure 3.1). This difference is noteworthy since previous studies (e.g., Kubicki et al., 1990; Chakraborty et al., 1995; Liang et al., 1996, and many others) have shown that diffusion of alkali and alkaline-earth cations can be strongly influenced by the magnitude and sign of Al gradients (hereafter referred to as “diffusive coupling”).

3.5.2 Interpretation of ugandite-rhyolite experiments

The Ca isotope profiles in the ugandite-rhyolite experiments (Figures 3.3e and 3.3f) are quite different from those in the basalt-rhyolite experiments. Especially notable is that the ugandite is Al-poor, hence the Al_2O_3 gradient in the ugandite-rhyolite experiments is such that Al is expected to be diffusing from the rhyolite into the ugandite. In these experiments, then, the Al gradient is opposite the Ca gradient, so if Ca and Al are coupled in the diffusion process this might be expected to be evident in the isotopic profiles.

The diffusion couple produced Ca concentration and isotope profiles on the mafic side of the capsule that are roughly similar to those produced in the Kilauea basalt-rhyolite couples. This requires that Ca is diffusing from the ugandite to the rhyolite, and that the ^{40}Ca species is diffusing more rapidly than the ^{44}Ca species. However, on the rhyolite side of the capsule there are two additional features. A small Ca concentration gradient developed within the rhyolite, with the concentration decreasing toward the ugandite. And in the region where this concentration gradient exists, there is a large increase in $\delta^{44}\text{Ca}$, suggesting that this region has been depleted of ^{40}Ca by preferential diffusion of light Ca toward the ugandite.

The immediate question is why Ca diffuses from the rhyolite toward the ugandite even though the ugandite has a higher Ca concentration. There are at least two possibilities. Since Ca will diffuse in response to chemical potential gradients, it is possible that Ca has a particularly low chemical potential in the new liquid composition generated within the rhyolite as it diffusively mixes with the ugandite. This might cause Ca to diffuse out of the pure rhyolite into the hybrid composition, depleting the neighboring part of the pure rhyolite in ^{40}Ca relative to ^{44}Ca . An alternative (or additional) explanation is that Al, which is diffusing from the rhyolite toward the ugandite, is combined with Ca in a Ca-Al complex, and that this component or species is diffusing out of the rhyolite toward the ugandite, leaving behind a residue that is enriched in ^{44}Ca . In the latter scenario, it would be required that the ugandite have a lower concentration of the Ca-Al complex than does the rhyolite, and that there is enhanced isotopic discrimination associated with diffusion of the Ca-Al complex. Although we may not be able to distinguish between the two possibilities, the results presented here clearly indicate that diffusive isotopic fractionations of Ca depend on the associations between different elements in the liquid.

3.5.3 Diffusive isotopic fractionation and speciation

There is no general agreement about what long-lived multi-atom species exist in silicate liquids. Empirical viscosity models (e.g., Bottinga and Weill, 1972; Hui and Zhang, 2007) incorporate alkali and alkaline earth aluminate components in addition to the simple oxides in order to account for the dual role of Al as a network-forming and network-modifying cation. Since viscosity and structural relaxation are functionally related to the diffusion of individual atoms in the liquid matrix (Dingwell, 2006), we have chosen to evaluate the possible role(s) that aluminate complexes might play in the diffusion process by recasting the diffusion profiles in terms of the species employed in the viscosity model of Bottinga and Weill (1972), which incorporates two Ca-bearing species, one of which is associated with Al.

Figure 3.4 compares the profiles of the two Ca-bearing species (CaO and CaAl_2O_4) to the isotope data presented in figure 3.3. In the basalt runs (figures 3.4a and 3.4b), the profiles for both Ca species appear to be simple monotonic diffusion profiles. The CaAl_2O_4 profile appears to extend further into the rhyolite and suggests that Ca may be more mobile when associated with Al. Figures 3.4c and 3.4d show CaO and CaAl_2O_4 for the ugandite experiments. In these experiments the CaO profile is again monotonic, but exhibits an irregularity in the tail of the diffusion profile that extends to approximately the point where the highest $\delta^{44}\text{Ca}$ value lies. The ugandite initially has zero CaAl_2O_4 due to its low Al_2O_3 concentration (Table 3.2), whereas the rhyolite has about 1 mol %. At the end of the run, the CaAl_2O_4 profile has become quite complicated. The ugandite near the end of the capsule has acquired CaAl_2O_4 , and in the mixing region between the liquids, the CaAl_2O_4 content is zero. The calculated zero value for CaAl_2O_4 arises because the liquids in this region have insufficient Al to make CaAl_2O_4 after the available Al has first been assigned to KAlO_4 and NaAlO_4 . This probably occurs because this region has acquired additional Na_2O and K_2O due to uphill diffusion (figure 3.2). It could reasonably be inferred that in this region, the chemical potential of the CaAl_2O_4 component is very low. The increased values of CaAl_2O_4 in the ugandite indicate that Al has been added in excess of any additions of Na and K. This is consistent with the Al_2O_3 profile (figure 3.2), which shows that the tail of the profile has penetrated all the way through the ugandite to the end of the capsule.

The enrichment of $\delta^{44}\text{Ca}$ in the rhyolite, which is the signature of residual Ca left behind after diffusive loss, suggests that Ca diffused out of this region. Since there is an Al gradient, decreasing toward the ugandite, it is plausible that the lost Ca was a result of a Ca-Al complex diffusing down a concentration gradient and out of the rhyolite, with the Ca coupled to the Al. The zero-value of CaAl_2O_4 suggests that a chemical potential gradient of the Ca-Al component developed as the experiment progressed. Although the CaAl_2O_4 profiles are complicated in these snapshots, it is noteworthy that the post-run gradients for the 12-hour run (figure 3.4c) are similar in sign and shape to those in the 24-hour run (figure 3.4d). Hence it appears that these gradients, once established, are maintained throughout the experiments and could be interpreted as indicative of long-lived chemical potential gradients that may be relevant to the isotopic results. A further significant feature is the large magnitude of the Ca isotopic effects, in comparison with the magnitude of the Ca and Al gradients, on the rhyolite side of the experiment. This hints that isotopic discrimination may be more pronounced in high- SiO_2 liquids than in low- SiO_2 liquids.

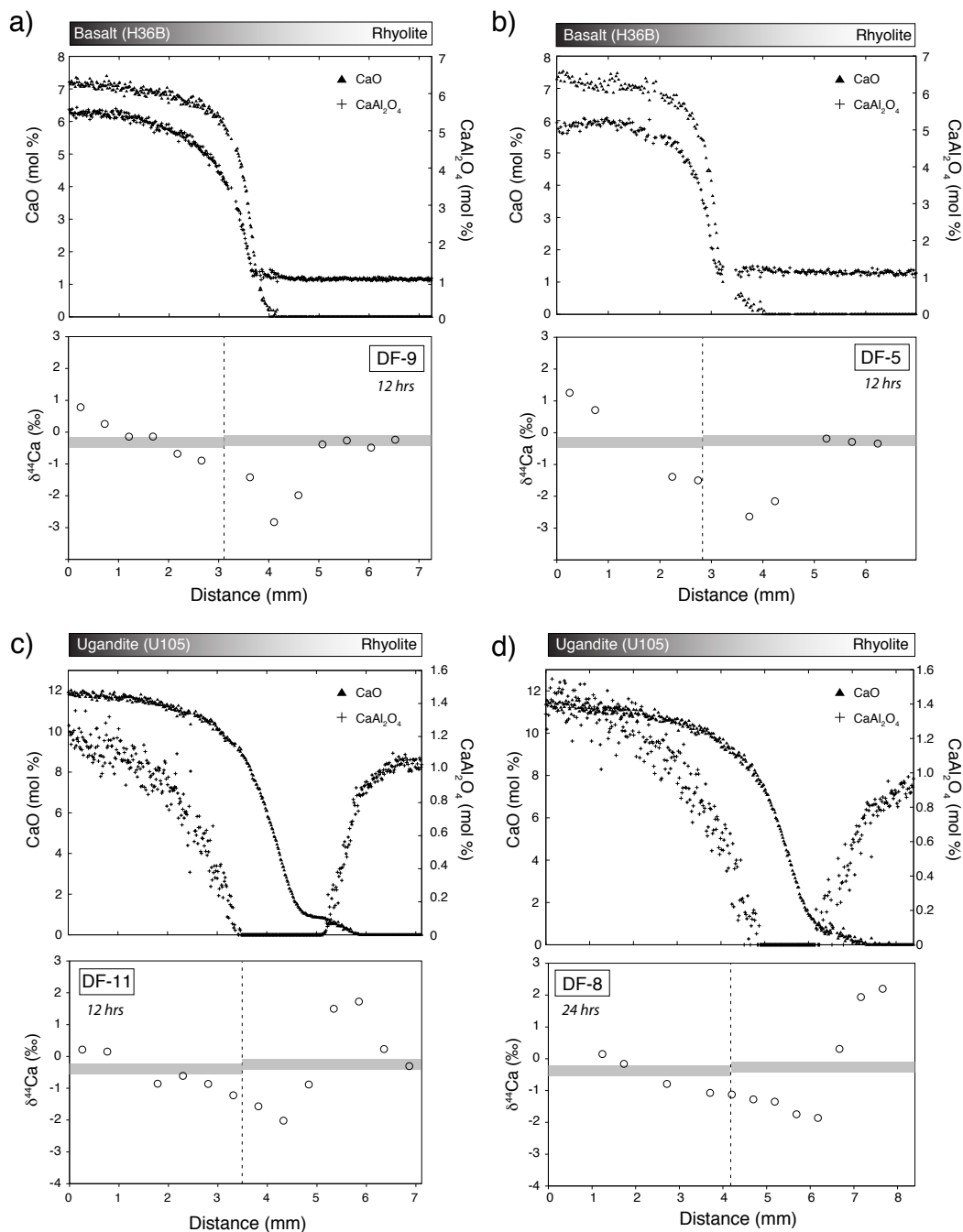


Figure 3.4: Major-element profiles from each of the diffusion couple experiments cast in terms components used in the Bottinga and Weill (1972) viscosity model. The post-run profiles for CaO and CaAl₂O₄ are compared to the Ca isotope profiles presented in figure 3.3. In the basalt-rhyolite experiments (3.4a and 3.4b), the gradients in both Ca species are unidirectional whereas in the ugandite-rhyolite experiments (3.4c and 3.4d), there are gradients in Ca species in both directions.

Overall the chemical data suggest that there could be both thermodynamic effects and simple coupling via a Ca-Al complex in the ugandite-rhyolite experiments. The contrasting behavior of the CaO and CaAl₂O₄ components in this experiment suggests that two separate Ca-bearing species are diffusing against each other in the liquid. In the following section we pursue the model of counter diffusion of two Ca species to evaluate how well that model can account for the isotopic results.

3.6 Theoretical Considerations

3.6.1 General multicomponent diffusion model

In a system of multiple diffusing components, the flux of one component may influence the flux of another and Fick's first law can be expressed as

$$J_i = \sum_{j=1}^{n-1} D_{ij} \nabla C_j \quad (3.7)$$

where D_{ij} is the multicomponent diffusion matrix. If diffusion of each component i is independent of all other components, then D_{ij} is a diagonal matrix. Generally, this is not the case in natural silicate liquids when individual elements or oxides are taken as the components, and the off-diagonal elements of D_{ij} specify the extent of diffusive coupling between these components.

If the diagonal or off-diagonal diffusion coefficients for a given element are mass dependent, then the flux of isotope k of element i can be written as (Liang, 1994; Richter et al., 1999):

$$J_{ik} = -D_k \nabla C_{ik} - \sum_{j=1}^{n-1} \chi_{ik} (D_{ij} - \delta_k D_k) \nabla C_j \quad (3.8)$$

where D_k is the self-diffusion coefficient of isotope k , C_{ik} is the concentration of k , and χ_{ik} is the mole fraction of k in element i . Equations 3.7 and 3.8 lead to the multicomponent diffusion equation with isotopes:

$$\frac{dC_i}{dt} = \nabla (D_k \nabla C_{ik}) + \sum_{j=1}^{n-1} \nabla (\chi_{ik} (D_{ij} - \delta_k D_k) \nabla C_j) \quad (3.9)$$

For our experiments, the appropriate boundary conditions are of zero flux into or out of either end of the capsule:

$$J_i = 0 \text{ at } x = 0 \text{ and } x = L. \quad (3.10)$$

Solving equation 3.9 requires knowledge of the diffusion matrix, which must be determined experimentally for a given composition (cf. Trial and Spera, 1994). Not only is D_{ij} not known for natural basalt or rhyolite, but D_{ij} is sensitive to composition between these two endmembers. Furthermore, because natural melts contain 8-12 oxide components, D_{ij} becomes prohibitively large to be forward-modeled. Therefore, implementing a full

multicomponent diffusion model that includes coupling between all major oxides is not practical. However, the essential behavior resulting from the coupling can be captured in a simplified model.

3.6.2 Simplified multicomponent diffusion model

Our goal is to obtain diffusion coefficients for Ca in a simplified model that takes into account the important observations that (1) Ca diffusion profiles are asymmetric and (2) that Ca diffuses against its own concentration gradient (assumed to be due to Ca-Al coupling) in the ugandite-rhyolite experiments. In our treatment that follows, we arbitrarily choose the simple oxides as components as is customary and for ease of comparison to other diffusion studies.

Based on qualitative assessment of the measured major-element and Ca isotopic profiles, we assume: (1) the rates of CaO diffusion are dependent mainly on the SiO₂ and Al₂O₃ content of the liquids such that we can treat the three oxides as a three-component system, (2) the diffusivities of SiO₂, Al₂O₃, and CaO are controlled by SiO₂ content as in RDDW, and (3) that CaO fluxes are coupled to Al₂O₃ gradients to allow for uphill diffusion of CaO in the ugandite-rhyolite experiments. The one-dimensional matrix representation of our system of equations is:

$$\begin{pmatrix} \frac{\partial C_{SiO_2}}{\partial t} \\ \frac{\partial C_{Al_2O_3}}{\partial t} \\ \frac{\partial C_{CaO}}{\partial t} \end{pmatrix} = \frac{\partial}{\partial x} \begin{bmatrix} D_{SiO_2} & 0 & 0 \\ 0 & D_{Al_2O_3} & 0 \\ 0 & D_{CaO-Al_2O_3} & D_{CaO} \end{bmatrix} \begin{pmatrix} \frac{\partial C_{SiO_2}}{\partial x} \\ \frac{\partial C_{Al_2O_3}}{\partial x} \\ \frac{\partial C_{CaO}}{\partial x} \end{pmatrix} \quad (3.11)$$

Note that the diffusion matrix is asymmetric, which in general is to be expected because of constraints such as local charge conservation; for example, one Ca atom coupled to two Al atoms in a species such as CaAl₂O₄. Also note that we allow Ca-Al coupling but not vice versa, and this is solely in order to minimize the number of free parameters (although the effect of Ca on the Al profile should be relatively small in comparison to coupling effects of other cations such as K and Na; Bottinga and Weill (1972).

To reproduce the asymmetry in the measured diffusion profiles, the D 's have a dependence on SiO₂ content that is parameterized as (RDDW):

$$D_{oxide} = D_{0,oxide} e^{-\alpha(X_{SiO_2}-0.5)} + D_1, \quad (3.12)$$

where X_{SiO_2} is the weight fraction of SiO₂ and $D_{0,oxide}$, α , and D_1 are fitting parameters for the major-element diffusion profiles. For simplicity, $D_{CaO-Al_2O_3}$ is assumed constant.

Referring to equation 3.9, we allow the diagonal and off-diagonal diffusion coefficients of ⁴⁰Ca and ⁴⁴Ca to differ by a constant factor. Expressing this difference in terms of the inverse mass ratio, we have two parameters β and γ defined as:

$$\frac{D_{^{44}CaO}}{D_{^{40}CaO}} = \left(\frac{40}{44} \right)^\beta \quad (3.13)$$

and

$$\frac{D^{44}\text{CaO-Al}_2\text{O}_3}{D^{40}\text{CaO-Al}_2\text{O}_3} = \left(\frac{40}{44}\right)^\gamma, \quad (3.14)$$

where β is the same as in equation 3.3 and γ describes the effect of diffusive coupling on the isotopes.

3.7 Numerical calculations

All numerical calculations were performed using the lattice Boltzmann (LB) model of Huber et al. (2008) developed for multi-component coupled diffusion. The LB method is a statistical approach to solving partial differential equations. It has been developed over the past two decades with a special emphasis on complex fluid dynamics and reaction-diffusion problems (Frisch et al., 1986; Qian et al., 1992; Chopard and Droz, 1998; Succi, 1991). Although LB models have been shown to be generally equivalent to explicit finite difference schemes, the LB diffusion models are unconditionally stable unlike finite difference models. Huber et al. (2008) showed that their multi-component coupled diffusion LB model is also unconditionally stable.

3.7.1 Model versus measured oxide profiles

The first step in modeling the major-element diffusion profiles is to obtain a reasonable approximation to the SiO_2 data. This provides the time-evolution of SiO_2 , which is necessary for modeling the asymmetric Al_2O_3 and CaO profiles with their SiO_2 -dependent diffusivities. After fitting the Al_2O_3 profile, we fit the CaO profile, which depends on the evolving SiO_2 and Al_2O_3 concentrations at each node. Lastly, we obtain parameters for the isotope profiles. To summarize:

1. Fit SiO_2 data (3 free parameters in D_{SiO_2}).
2. Fit Al_2O_3 data (3 free parameters in $D_{\text{Al}_2\text{O}_3}$).
3. Fit CaO data (3 free parameters in D_{CaO}).
4. Model the Ca isotope profile (2 free parameters β and γ).

Figure 3.5 compares model versus measured SiO_2 , Al_2O_3 and CaO diffusion profiles from the three sets of experiments discussed in this paper. The parameters used to model RB2 are the same as those given by RDDW and figure 3.5 shows that our numerical algorithm achieves the same fit for these profiles.

Figure 3.5 provides calculated diffusion coefficients and shows that our simplified 3-component diffusion model is able to capture the asymmetry and uphill diffusion of CaO in the measured profiles. It is also apparent, however, that our simplifying assumptions result in significant misfit to the data. For example, the model fails to reproduce the uphill diffusion of Al_2O_3 in the basalt-rhyolite experiments because Al_2O_3 fluxes are not coupled to gradients of any other oxides such as Na_2O and K_2O (in this case, coupling Al_2O_3 to CaO would be of little help since the CaO concentration gradients are small in this region).

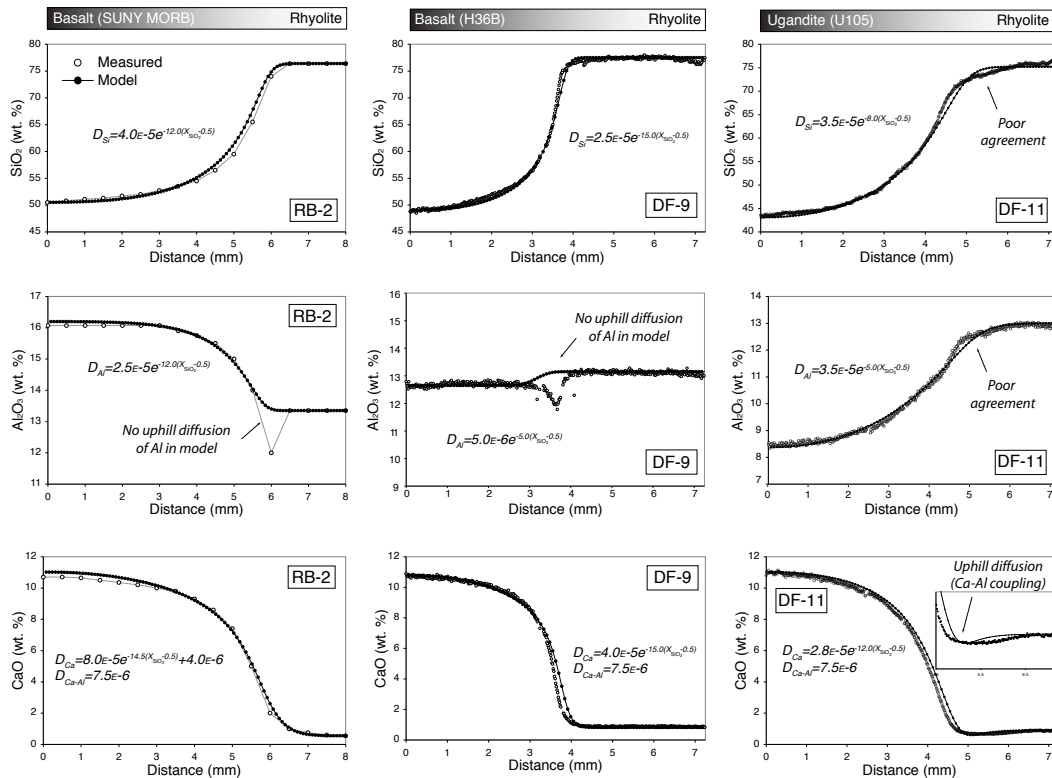


Figure 3.5: Model versus measured diffusion profiles for SiO_2 , Al_2O_3 , and CaO from the three sets of experiments. The model assumes three-component diffusion and includes diffusive coupling of CaO to Al_2O_3 . Diffusivity parameters for the model profiles are given in each panel in units of mm^2/s . Despite the relative simplicity of the model, a reasonable fit can be achieved for CaO , which is then used to generate the Ca isotopic profiles in figure 3.6.

Also, the SiO_2 and Al_2O_3 profiles of DF11 are poorly reproduced where there are unsmooth gradients (i.e., a sharp kink) and uphill diffusion in the rhyolite. The important point, however, is that the model produces the important characteristics of the CaO profiles, including the magnitude of uphill diffusion seen in the ugandite-rhyolite experiment (figure 3.5c). The misfit in the width of the uphill diffusing region can probably be attributed to the misfit in the Al_2O_3 gradients that our model fails to capture.

3.7.2 Model versus measured Ca isotope profiles

Beginning with the model major-element profiles, we incorporate the isotopic differences (described by β and γ) to produce a model isotopic profile. Figure 3.6 compares model versus measured isotopic profiles for the three sets of diffusion couples studied. The model succeeds in capturing the overall shape and parameters can be found to match the magnitude of the observed fractionations in each profile. In both DF9 and DF11, the disagreement between model and data on the rhyolite end may arise from our inability to successfully capture the corresponding gradients in the Al_2O_3 profiles. In all three sets of experiments, our model fails to reproduce the roughly linear isotopic gradients on the mafic end (which we address toward the end of this chapter).

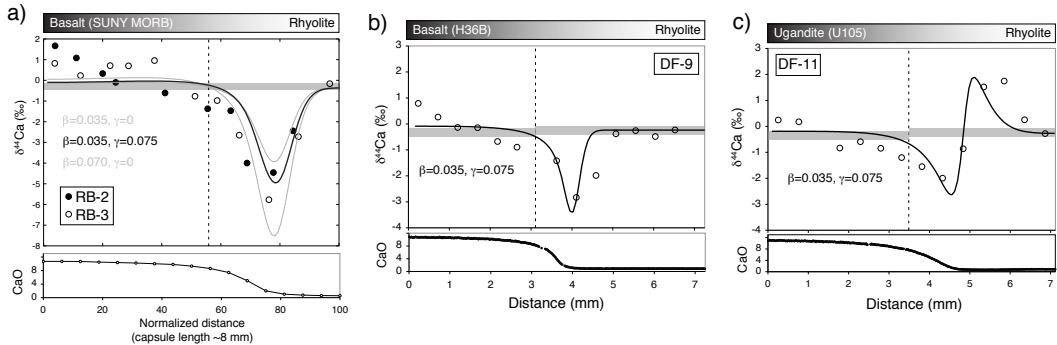


Figure 3.6: Model versus measured Ca isotope profiles for the three sets of experiments (labeled a, b, and c). Despite the relative simplicity of the model, the overall shape and magnitude of the fractionations are reproduced. The disagreement between model and data on the rhyolite end of the capsules may be related to the same region of the Al_2O_3 profiles in figure 3.5.

The simplified multicomponent diffusion model does provide some interesting and useful quantitative results. Using DF9 as a starting point, we find that $\beta=0.035$ (where γ is poorly constrained because there are essentially no Al_2O_3 gradients). In DF11, where Al_2O_3 gradients are large and opposite the CaO gradients, we can obtain values of $\beta=0.035$ and $\gamma=0.075$. Finally, in RB2 and RB3, we find that with diffusive coupling (and assuming $\gamma=0.075$), we calculate $\beta=0.035$, which is much different than the value calculated without diffusive coupling (i.e., $\beta=0.075$; RDDW).

To summarize, we can find a single set of parameters ($\beta=0.035$ and $\gamma=0.075$) to describe the fractionations in all of the profiles. We also find that γ is significantly

greater than β in the ugandite-rhyolite experiment, implying one or both of the following: (1) Ca-Al diffusive coupling discriminates between Ca isotopes more strongly than simple chemical diffusion or (2) mass discrimination by diffusion is more pronounced in the rhyolite where the coupling effects are being directly observed. We favor the latter interpretation for reasons discussed in the following section.

3.8 Discussion

Our experiments indicate that the isotopic effects associated with diffusion in silicate liquids are more complicated than has yet been appreciated. Nevertheless, the Ca, Mg, and Li results can be explained in a relatively straightforward manner in terms of two distinct diffusion mechanisms by which cations move.

3.8.1 Physical explanation for mass discrimination by diffusion

Dingwell (1990) suggested that the diffusive behavior of cations depends on the ratio

$$D_{cation}/D_{Eyring} \quad (3.15)$$

where D_{cation} is the cation bulk diffusivity and D_{Eyring} is the so-called Eyring diffusivity, which correlates with melt viscosity and is commonly used as a proxy for the mobility of the melt matrix. The Eyring diffusivity can be calculated from (Dingwell, 1990):

$$D_{Eyring} = \frac{kT}{\lambda\eta}, \quad (3.16)$$

where k is Boltzmann's constant, T is temperature in kelvin, λ is an effective jump distance (Dingwell and Webb, 1989), and η is melt viscosity.

Figure 3.7 embodies the physical description for cation diffusion described by Dingwell which, we argue, can explain the major features of diffusive isotopic fractionations discussed in this chapter. The figure compares D_{Si} , D_{Al} , D_{Ca} and D_{Eyring} versus melt viscosity across the ugandite-rhyolite diffusion couple. Also shown is D_{Li} from RB5. When D_{cation}/D_{Eyring} is large, as is the case for Li, the cation can be viewed as diffusing by site-hopping within and between quasi-static (glass-like?) structures. This is referred to as the intrinsic regime of diffusion (Dingwell, 2006), and in this regime, the diffusion of the species is largely independent of the movements of other atoms or multi-atom structures in the liquid. Consequently, the mass dependence of the diffusivity is closer to the $m^{-1/2}$ dependence (or in other words, the efficiency parameter E in equation 3.6 is relatively large (0.43 for Li), and the parameter n in equation 3.6 approaches zero).

In the other limit, as D_{cation}/D_{Eyring} approaches unity, cation motion is increasingly influenced by the continual rearrangement of the dynamic liquid matrix. This is the extrinsic end-member regime of diffusion (Dingwell, 2006), whereby cations not only site-hop among, but also translate with, larger structural units. In this regime E becomes small and nm (Equation 3.6) relatively large. The diffusion of Ca and Mg in basalt is in this extrinsic regime, as evidenced by the low values of $E \approx 0.07$ to 0.15.

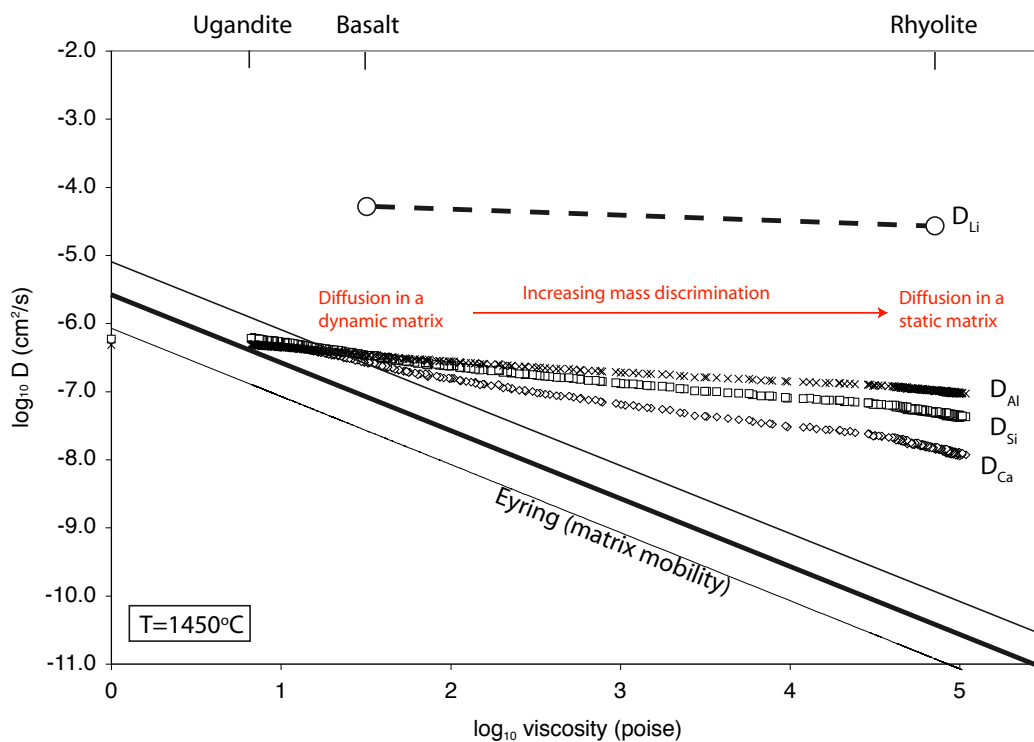


Figure 3.7: Diffusivities of Ca, Al, and Si (calculated from our diffusion model) as a function of melt viscosity (calculated using the model of Bottinga and Weill (1972) across a ugandite-rhyolite diffusion couple. Also shown are D_{Li} (from RDDW) and D_{Eyring} (using $l=1.4\text{\AA}$, the diameter of an oxygen anion) for the same experimental conditions. The ratio of D_{cation}/D_{Eyring} depends on the cation as well as melt viscosity, which can explain the diffusive isotopic fractionations observed (see text).

We therefore propose that D_{cation}/D_{Eyring} is a proxy for, and is correlated with, the efficiency or strength of mass discrimination for isotopes of diffusing cations in silicate liquids. Based on the dependence of D_{cation}/D_{Eyring} on the SiO_2 concentration of the liquid (Figure 3.7), mass discrimination by diffusion should increase in going from mafic to felsic liquid. This would help to explain the rather large isotopic effects in the rhyolite end of the ugandite-rhyolite couple.

It has previously been concluded that silicate liquids are not “molecular” liquids in the sense of organic polymers, but instead are dynamic in that viscous flow and diffusion of network-forming cations are dominated by continual making and breaking of bonds instead of molecular mechanisms of motion (Stebbins, 1995). Indeed, any individual bond, let alone a distinct structural unit or complex, probably lasts no longer than 10^{-4} - 10^{-5} s under our experimental conditions as evidenced by motional averaging in NMR studies (Stebbins, 1995). Nevertheless, our experiments clearly demonstrate that however transient their existence, the motion of complexes may be important for diffusion. One way to visualize this is by way of analogy to Mg and Li diffusion in aqueous solutions (Richter et al., 2006; Bourg and Sposito, 2007), where there is evidence from molecular dynamics simulations that the magnitude of isotopic discrimination is a function of the lifetime of water molecules in the first hydration shell around the cation. Applying this analogy to silicate liquids, the magnitude of diffusive isotopic fractionations exhibited by a particular cation should depend on the lifetime of its bond to local aluminosilicate structures and the size of those structures.

3.8.2 Silicate melt structures and diffusing components

Our isotopic results for Ca, which suggest a reinterpretation of the RDDW results as noted earlier, affect the calculated masses $(nm+m_1)^*$ in Table 1. We calculate a value for the on-diagonal terms affecting Ca of $\beta=0.035$ ($D_2/D_1=0.9965$) rather than the value of 0.075 ($D_2/D_1=0.993$) proposed by RDDW. Using equation 3.6, this translates into a maximum mass of 598. For the off-diagonal term, the calculated value is $(nm+m_1)^*=278$. The latter value is equal to, for example, the combined mass of Ca plus at least two $(\text{Al,Si})\text{O}_4$ units. This interpretation does not necessarily require that Ca diffusion involve the motion of long-lived Ca-bearing molecular complexes.

There are several additional lines of evidence to support the notion that molecular-scale structures may be important for diffusion in molten silicates. First, measured diffusion coefficients for a given oxide vary widely (an order of magnitude or greater) even in melts of the same SiO_2 content (e.g., Watson, 1982). Similar variability can depend on the direction of the oxide concentration gradient (e.g., der Laan et al., 1994) or whether the cation is present in major versus trace quantities (Baker, 1989; Leshner, 1994; der Laan et al., 1994). Each of these observations can be anticipated by appealing to diffusion driven by gradients in molecular complexes as opposed to gradients in the oxides. In one study where the choice of molecular components could be reasonably inferred, Kubicki et al. (1990) performed diffusion couple experiments using compositions near the diopside-anorthite join and were able to describe most of their data in terms of simple binary diffusion using diopside and anorthite as the diffusing components (cf. also Trial and Spera (1994) who emphasized the significance of this result). Kress and Ghiorso (1993) performed diffusion couple experiments

in the same system (CaO-MgO-Al₂O₃-SiO₂) and found similar results. In both studies, more complicated diffusion behavior arose when the endmember compositions did not lie on the anorthite-diopside join (i.e., one or both of the starting liquids had excess Ca, Mg, Al, or Si). In the latter study, Kress and Ghiorso (1993) attempted to reproduce anomalous features in their diffusion profiles by defining a different set of melt components (from educated guess) and they claim to have found some success using melt species that look like Mg₂Al₂O₅ and MgAl₂Si₂O₈.

A more quantitative approach for choosing diffusing components would be an eigen component analysis of the full diffusion matrix (cf. Trial and Spera (1994); Chakraborty et al. (1995); Liang et al. (1996) for discussions and applications of this approach). It has been shown that the full diffusion matrix (which is known for a very limited set of compositions in simplified systems) can be diagonalized (Cullinan, 1965) to decouple the set of differential equations describing diffusion. This takes into account all coupling between the oxides by creating new concentration variables (i.e., new components) whose stoichiometry is given by the coefficients in the eigenvectors. Is this approach merely a matter of convenience because the uncoupled set of differential equations are easier to solve (Trial and Spera, 1994) or do the independent components of diffusion have physical meaning in terms of the lengthscales of interatomic associations that define thermodynamic and/or transport properties? Since the masses we calculate for the diffusing species are comparable in size to common Ca-bearing mineral formula units (which in turn, are comparable in size to thermodynamic components employed in pMELTS; Ghiorso et al. (2002)), we speculate that interatomic associations extending about 3-10Å (roughly the unit cell dimensions of major minerals) from a central atom correspond to the lengthscales that determine both macroscopic thermodynamic properties (e.g., heat capacity, thermal expansivity, and compressibility) of silicate liquids as well as viscosity and the diffusion behavior of network-modifying cations.

3.8.3 Thermal gradients in the experiments

In all but one of the experiments shown in Figure 3.3, there are linear gradients in $\delta^{44}\text{Ca}$ on the mafic side of the diffusion couple that are unaccounted for in our chemical diffusion model. This issue was addressed by Richter et al. (2008) and it was concluded that these features represent isotope fractionations due to undesired temperature gradients across the sample capsule during the experiments. They supported this conclusion by first assuming that the temperature gradients were restricted to the basalt side; then, they avoided this portion of the furnace by using a shorter basalt-rhyolite diffusion couple (5mm instead of 10mm), and found that the linear isotopic gradients were no longer observed. In a subsequent study aimed at quantifying the ability of thermal gradients to separate isotopes of various elements, Richter et al. (2009) subjected basalt to a large known temperature gradient (about 110°C) and measured strikingly large Ca isotope fractionations of 6.4‰ per 100°C between the hot and cold ends of the capsule. From this, one obvious concern is that temperature effects are competing with and overprinting the isotopic effects due to chemical diffusion in our experiments.

To assess the effects of thermal gradients in our experiments, we performed an additional experiment wherein we placed basalt alone in the sample assembly and ran it

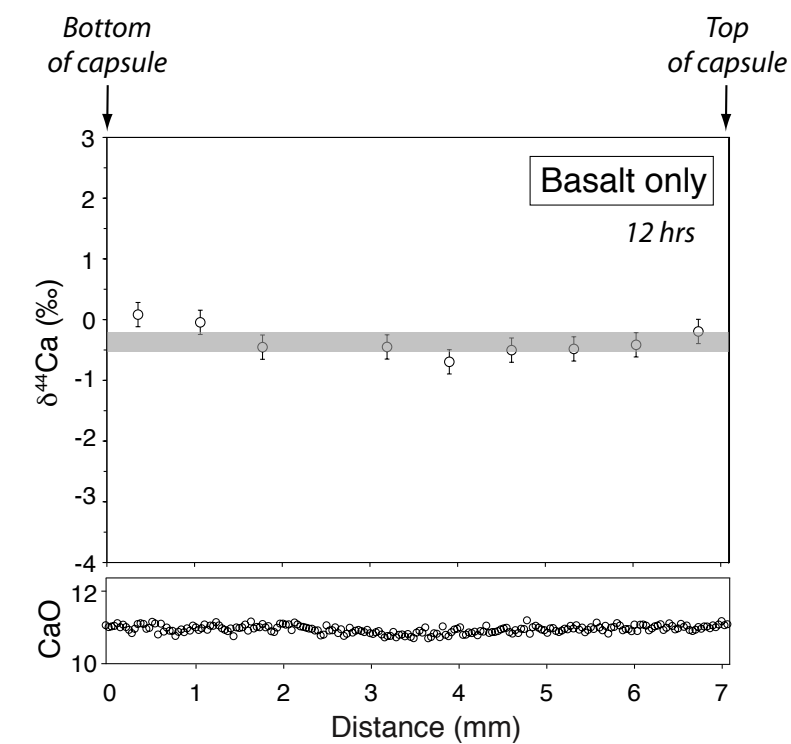


Figure 3.8: Results from an experiment to test temperature gradients across the diffusion couples. Basalt was placed in the experimental assembly exactly the way the basalt-rhyolite couples were. The data suggest that a the linear gradients we observe in the mafic end of our diffusion couples can be attributed in part to a temperature gradient of about 15°C (Richter et al., 2008). There are no discernible isotopic fractionations due to temperature gradients in the top half of the capsules (i.e., the rhyolite end).

under exactly the same conditions as all of our previous experiments. Figure 3.8 shows the results. We find that although there are isotopic effects that can only be attributed to temperature gradients, these are relatively minor. The total variation in $\delta^{44}\text{Ca}$ is about 1.0 ± 0.3 ‰, corresponding to a temperature difference of $\Delta T = 15 \pm 5^\circ\text{C}$ (a value that overlaps with direct measurements by spinel thickness thermometry for the piston-cylinder assembly used by Richter et al., 2009). Figure 3.8 also shows that the largest temperature gradients are at the bottom of the capsule (lefthand side of figure 9) where the isotopic effects are similar in magnitude to those in the ugandite-rhyolite experiments. However, they are far less pronounced than in the basalt-rhyolite experiments for reasons we do not understand. In figure 3.8, we do not see clear isotopic evidence for temperature gradients near the top of the capsule, in agreement with lack of isotopic gradients in the rhyolite end of each of the basalt-rhyolite experiments (figures 3a-3d). Richter et al. (2009) modeled the combined chemical and thermal diffusion problem and found that the minimum in $\delta^{44}\text{Ca}$ remains unaffected for any reasonable estimate of the temperature distribution in their experiments. Taking this and the observations listed above into account, we conclude that our calculated values for β and γ remain valid as estimates of the mass discrimination by diffusion.

3.9 Summary and conclusions

We performed superliquidus mafic-felsic diffusion couple experiments to investigate whether diffusive isotopic fractionations of Ca depend on liquid composition and therefore might be useful to probe silicate liquid structure and dynamics. The results indicate that the ability of chemical diffusion in silicate liquids to fractionate Ca isotopes is dependent on liquid composition, that there may be multiple diffusing Ca-bearing species in silicate liquids, and that these species may be multi-atom complexes that are sufficiently long-lived to affect Ca diffusion behavior. Evidence for strong coupling of Ca diffusion to Al diffusion is provided in two experiments involving a high-Ca, low-Al ugandite composition as the mafic end of the diffusion couple. The results from the ugandite experiments also suggest that isotopic discrimination by chemical diffusion is stronger in silica-rich, high viscosity liquids than in more silica-poor, low viscosity liquids.

To model the Ca isotope results we used a simplified 3-component diffusion matrix involving Ca, Al, and Si-oxides. We find that diffusive isotopic fractionations arise due to a mass-dependence of the diagonal as well as the off-diagonal terms of the diffusion matrix. Hence the isotopic discrimination for Ca isotopes cannot be described in terms of a single parameter, but requires at least two parameters - one being a function of Al concentration. We define two parameters β and γ that quantify the mass dependence of the diagonal and off-diagonal terms, respectively. A single set of β and γ values adequately describes the Ca isotope results from our experiments plus those of Richter et al. (2003), which together involve three different mafic liquid compositions differing mainly in their Al, Na, and K concentrations. Surprisingly, the magnitude of the off-diagonal parameter γ is about twice that of the on-diagonal parameter β . Hence when Al concentration gradients are in the same direction as Ca concentration gradients, Ca isotopic fractionation is enhanced, and when the two gradients are opposed Ca isotopic fractionation is reduced. In addition, an Al concentration gradient can generate Ca isotope fractionation even in the absence of a

Ca concentration gradient.

Our results imply that multi-atom molecular complexes may in some instances be the diffusing species in silicate liquids, even though spectroscopic studies indicate that such species have lifetimes that are not much longer than the jump frequency associated with Ca diffusion. This is an intriguing result that needs to be further investigated. The emerging view of silicate liquids from nuclear and vibrational spectroscopy, diffraction studies, and molecular dynamics simulations is that the structure of silicate liquids is constantly changing, with rapid breaking and re-forming of bonds, and a continual rearrangement of “species”. We reconcile this nanometer-picosecond view of silicate liquids with our results using the Dingwell (1990, 2006) model of extrinsic and intrinsic regimes of diffusion.

Under the experimental conditions ($T=1450^{\circ}\text{C}$ and $P=1\text{ Gpa}$) fast diffusing cations such as Li diffuse primarily by site-hopping (intrinsic regime) and exhibit large diffusive mass discrimination. Conversely, slower diffusing cations such as Ca and Mg diffuse by some combination of site-hopping and translating as part of larger structural units (extrinsic regime) and exhibit relatively small diffusive mass discrimination. However, the mass-discrimination for Ca appears to be enhanced in more polymerized liquids. The manner in which cations diffuse through some combination of intrinsic and extrinsic regimes is given by $D_{\text{cation}}/D_{\text{Eyring}}$, which is essentially the ratio of the cation jump frequency to the mobility of the melt matrix. Increased polymerization implies a small Eyring diffusivity (and large $D_{\text{cation}}/D_{\text{Eyring}}$), which translates to enhanced isotopic fractionations for more polymerized liquids.

The unexpected isotopic fractionation effects described here in mafic-felsic silicate liquid diffusion couples indicate that diffusive isotopic fractionation experiments in both natural and simpler synthetic liquids can provide new information about the way that silicate liquids are structured. The isotopic discrimination effects are complementary to other studies in that they isolate mass-dependent effects from other chemical effects, and they can be studied directly in the liquid state. Results from such studies may help eventually to provide a more comprehensive view of the relationships between atomic and molecular scale processes and macroscopic thermodynamic and transport properties.

3.10 Code validation

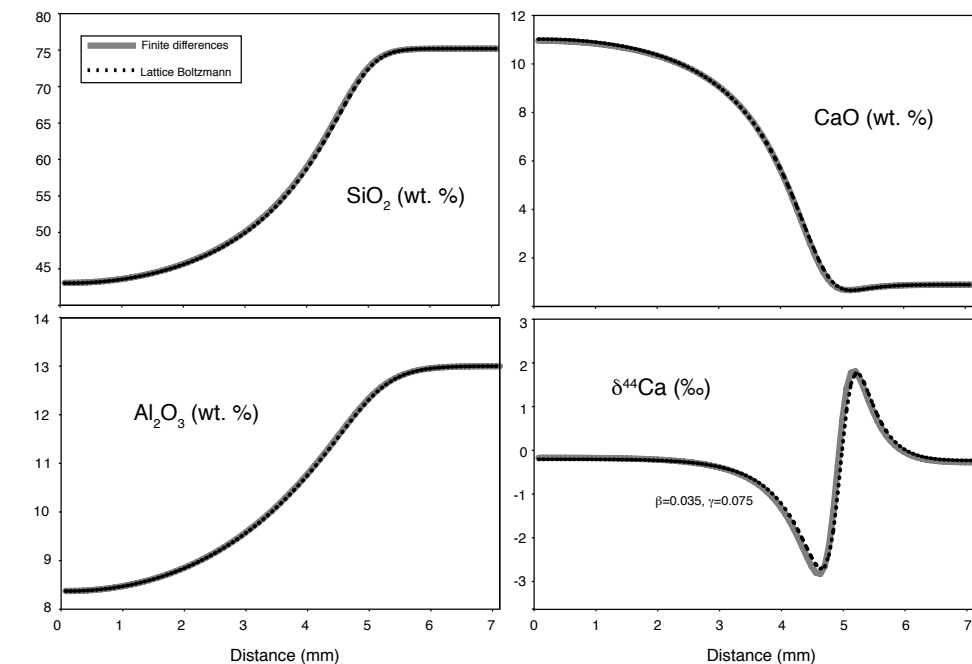


Figure 3.9: Model results using two different numerical algorithms: (1) finite differences coded by J.M. Watkins using MATLAB and (2) Lattice Boltzmann (LB) coded by C. Huber using C++. These solutions were obtained using a slightly different input parameter for the Ca-Al coupling: $D_{Ca-Al}=5 \mu\text{m}^2/\text{s}$ in the finite differences solution versus $D_{Ca-Al}=7 \mu\text{m}^2/\text{s}$ in the LB solution. This small discrepancy aside, the numerical schemes give nearly indistinguishable results, which we take to be a strong indication that the model results in this chapter are accurate.

Chapter 4

Isotope separation by diffusion in synthetic molten silicates

4.1 Introduction

In the previous chapter, we observed isotopic fractionations that suggested a composition-dependence to the diffusive isotope separation for calcium. In those experiments the compositional dependence was equivocal because of other possible contributing effects and the fact that natural silicate melt compositions are complicated. In this diffusion study we use silicate liquids of simple composition to further probe the compositional dependence of diffusive isotopic discrimination and its relationship to liquid structure. All of the starting materials are combinations of three mineral constituents anorthite ($\text{CaAl}_2\text{Si}_2\text{O}_8$; denoted AN), albite ($\text{NaAlSi}_3\text{O}_8$; denoted AB), and diopside ($\text{CaMgSi}_2\text{O}_6$; denoted DI), so that the resulting silicate liquids are considerably less complicated than natural basalt and rhyolite.

4.2 Experiments

Two diffusion couples; one consisting of AB and AN (1% AN versus 15% AN), and the other consisting of AB and DI (1% DI versus 15% DI) were constructed. The starting compositions are listed in table 4.1. The ends of the diffusion couple with a greater proportions of AN (or DI) has much higher Ca concentration than the AB-rich end, hence Ca diffuses down a substantial concentration gradient during the experiments. Albite was chosen as the main component of the liquids because of its relatively low melting temperature (1203°C at 8 kbar; Birch and LeComte (1960)), permitting us to use temperature and pressure conditions similar to previous experiments on natural magmatic compositions (Richter et al., 2003, 2008, 2009; Watkins et al., 2009). The variation in SiO_2 concentration among the synthetic starting compositions is also relatively small (Table 4.1). As diffusion coefficients for most elements in silicate liquids vary with the concentration of SiO_2 , this characteristic simplifies analysis as we can assume that the diffusion coefficients are uniform across the couple, and that they do not change over the course of the experiment.

		CaO	MgO	SiO ₂	Al ₂ O ₃	Na ₂ O	Total
85AB+15AN	Calculated	3.02	0.00	64.91	22.02	10.05	100.00
	Measured	3.04	-	63.70	22.15	9.80	98.69
99AB+01AN	Calculated	0.20	0.00	68.48	19.61	11.70	100.00
	Measured	0.33	-	68.30	19.75	10.80	99.18
85AB+15DI	Calculated	3.88	2.79	66.75	16.53	10.05	100.00
	Measured	3.75	2.60	66.00	16.80	9.65	98.80
99AB+01DI	Calculated	0.26	0.19	68.61	19.25	11.70	100.00
	Measured	0.37	0.30	67.70	19.30	10.90	98.57

Table 4.1: Targeted versus measured bulk compositions of starting materials used in diffusion couple experiments. The difference between the target (or calculated) compositions and those measured by electron microprobe is not an important factor for the purposes of this study.

4.3 Results

4.3.1 Major-element diffusion profiles

Figures 4.1 and 4.2 show the major-element diffusion profiles corresponding to the AB-AN and AB-DI experiments, respectively. In both experiments, Ca and Na are observed to diffuse more rapidly than the network-forming cations Si and Al. This difference is different from what is observed in natural silicate liquids under similar experimental conditions, where the length scales of Ca, Na, and Si diffusion are nearly identical (Richter et al., 2003, 2008, 2009; Watkins et al., 2009). In the AB-DI experiment, Mg diffuses more slowly than Ca and Na, its behavior resembling that of the network-forming cations. The slow diffusion of Mg relative to Ca has also been observed for tracer diffusion in liquids of nearly pure albite composition over the temperature range 645-1025°C (Rosalieb and Jambon, 2002).

4.3.2 Ca and Mg isotope profiles

Figure 4.3 shows the Ca and Mg isotopic composition along the diffusion profiles. As the isotopic composition is initially uniform across the two diffusion couples ($\delta^{44}\text{Ca} = -0.3\text{‰}$ and $\delta^{26}\text{Mg} = -1.2\text{‰}$), the observed isotopic variability develops as a result of diffusion during the experiment. In the AB-AN experiment (figure 4.3a), the variation in $\delta^{44}\text{Ca}$ of ca. 10‰ is the largest fractionation of Ca isotopes so far observed in such chemical diffusion experiments. In this experiment, the isotopic composition at the boundaries changed slightly from the initial condition, indicating that diffusive effects have reached both ends of the capsule. In the AB-DI experiment (figure 4.3b), the range in $\delta^{44}\text{Ca}$ is ca. 6‰, comparable to the maximum range previously observed in natural compositions, and the isotopic composition at both ends of the capsule is unchanged from the initial condition. In the same experiment, the range in $\delta^{26}\text{Mg}$ (figure 4.3c) is only ca. 1.3‰ and the length scale of Mg isotope variability from the initial state is comparable to that for Ca isotopes. In both experiments, the overall shape of the profiles match those expected for the simplest model of chemical diffusion in which Ca and Mg diffuse in response to their own concentration gradients.

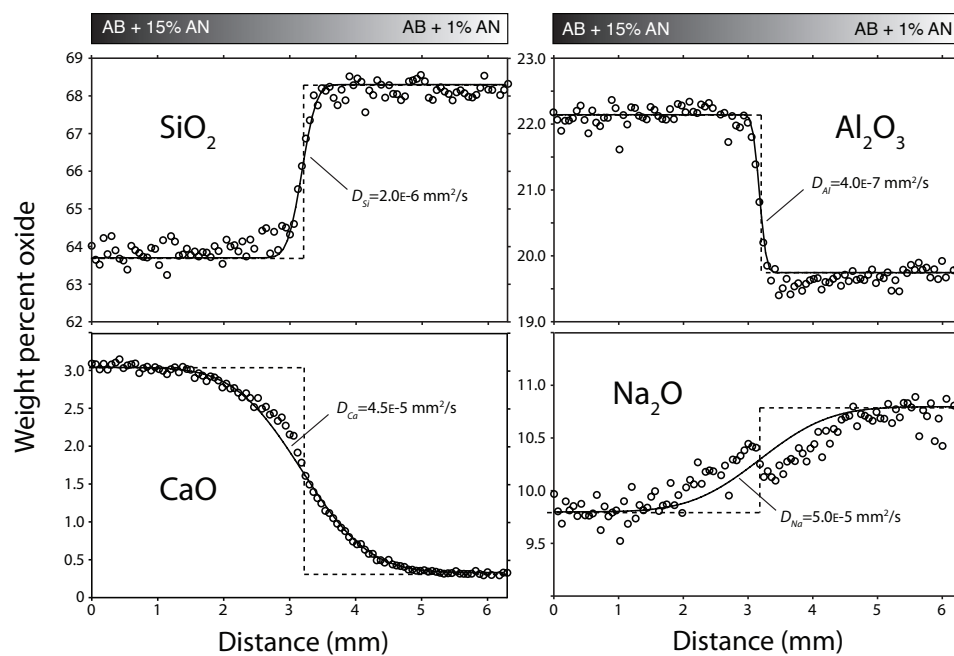


Figure 4.1: Diffusion profiles of major cations between two simplified molten silicate compositions along the albite-anorthite (AB-AN) join as measured by electron microprobe. Solid lines are model diffusion profiles and the dashed lines represent the starting concentrations and initial condition for the diffusion model. The diffusivity D_i of each of the major cations is roughly constant across the diffusion couple, as evidenced by the observed symmetry in each of the profiles about the initial interface between starting liquids.

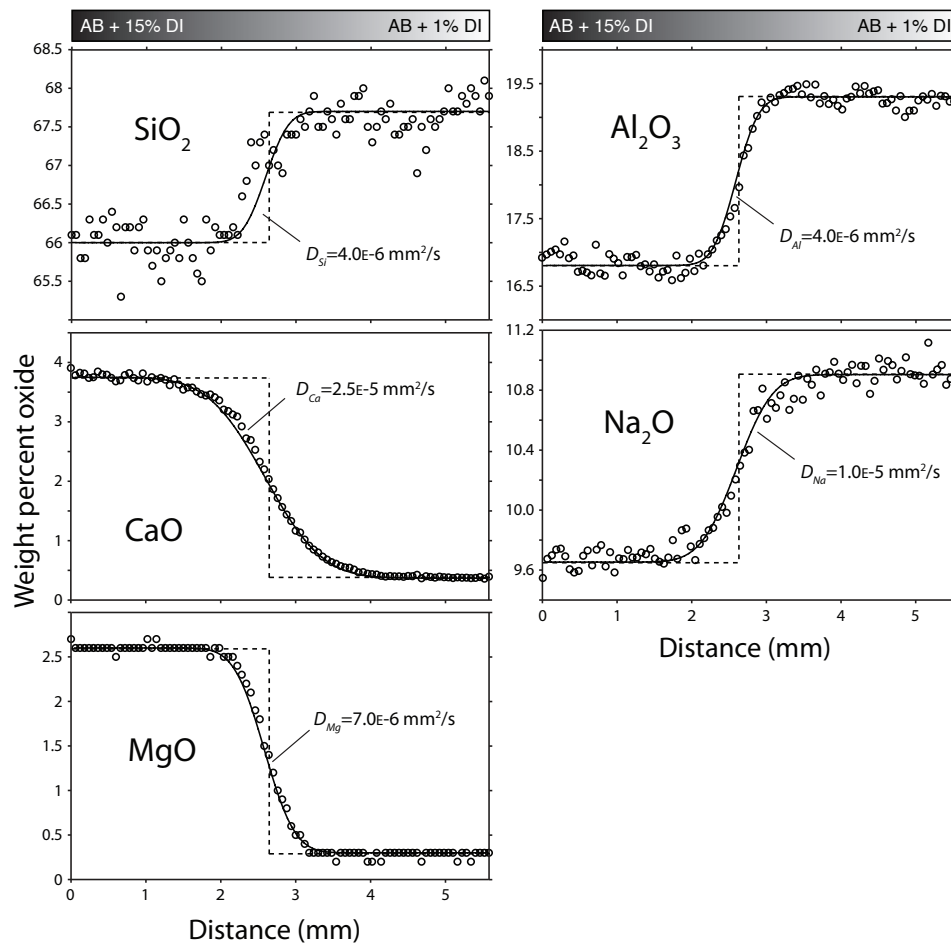


Figure 4.2: Same as figure 4.1 except here the starting compositions lie along the albite-diopside (AB-DI) join.

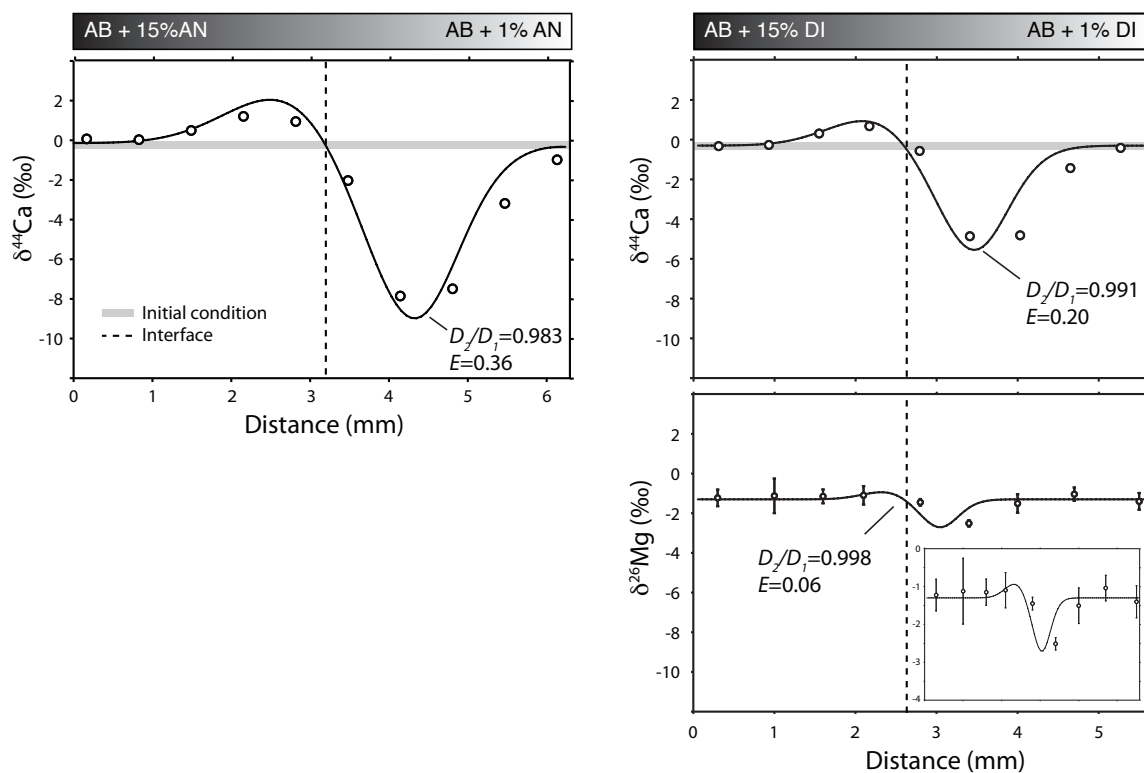


Figure 4.3: Calcium and magnesium isotope separation by diffusion in the AB-AN and AB-DI experiments. The initial isotopic composition is denoted by the grey horizontal line. Solid lines are model isotope profiles used to quantify the efficiency of isotope separation E , which is related to the ratio of isotopic diffusion coefficients (D_2/D_1).

Albite-Anorthite experiment					
Sample (wafer no.)	Distance (mm)	$\delta^{44}\text{Ca}^\ddagger$ (‰)	No. of analyses		
ABAN2-1	5.985	-0.98	3		
ABAN2-2	5.355	-3.19	2		
ABAN2-3	4.725	-7.49	3		
ABAN2-4	4.095	-7.86	2		
ABAN2-5	3.465	-2.03	3		
ABAN2-6	2.835	0.95	3		
ABAN2-7	2.205	1.21	2		
ABAN2-8	1.575	0.50	2		
ABAN2-9	0.945	0.03	2		
ABAN2-10	0.315	0.07	2		

Albite-Diopside experiment					
Sample (wafer no.)	Distance (mm)	$\delta^{44}\text{Ca}^\ddagger$ (‰)	No. of analyses	$\delta^{26}\text{Mg}$ (2σ) (‰)	No. of analyses
ABDI4-1	5.967	-0.42	2	-1.40 (29)	3
ABDI4-2	5.304	-1.43	3	-1.04 (34)	3
ABDI4-3	4.641	-4.82	2	-1.51 (47)	7
ABDI4-4	3.978	-4.86	2	-2.51 (16)	2
ABDI4-5	3.315	-0.57	3	-1.45 (17)	3
ABDI4-6	2.652	0.68	2	-1.10 (47)	2
ABDI4-7	1.989	0.31	2	-1.15 (---)	1
ABDI4-8	1.326	-0.27	2	-1.12 (87)	3
ABDI4-9	0.663	-0.33	2	-1.23 (42)	3

‡ Uncertainties in $\delta^{44}\text{Ca}$ are within $\pm 0.15\%$.

Table 4.2: Ca and Mg isotope compositions measured on post-run diffusion couples.

4.4 Analysis

The essential and unexpected result of the experiments described above is that the Ca isotopic separation due to diffusion in chemically simple diffusion couples is both larger than observed in natural volcanic liquids (Richter et al., 2003; Watkins et al., 2009, e.g.,) and variable. It was originally postulated by Richter et al. (2003) based on the data available, that the Ca isotopic selectivity due to diffusion in silicate liquids might be roughly constant; that is, independent of liquid composition. Watkins et al. (2009) provided evidence that the isotopic selectivity might be more pronounced in high silica liquids, but the complexity of the experimental results did not allow for more definitive conclusions. The present results, however, show unequivocally that Ca isotope fractionation during diffusion can be highly variable. In the following section we analyze this variability and show that the efficiency of isotope separation appears to be correlated with both the magnitude of the diffusivity, and more precisely, the ratio of the Ca diffusivity to that of Si. The systematic relationships we have discovered allow us to move closer to a general model of isotopic fractionation during diffusion in silicate liquids, and also shed light on the bonding of cations within these liquids and the structure of the liquids themselves.

4.4.1 Model for the elemental diffusion profiles

For diffusion in a multicomponent system, the flux-density J_i for the i th component is given by:

$$J_i = \sum_{j=1}^{n-1} D_{ij} \nabla C_j \quad (4.1)$$

where D_{ij} is the multicomponent diffusivity matrix and C_j is the concentration of component j in volume-normalized units. When the diffusivity matrix is not known, as is the case in our systems, a simplified effective binary diffusion model (Cooper, 1965) is typically employed, in which the flux density J_i is given by:

$$J_i = D_i \nabla C_i, \quad (4.2)$$

where D_i is referred to as the effective binary diffusion coefficient (EBDC). The effective binary model ignores coupling between chemical components but provides a useful estimate of mobility. Since our experiments were designed so that we could assume a constant D_i , mass conservation leads to the following one-dimensional diffusion equation:

$$\frac{\partial C}{\partial t} = D_i \frac{\partial^2 C}{\partial x^2} \quad (4.3)$$

Given that the initial condition is a step function in concentration and assuming a fixed concentration at the boundaries (this is only approximately correct), the analytical solution to equation 4.3 yields the concentration profile:

$$C_i = \frac{C_{i,L} + C_{i,R}}{2} + \frac{C_{i,R} - C_{i,L}}{2} \operatorname{erf} \left(\frac{x}{2\sqrt{D_i t}} \right) \quad (4.4)$$

where $C_{i,L}$ and $C_{i,R}$ are the initial concentrations of component i in the two starting liquids, and D_i is the only unknown (Zhang, 2008). In equation 4.4 the zero x-coordinate is defined as the position of the interface between the liquids. Model versus measured diffusion profiles for Ca, Mg, Na, Al and Si and the associated diffusion coefficients for both diffusion couples are shown in Figures 4.1 and 4.2. The contrast between Ca and Si diffusivity is largest in the AB-AN experiment where the diffusivity of Ca is greater than that of Si by a factor of 22.5 ($D_{Ca}=4.5E-5$ mm²/s and $D_{Si}=2.0E-6$ mm²/s). In the AB-DI experiment, where the primary difference is the addition of Mg, the diffusivity of Ca is reduced ($D_{Ca}=2.5E-5$ mm²/s) and the diffusivity of Si is increased ($D_{Si}=4.0E-6$ mm²/s) such that D_{Ca}/D_{Si} is about 6. This latter value is still large in comparison to D_{Ca}/D_{Si} in natural silicate liquids, which is close to unity. In the same experiment, the diffusivity of Mg is less than that of Ca yet similar to that of Si ($D_{Mg}/D_{Si}\sim 1$).

4.4.2 Model for the isotope ratio profiles

The Ca and Mg isotope ratio profiles require that the diffusion coefficients for the isotopes of Ca vary with mass. To model the profiles, each isotope is treated as an independent component, and the ratio of isotopic diffusion coefficients is constant. A single parameter, E can describe the efficiency of isotope separation:

$$E = \frac{(D_2/D_1) - 1}{(m_1/m_2)^{1/2} - 1}, \quad (4.5)$$

where m_i and D_i are the mass and diffusivity, respectively, of isotope i (Schoen, 1958). This parameter is related to the analogous parameter β used by Richter et al. (2003), by the simple relationship $E=2\beta$. The magnitude of E is affected by the number and masses of other atoms whose motions are correlated with the motion of the atom of interest. Larger values of E correspond to greater mass discrimination between isotopes and imply that the diffusing atom is decoupled from the motion of other atoms (Rothman and Peterson, 1965). The value of E approaches unity for diffusion in gases but is generally much smaller in liquids and solids. Values for D_2/D_1 (i.e., D_{44Ca}/D_{40Ca}) can be obtained from the model fit to the isotopic profiles and E derived from equation 4.5 and the isotopic masses of Ca.

4.4.3 Comparison between model and measured isotope profiles

The model profiles with corresponding values of E are compared to the measured isotope profiles in figure 4.3. The overall shape of the model profiles and magnitude of the fractionations are in especially good agreement with the data in these simplified systems. Of particular significance is the nearly exact fit of the $\delta^{44}Ca$ data on the high-Ca side of both experiments, because in most of the experiments conducted using natural basalt-rhyolite diffusion couples, linear variations in $\delta^{44}Ca$ have been observed in the high-Ca end that could not be accounted for with a simplified chemical diffusion model (Richter et al., 2003). Such variations have been attributed to undesired temperature gradients in the experimental capsules because temperature gradients can produce a similar isotopic signature (Richter et al., 2008). However, our failure to observe linear variations in $\delta^{44}Ca$ in the AB-AN and AB-DI experiments, and in an isochemical experiment under the same

conditions (Watkins et al., 2009), suggests that these unexpected isotopic effects in the natural systems have other causes. We postulate that they are related to chemical mixing and configurational entropy production near the interface of the diffusion couple since these effects are only observed when the starting compositions are significantly different in bulk composition. However, since this hypothesis does not bear directly on the AB-AN and AB-DI experimental results, we leave it as the focus of a future study.

The misfit between model and data in the location of the lightest $\delta^{44}\text{Ca}$ values likely represents isotopic exchange superimposed on chemical diffusion, which is not accounted for in the effective binary diffusion model. It has been shown that isotopic homogenization is generally more efficient than elemental homogenization by diffusion in silicate liquids (Leshner, 1990; der Laan et al., 1994), and hence if anything the isotope profiles should be (and are) more advanced than the elemental profiles. Furthermore, it is noteworthy that this feature is common to the experiments using natural silicate liquid compositions (Watkins et al., 2009). For present purposes, we emphasize that the overall agreement between model and data is good and assume that accounting for isotopic exchange would not significantly alter the derived values of E .

4.5 Discussion

4.5.1 Isotope separation by diffusion in silicate melts

Our results demonstrate, in contrast to previous proposals (Richter et al., 2003; Watson and Muller, 2009) that diffusive isotopic separation for Ca is sensitive to even slight changes in liquid composition. The compositions of the diffusion couples are similar in terms of SiO_2 content, and yet E for Ca varies from 0.20 in the AB-DI experiment to 0.36 in the AB-AN experiment. Both values are significantly greater than that found in natural silicate liquid experiments ($E=0.07$ to 0.15), and show that there is no single value of E that can describe the diffusive fractionation behavior of Ca isotopes in silicate liquids. E_{Ca} does, however, appear to be strongly correlated with the ratio $D_{\text{Ca}}/D_{\text{Si}}$ (Figure 4.4), which represents the ratio of the diffusivity of a “solute” component relative to that of the “solvent” component, in this case represented by Si. Among the silicate melt compositions for which diffusive fractionation of calcium has been measured, $D_{\text{Ca}}/D_{\text{Si}}$ varies by a factor of ~ 200 and E varies systematically between 0.07 and 0.36. The variation in D_i/D_{Si} is even larger, ~ 1000 , if experimental data for Ca, Mg, Fe and Li are considered, and the strong correlation between E_{solute} and D_i/D_{Si} , suggests that D_i/D_{Si} is an excellent predictor of the magnitude of the isotope effect in silicate liquids.

4.5.2 Isotope separation by diffusion in aqueous solutions

The results from silicate liquid experiments are combined with results from experiments on cation diffusion in aqueous solutions in Figure 4.4. To generalize the terminology we plot E versus the ratio $D_{\text{solute}}/D_{\text{solvent}}$ where the solvent is H_2O in the aqueous solution case and the aluminosilicate matrix in the silicate liquid case. For D_{solvent} we use the self-diffusion coefficient of H_2O (Bourg and Sposito, 2007) and the measured diffusion coefficient of Si. For the aqueous solutions, $D_{\text{H}_2\text{O}}$ is constant for a given temperature, so

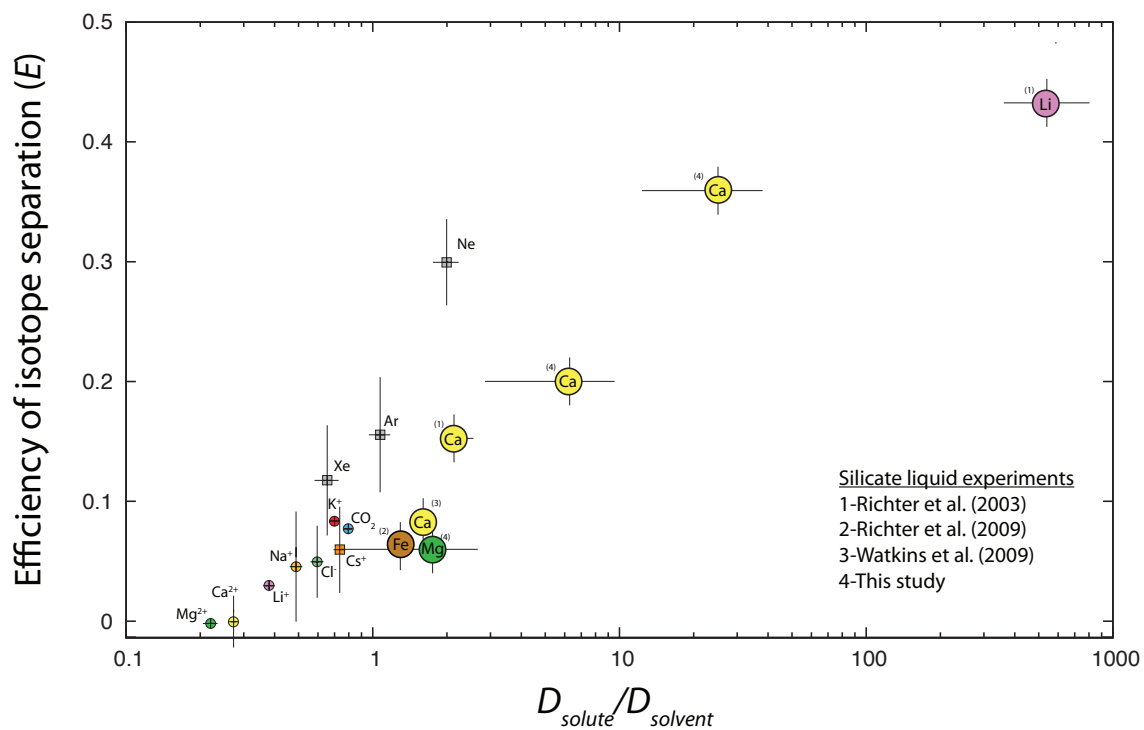


Figure 4.4: The observed relationship between the efficiency of isotope separation E and the mobility of the diffusing cation (D_{cation}) relative to the mobility of the liquid matrix ($D_{solvent}$) in aqueous solutions (small symbols) and silicate liquids (large symbols). The subscript solvent refers to H_2O in aqueous solutions and Si (or SiO_2) in silicate liquids.

Diffusing medium	Experiment No.	Description	Isotopic system	$D_{\text{solid}} \cdot 10^{11}$ (m ² /s)	$D_{\text{liquid}} \cdot 10^{11}$ (m ² /s)	E	References
Natural volcanic liquids	DF-9	basalt-rhyolite	⁴⁴ Ca/ ⁴⁰ Ca	0.36	0.23	0.15±0.01	Watkins et al. (2009)
	RB-2	basalt-rhyolite	⁴⁴ Ca/ ⁴⁰ Ca	1.3	0.59	0.07±0.01	Richter et al. (2003)
	RB-X	basalt-rhyolite	²⁶ Mg/ ²⁴ Mg	N/A	1.1	0.10±0.01	Richter et al. (2008)
	RB-5	basalt-rhyolite	⁷ Li/ ⁶ Li	320	0.59	0.44±0.01	Richter et al. (2003)
	RB-X	basalt-rhyolite	⁵⁶ Fe/ ⁵⁴ Fe	1.4	1.1	0.06±0.01	Richter et al. (2009)
	AB-AN	albite+anorthite	⁴⁴ Ca/ ⁴⁰ Ca	5.0±0.5	0.2±0.1	0.38±0.01	This study
Simple silicate liquids	AB-DI	albite+diopside	⁴⁴ Ca/ ⁴⁰ Ca	2.5±0.5	0.4±0.2	0.20±0.01	This study
	AB-DI	albite+diopside	²⁶ Mg/ ²⁴ Mg	0.7±0.2	0.4±0.2	0.06±0.01	This study
Diffusing medium	Experiment No.	Description	Isotopic system	$D_{\text{solid}} \cdot 10^9$ (m ² /s)	$D_{\text{liquid}} \cdot 10^9$ (m ² /s)	E	References
Liquid water (25°C)	-	MD simulation	He	7.85±0.54	2.4±0.1	0.342±0.056	Bourg and Sposito (2008)
	-	MD simulation	Ne	4.78±0.37	2.4±0.1	0.300±0.036	Bourg and Sposito (2008)
	-	MD simulation	Ar	2.57±0.15	2.4±0.1	0.156±0.048	Bourg and Sposito (2008)
	-	MD simulation	Xe	1.57±0.11	2.4±0.1	0.118±0.046	Bourg and Sposito (2008)
	-	Experiment	²⁶ Mg/ ²⁴ Mg	1.21±0.06	5.5±0.1	0.000±0.003	Richter et al. (2006); Bourg and Sposito (2007)
	-	Experiment	⁷ Li/ ⁶ Li	2.09±0.08	5.5±0.1	0.030±0.004	Richter et al. (2006); Bourg and Sposito (2007)
Liquid water (75°C)	-	Experiment	³⁷ Cl/ ³⁵ Cl	3.27±0.14	5.5±0.1	0.050±0.030	Richter et al. (2006); Bourg and Sposito (2007)
	-	MD simulation	Na	2.69±0.14	5.5±0.1	0.058±0.044	Bourg et al. (2010)
	-	Experiment	²⁴ Na/ ²³ Na	-	-	0.046±0.046	Plkal (1972)
	-	MD simulation	K	3.85±0.17	5.5±0.1	0.098±0.034	Bourg et al. (2010)
	-	Experiment	⁴¹ K/ ³⁹ K	-	-	0.084±0.004	Bourg et al. (2010)
	-	MD simulation	Cs	4.04±0.20	5.5±0.1	0.060±0.036	Bourg et al. (2010)
	-	MD simulation	Ca	1.50±0.03	5.5±0.1	0.000±0.022	Bourg et al. (2010)
	-	Experiment	⁴⁴ Ca/ ⁴⁰ Ca	-	-	0.009±0.001	Bourg et al. (2010)
	-	MD simulation	Li	2.12±0.08	5.5±0.1	0.034±0.032	Bourg et al. (2010)
	-	Experiment	¹⁸ O/ ¹⁶ O	7.22±0.27	2.4±0.1	0.077±0.004	Jähne et al. (1987)
-	Experiment	⁴ He/ ³ He	1.91±.073	2.4±0.1	0.97±0.18	Jähne et al. (1987)	

Table 4.3: Values and associated references used in the compilation of figure 4.4.

the data indicate that there is a correlation between E and diffusivity of the solute. For the silicate liquids, D_{Si} is variable so there is not a one-to-one correspondence between D_{solute} and $D_{solute}/D_{solvent}$.

In the case of ions in aqueous solution, recent studies offer a molecular scale explanation of the pattern shown in Figure 4.4. The efficiency of isotope separation for a cation (and its diffusivity) correlates with the residence time of water molecules in its first solvation shell as determined from molecular dynamics simulations (Bourg and Sposito, 2007). If the water molecules are weakly bound, as for Li^+ , it implies that the ion can move through the liquid as a single atom and therefore the isotopic effect and the diffusivity is determined largely by the mass of the atom. If one or more water molecules are affixed to the ion, the effective mass of the diffusing species is larger than that of the ion. The actual situation is somewhere in between, where the ion spends part of the time isolated and part of the time bound to water molecules. If the hydration shell is massive enough, and the lifetime of the water molecules in the hydration shell long enough, the isotopic effect tends toward zero, as seems to be the case for aqueous Mg^{2+} . It should be noted that in the cases of Mg^{2+} , Ca^{2+} , K^+ , and Li^+ , the ratio of the diffusion coefficients for the isotopes has been measured experimentally, whereas the lifetime of water molecules in the hydration shell has been estimated using molecular dynamics models.

The translation of this general principle to the case of silicate liquids is only approximate, and has not yet been verified by molecular simulations. In the situation where the diffusivity of an element (like Li in natural liquids, or Ca in the AB-AN experiment) is much greater than the diffusivity of Si, it is likely that the element is not strongly bound to the aluminosilicate matrix, and hence is diffusing mostly as an isolated atom through a quasi-stationary aluminosilicate framework. This condition results in the large values for E_{Li} and E_{Ca} . For elements like Ca, Mg, and Fe in basaltic liquids, where the diffusivities are approximately the same as that of Si, these elements must be more strongly bound to the aluminosilicate matrix and hence are diffusing effectively as part of more massive multi-atom complexes that include Si. This range of diffusion behavior in silicate liquids and its explanation has been described previously (Dingwell, 1990) and we now can see that the isotopic effects follow logically at least at a qualitative level.

An important difference between aqueous solutions and silicate liquids is that ions in aqueous solution typically diffuse more slowly than H_2O , whereas elements in silicate liquids diffuse faster than Si. For aqueous solutions this effect may be due to charge balance constraints in addition to hydration, and the fact that water molecules are weakly bound to each other. In silicate liquids, Si is strongly bound in multi-atom complexes with O (as well as Al and other Si atoms), so it diffuses more slowly than other elements. The average size and lifetime of these Si-O complexes varies with liquid composition and could account for the variations in D_{Si} .

4.6 Summary and conclusions

We performed superliquidus diffusion-couple experiments using simplified synthetic silicate liquids in order to investigate why the efficiency of isotope separation by diffusion varies between cations and in liquids of different composition. Two diffusion ex-

periments were conducted using combinations of the mineral constituents albite, anorthite and diopside. For both experiments, a simplified chemical diffusion model was used to quantify cation diffusivities (D_{cation}) and the efficiency of isotope separation (E).

Model results indicate that a relationship exists between the efficiency of isotope separation E and the normalized diffusivity - the ratio of the mobility of the cation (D_{cation}) to the mobility of the liquid matrix (D_{Si}). Where $D_{cation} \approx D_{Si}$, isotope separation by diffusion is less efficient because the cation is likely to be more strongly bound to the aluminosilicate matrix, and hence, the mass difference between isotopes is effectively reduced because the cation is associated with a larger complex that includes Si. Conversely, where $D_{cation} \gg D_{Si}$, isotope separation by diffusion is more efficient because it is likely that the element is not strongly bound to the aluminosilicate matrix and is diffusing mostly as an isolated atom through a quasi-stationary aluminosilicate framework.

This interpretation offers a plausible explanation for why diffusive isotope effects are greater in silicate liquids at 1450°C than in aqueous solutions at 25-75°C. In silicate liquids, the solvent is mainly silicon in the form of silica tetrahedra, which are generally less mobile than the other cations; that is, $D_{cation}/D_{solvent}$ is generally greater than unity. In aqueous solutions, by contrast, the solvent water molecules are generally more mobile than the diffusing ions owing to relatively strong interactions between ions and their surrounding water molecules.

Our empirical result also provides a context for discussing diffusive isotope effects in natural geologic environments. It is now recognized that kinetic isotope separations can be relatively large, even at the high temperatures associated with molten silicates, and our results indicate that these effects are likely to be greater in high-SiO₂ liquids than in low-SiO₂ liquids. At present there are only a few documented instances of diffusive isotope effects in natural rocks - mostly in mafic systems - and future stable isotope studies will doubtless uncover much more isotopic variability. Quantifying these effects will require a combination of experiments and molecular-scale modeling in order to better understand and/or characterize the efficiency of isotope separation for different isotope pairs under different conditions. This information in turn will be useful for assessing the effects of diffusion and extent of isotopic disequilibrium during crystallization, mineral dissolution, and chemical alteration on the differentiation of silicate liquids that solidify to form igneous rocks.

4.7 Comment on multicomponent diffusion models

In the AB-AN system, which contains four oxide components, a 3×3 matrix is required to describe all of the diffusive fluxes and there are nine free parameters in the multicomponent diffusion model as opposed to just one free parameter in the effective binary diffusion model. With this many free parameters, it is not possible based on one experiment to obtain a unique diffusivity matrix for describing the diffusion profiles. To illustrate this point, figure 4.5 compares data from the AB-AN experiment to two model diffusion profiles generated using two completely different diffusion matrices (see figure 4.5 legend). As can be seen, the two model profiles are indistinguishable, and since both fit the data equally well, the physical meaning of the values in either of the diffusivity matrices is

at best ambiguous.

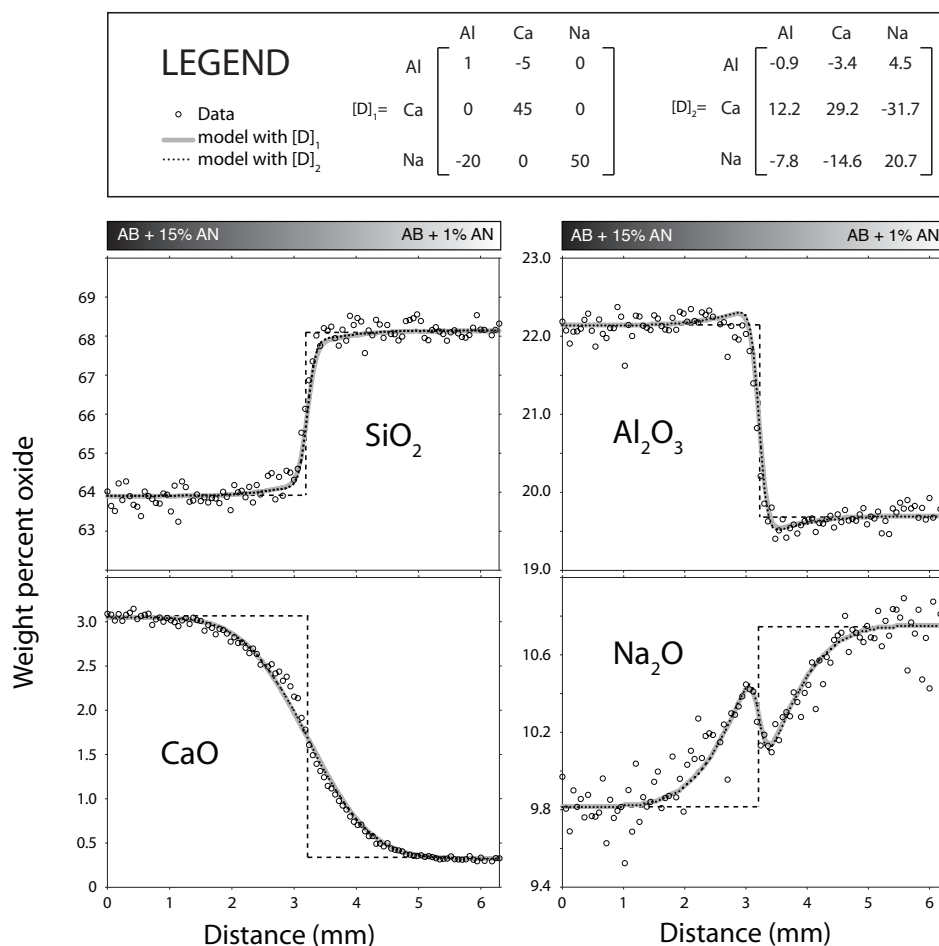


Figure 4.5: Results from model diffusion profiles that allow for diffusive coupling between chemical components. Two different sets of parameters (i.e., diffusion matrices) provide nearly identical fits to the measured profiles. This shows that the solution to the multicomponent diffusion problem based on one experiment is under-constrained.

The next immediate question is what would it take to obtain a physically meaningful diffusivity matrix? Trial and Spera (1994) argued that in an n -component system, at least $(n-1)$ cleverly designed diffusion-couple experiments are required to adequately constrain the “true” diffusion coefficients in the diffusivity matrix. Clearly, a significant effort must be expended in order to obtain the full diffusivity matrix for a given bulk composition. For this reason, and to our knowledge, the full diffusivity matrix has been obtained only in silicate liquid systems with three or fewer components (e.g. Liang et al., 1996; Chakraborty et al., 1995). The systems in this study contain four or more oxide components, and although it would require significant effort, it is certainly within our capacity to determine a unique diffusivity matrix corresponding to the average compositions in the AB-AN and

AB-DI diffusion couples. However, the effort required to do so is not the only deterrent.

Assuming one knew the full diffusivity matrix for the AB-AN and AB-DI systems, the picture would be further complicated by the fact that each coefficient in that matrix should have a dependence on mass. For a 3×3 matrix there would be 9 values of E . This doubles the number of free parameters required in order to fit the isotopic ratio profile and it is not clear whether a unique solution could be obtained for the isotope profile. The bottom line is that a more complicated diffusion model would significantly complicate the analysis and interpretation when our goal is to use the simplest diffusion model that permits us to generalize our results as much as possible beyond the specific experimental conditions. While using a full diffusivity matrix to model the isotope profiles may be an informative undertaking in a future study, the effective binary approach is arguably the best course of action for obtaining fits to the profiles, save for instances in which the data warrant a model that is more complex.

Chapter 5

Chemical, Tracer and Soret diffusion

5.1 Isotopic exchange superimposed on chemical diffusion

The traditional formulations of chemical diffusion - Fick's Laws - do not specifically account for the fact that chemical elements have isotopes, but it has been shown by our experiments in the previous chapters that isotopic species diffuse at different rates depending on mass, with especially large effects being generated in silicate liquids. To model these effects, we have thus far treated each isotope as an independent chemical species, diffusing in response to its own chemical gradient. However, it must also be the case that there is isotopic exchange superimposed on the chemical diffusion process. In the first section of this chapter, we develop a model in which gradients in the mole fraction of each isotope drive isotopic redistribution. In the second section we offer a physical explanation for the observed difference between chemical- and self-diffusion coefficients of an element. In the third section we discuss isotope separation by diffusion in a temperature gradient.

5.1.1 Modification of Fick's first law for isotopes

In non-equilibrium thermodynamics, fluxes are linearly proportional to forces. For chemical fluxes, the forces are gradients in chemical potential, but since chemical potentials are difficult to measure, gradients in concentration are generally used as an approximation. In the simplest case, a chemical component such as Ca diffuses in response to its own concentration gradient:

$$J_i \sim \nabla C. \quad (5.1)$$

For isotopes of Ca, we can write

$$J_i \sim \nabla(f_i C), \quad (5.2)$$

where f_i is the fraction of isotope i . By expanding the right-hand side, we can see that there are actually two forces, or two potentials, that drive the flux of isotope i :

$$\underbrace{J_i}_{flow} \sim f_i \underbrace{\nabla C}_{force} + C \underbrace{\nabla f_i}_{force}. \quad (5.3)$$

The first term represents a driving force for chemical homogenization and the second term represents a driving force for isotopic homogenization. It is posited here that these terms correspond to chemical and self diffusion, respectively. Chemical diffusion refers to the chemical homogenization of a major component and it occurs when the concentration of the component of interest is sufficiently elevated so as to induce activity gradients in other chemical species (Leshner, 1994). Self diffusion, on the other hand, refers to the process of isotopic homogenization in the absence of concentration gradients; in practice, self-diffusivity is measured by setting up an experiment in which there is a gradient in the concentration of a minor isotope (Leshner, 1994).

In the formulation above, the isotopes are coupled to one another through f_i , which is distinctly different from coupling via a diffusivity matrix. To make equation 5.3 an equality, we introduce two separate proportionality constants, D_c and D_s :

$$J_i = -D_c f_i \nabla C - D_s C \nabla f_i. \quad (5.4)$$

where D_c and D_s are hereafter referred to as the chemical diffusivity and self diffusivity, respectively. The change in concentration with time is given by the divergence of the flux:

$$\frac{dC_i}{dt} = -\nabla \cdot J_i. \quad (5.5)$$

which leads to (assuming the D 's are constant):

$$\frac{dC_i}{dt} = D_c f_i \nabla^2 C + (D_c + D_s) \nabla C \nabla f_i + D_s C \nabla^2 f_i \quad (5.6)$$

It can be seen that this equation holds for two limiting cases. In the case that there is only one isotope ($f_i=1$), the resulting equation is

$$\frac{dC}{dt} = D_c \nabla^2 C, \quad (5.7)$$

which is the standard chemical diffusion equation. In the case that the elemental composition is uniform ($C=\text{constant}$) but there are gradients in the isotopic ratios, the resulting equation is

$$\frac{dC_i}{dt} = D_s C \nabla^2 f_i. \quad (5.8)$$

It makes sense that the rate of isotopic homogenization depends on the concentration of the element; the more abundant the element, the greater the number of opportunities for isotopic exchange.

5.1.2 Model results

Figure 5.1.2 shows results of equation 5.6 applied to the AB-AN and AB-DI experiments. When $D_s=D_c$ (dashed line), the results are indistinguishable from the simplified diffusion model employed in Chapter 4 (previous results are not shown for clarity). In order to obtain model isotope profiles that are more advanced than the elemental profiles, it is required that D_s be significantly greater than D_c (black lines). Results show that the difference in the length scales of elemental versus isotope ratio diffusion profiles can be explained

if D_s is greater than D_c by a factor of 2 for Ca and 6 for Mg in albitic liquid at 1450°C. This is consistent with previous observations that diffusive isotopic homogenization (self diffusion) is generally more efficient than elemental homogenization (chemical diffusion) in silicate liquids. The extent to which D_s differs from D_c seems to be inversely correlated with cation mobility, and we suspect that for fast diffusing cations, the mechanisms of chemical and self diffusion are similar and D_s/D_c approaches a value of unity.

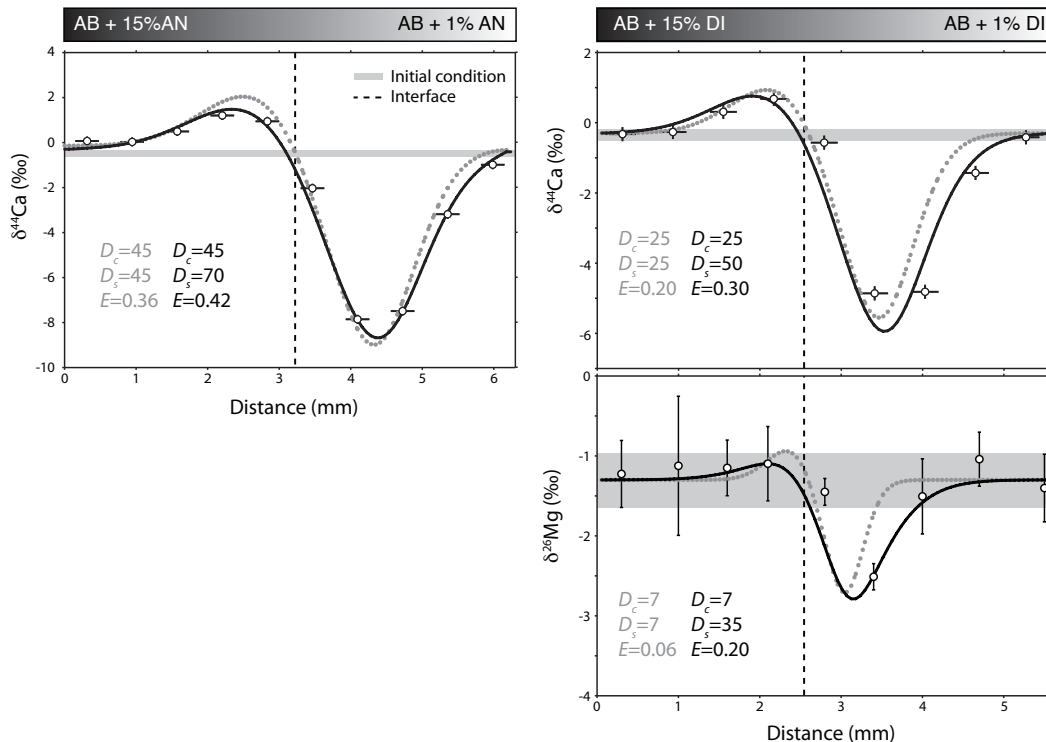


Figure 5.1: Model results using equation 5.6 applied to the AB-AN and AB-DI diffusion couples. The dashed line is for $D_s = D_c$ and results are indistinguishable from those in chapter 4. The solid line shows the result for $D_s \geq D_c$, which can explain the observation that isotope ratio profiles are more “evolved” than elemental diffusion profiles.

5.1.3 Summary and future work

During chemical diffusion, the equilibrium isotopic distribution is disturbed by the differing diffusivities of the isotopes, forming large transient variations in isotopic ratios. There must be concomitant diffusive fluxes related to isotopic exchange acting to erase these isotopic variations. The net isotope separations in our experiments must reflect both of these processes. Our experimental design combined with the model developed in this section offer a means of quantifying the self diffusion coefficient in addition to the chemical diffusion coefficient for a given cation from a single diffusion couple experiment. The question as to why the chemical and self diffusivities *should* be different is addressed in the next section.

5.2 The mechanisms of chemical versus tracer diffusion

In this section, I examine why it is that major isotopes (e.g., ^{40}Ca) should behave differently than isotopes that are present in trace quantities (e.g., ^{44}Ca). First, a few definitions (Lesher, 1994):

- **Chemical diffusion** refers to the chemical homogenization of a major component and it occurs when the concentration of the component of interest is sufficiently elevated so as to induce activity gradients in other chemical species.
- **Tracer diffusion** is measured by setting up an experiment in which there is a gradient in the concentration of a minor species.
- **Self diffusion** is very similar to tracer diffusion and refers to the process of isotopic homogenization in the absence of concentration gradients.

According to these definitions, chemical and tracer (or self) diffusion are fundamentally different processes. In most silicate liquids, ^{40}Ca is present in major quantities (chemical diffusion) whereas ^{44}Ca is present in trace quantities (self diffusion). Lesher (1994) showed that the chemical and self-diffusion coefficients of a component i can be related to one another through:

$$D_i^c = D_i^s \frac{d \ln a_i}{d \ln x_i}, \quad (5.9)$$

where D_i^c is the chemical diffusion coefficient, D_i^s is the self-diffusion coefficient, a_i is the activity, and x_i is the mol fraction. Equation 5.9 relates the chemical diffusivity to the product of species mobility and the activity-composition gradient along which diffusion occurs. In the limiting case that there are no compositional gradients, $\frac{d \ln a_i}{d \ln x_i}$ is unity and the chemical diffusion coefficient is the self-diffusion coefficient. This term is also unity for any component obeying Henry's law ($a_i = k_i x_i$), where k_i is the Henry's law constant; that is, the diffusion coefficient of a trace component such as ^{44}Ca is unaffected by compositional gradients. The main point here is to say that the chemical diffusion coefficient takes on a different form for ^{40}Ca than for ^{44}Ca as a consequence of the fact that the former is present in major quantities.

This formulation is interesting for a couple of reasons. First, it treats diffusive coupling as being thermodynamic rather than kinetic in nature. In chapter 3, we explored the possibility that diffusive coupling reflected the motion of multi-atom complexes in the liquid. In equation 5.9, however, diffusive coupling reflects changes in the activity of a diffusing component induced by changes in the local bulk composition. Second, equation 5.9 might account for why there are linear variations in $\delta^{44}\text{Ca}$ on the mafic side of the natural diffusion-couple experiments but not in the synthetic liquid experiments. In the natural liquid experiments, all of the major cations diffuse at roughly the same rate and there are significant compositional gradients that develop on the mafic side of the couple. Therefore it is this region of the couple where $\frac{d \ln a_i}{d \ln x_i}$ is probably important. In the AB-AN and AB-DI experiments, $\frac{d \ln a_i}{d \ln x_i}$ is not as important because the compositional gradients are minor. Hence the approximation that both ^{40}Ca and ^{44}Ca can be represented by a single diffusion coefficient is more valid.

To test this hypothesis, we would need information on how activity-composition gradients vary between mafic and felsic liquids. This is a significant hurdle because the solution properties of natural melts are complex. However, there is an indication from the work of Leshner and Walker (1986) and Leshner (1986; 1994; pers. comm.) that information on how $\frac{dlna_i}{dlnx_i}$ varies for ^{40}Ca between mafic and felsic liquids could be obtained from Soret experiments. The goal of a future study will be to use equation 5.9 with the parameterization of the solution properties of Sr as a function of SiO_2 content (Leshner, 1994) and implement this form of the diffusion coefficient for Sr (and by proxy Ca) isotopes into a diffusion model akin to that used in Chapter 3.

5.3 Soret isotope separation in a silicate liquid

Soret effects are another class of isotope effects that could be responsible for isotopic variations in nature. The Soret effect refers to a heat flow driving a flow of matter. This effect can be seen in experiments which show chemical separation by diffusion in an imposed temperature gradient. There are three reasons why Soret effects are interesting and potentially useful: (1) Soret separations offer one possible explanation for the linear gradients we observed in the diffusion couple experiments (Richter et al., 2008), (2) Soret separations could be responsible for considerable elemental and isotopic variability in nature (e.g., Leshner, 1986; Leshner and Walker, 1986; Kyser et al., 1998; Huang et al., 2009; Lundstrom, 2009; Huang et al., 2010) and (3) Soret separations may provide information on speciation in silicate liquids through the mass dependence on heat capacity as I describe below.

It was shown by Richter et al. (2009) that the Soret effect for isotopes in a silicate liquid can be relatively large (several ‰ per 100°C). The next immediate question is what causes this isotopic unmixing? It is a question that was not addressed by Richter et al. (2009) and in this section I make the case that isotopes separation in a temperature gradient is due to a mass dependence on heat capacity and that Soret isotope effects could be used to infer speciation. For this work I performed the Ca isotope analyses, which are shown below and have been published in *Geochimica et Cosmochimica Acta*.

5.3.1 Experiments

An experiment was conducted in which a homogeneous basalt powder was held above the liquidus in an imposed temperature gradient. Temperature was measured using the spinel growth thermometer method developed by Watson et al. (2002). Figure 5.3.1 summarizes the results. We observed that an imposed temperature gradient on a molten basalt can lead to isotope separations corresponding to $\delta^{44}\text{Ca}$ variations of about 1 per mil per 15°C . For this experiment, Fe, Si, and O isotopes were also measured (cf. Richter et al., 2009) and a general observation is that heavy isotopes are concentrated at the cold end of the capsule for all isotope pairs studied (Richter et al., 2009). This is an empirical result and in this section I provide my efforts thus far to provide a theoretical explanation for the Soret isotope effect in silicate, and perhaps other, liquid systems. The result of what follows is that the magnitude of isotope separation in a Soret experiment should reflect the

mass dependence of partial molar heat capacities of chemical components in the liquid.

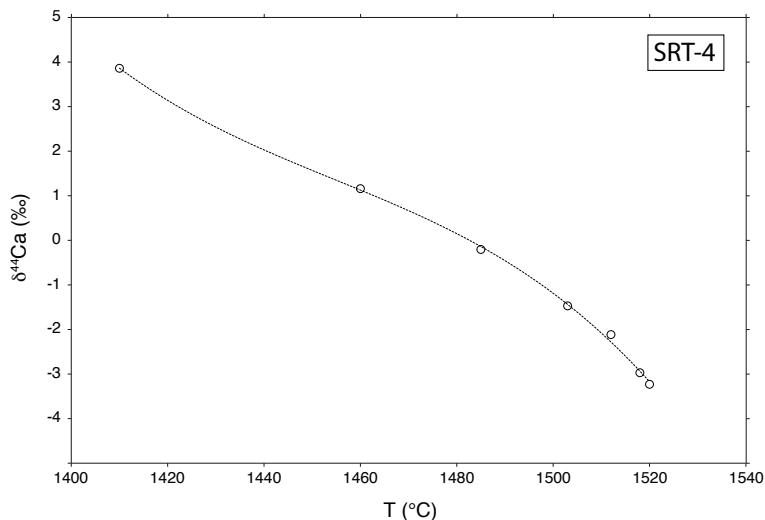


Figure 5.2: Calcium isotope separation in a temperature gradient. The bulk composition of the system is tholeiitic basalt. The isotopic composition, which was uniform prior to the experiment, varies systematically with temperature. The dashed curve is a third-order polynomial fit with no physical basis and only serves as a guide to the eye.

5.3.2 Theory

Ghiorso (1987) showed that in a Soret array at steady state, the chemical potential μ of each component k is a linear function of the temperature profile across the system. That is,

$$\mu_k = a_k + b_k T, \quad (5.10)$$

where a_k and b_k are constants. As I show below, equation 5.10 leads to the result that when a Soret experiment reaches steady state, there are no gradients in the partial molar entropy of *any* of the chemical components in the system. The derivation begins with

$$\frac{\mu_k}{T} = cst, \quad (5.11)$$

and therefore

$$\frac{\partial(\frac{\mu_k}{T})}{\partial T} = \frac{\partial\mu_k}{\partial T} \frac{1}{T} - \mu_k \frac{1}{T^2} = 0. \quad (5.12)$$

Rearranging 5.12, we arrive at

$$\frac{\partial\mu_k}{\partial T} = \frac{\mu_k}{T} = cst. \quad (5.13)$$

The next trick is to rewrite $\partial\mu_k/\partial T$ using the cross partials in the Gibbs Free Energy. That is,

$$\left(\frac{\partial\mu_k}{\partial T}\right)_{P,n} = \left(\frac{\partial}{\partial T}\left(\frac{\partial G}{\partial n_k}\right)_{T,P,n_j\neq k}\right)_{P,N} = \left(\frac{\partial}{\partial n_k}\left(\frac{\partial G}{\partial T}\right)_{P,n}\right)_{T,P,n_j\neq k} = \left(\frac{\partial S}{\partial n_k}\right)_{T,P,n_j\neq k} = \bar{s}_k \quad (5.14)$$

That is, the partial molar entropy of each component k is constant across the profile.

$$\bar{s}_k = cst \text{ for all } k. \quad (5.15)$$

From this it follows that in a Soret array at steady state there are zero entropy gradients throughout the system (though entropy is still being produced by the heat flow). A qualitative explanation for chemical (and perhaps isotopic) separation in a temperature gradient is the following: a stationary state Soret profile is characterized by a balance between one entropy gradient generated by a nonuniform temperature profile (vibrational entropy) against another generated by a composition profile (configurational+vibrational entropy). In other words, chemical unmixing occurs in order to offset the entropy gradient associated with the temperature profile. The goal of the next section is a quantitative description of this explanation.

5.3.3 What causes isotope separation in a thermal gradient?

We begin with the result from equation 5.15:

$$\nabla\bar{s}_k = 0 \text{ for all } k. \quad (5.16)$$

Let T_1 be the temperature at the hot end and T_2 be the temperature at the cold end. We have

$$\bar{s}_{k,T_1} = \bar{s}_{k,T_2}, \quad (5.17)$$

where the subscripts refer to \bar{s}_k at T_1 and T_2 respectively. The total partial molar entropy can be split into a vibrational contribution and a configurational contribution (Mysen and Richet, 2005):

$$\bar{s}_k = \bar{s}_k^{vib} + \bar{s}_k^{conf}. \quad (5.18)$$

Equation 5.17 can now be rewritten as

$$\bar{s}_{k,T_1}^{vib} + \bar{s}_{k,T_1}^{conf} = \bar{s}_{k,T_2}^{vib} + \bar{s}_{k,T_2}^{conf}. \quad (5.19)$$

Each of these terms is related to the heat capacity (which also consists of a vibrational and configurational contribution; Mysen and Richet (2005)). So we can write

$$\bar{s}_k^{0,vib} + \int_{T_0}^{T_1} \frac{c_{p,k}^{vib}(T)}{T} dT + \bar{s}_k^{0,conf} + \int_{T_0}^{T_1} \frac{c_{p,k}^{conf}(T, X)}{T} dT = \bar{s}_k^{0,vib} + \int_{T_0}^{T_2} \frac{c_{p,k}^{vib}(T)}{T} dT + \bar{s}_k^{0,conf} + \int_{T_0}^{T_2} \frac{c_{p,k}^{conf}(T, X)}{T} dT, \quad (5.20)$$

where the \bar{s}_k^0 's refer to the standard state partial molar entropies and the parentheses indicate that c_p is a function of temperature T and composition X . Equation 5.20 can be simplified to

$$\int_{T_2}^{T_1} \frac{c_{p,k}^{vib}(T)}{T} dT = \int_{T_2}^{T_1} \frac{c_{p,k}^{conf}(T, X)}{T} dT. \quad (5.21)$$

Equation 5.21 applies to a Soret array at steady state and assumes that the chemical potential μ_k is a linear function of temperature (Ghiorso, 1987). It states that the integrated vibrational contribution to the heat capacity is exactly balanced by the integrated configurational contribution to the heat capacity associated with each chemical component.

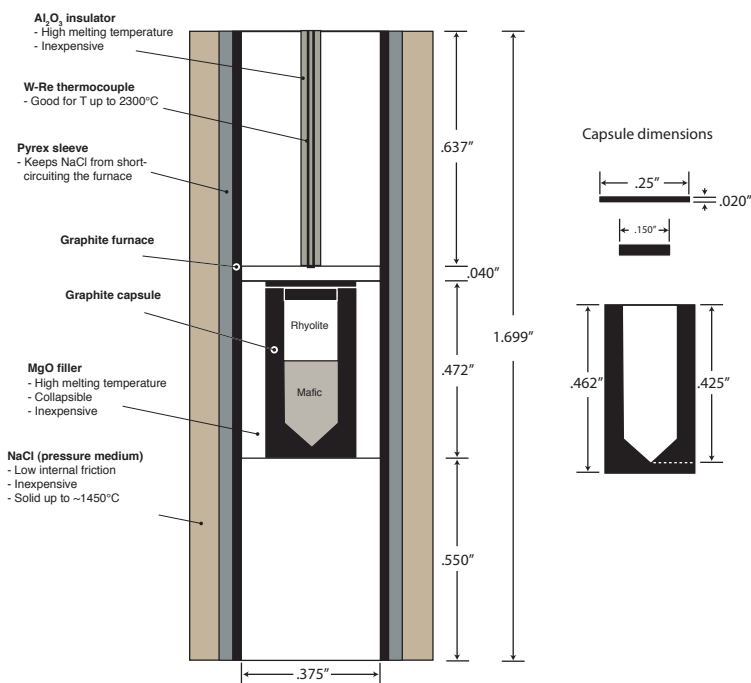
As for the isotopes, the heat capacity of a compound must change by some amount upon isotopic substitution. The magnitude of the mass dependence, however, is unknown in melts and would be difficult to predict because the identity of molecular complexes in silicate liquids is ambiguous (cf. chapter 3). Nevertheless, the relatively large isotope effects generated in Soret experiments on silicate liquids seem to suggest that the mass dependence is significant. Furthermore, these isotope effects must depend on the isotopic system (which they do; Richter et al. (2009)) as well as the nature of the isotopically-substituted species. Future experiments on simplified systems would be useful for assessing these postulates and determining whether Soret isotope separations could also be used to infer speciation in molten silicates.

Appendix A

Diffusion couple experiments

The experimental design for the silicate liquid diffusion couples was adopted from Richter et al. (2003). The starting materials are generally rock powders, which are pressed together in a graphite capsule with the mafic endmember below the felsic endmember to ensure gravitational stability. The graphite capsule is then placed in a standard piston-cylinder assembly.

A.1 Sample assembly



A.2 Piston cylinder

Once the sample assembly is in the piston-cylinder, the samples are pressurized to about 1 Gpa in order to prevent the formation of bubbles and then heated to 1450°C at a ramp rate of 150°C/min. During the ramping step, pressure is monitored and adjusted to 1.0 ± 0.1 Gpa. Samples are held at constant temperature and pressure for a specified duration and then quenched by turning off the power. The heating and cooling durations are neglected in all of our diffusion models.

A.3 Electron microprobe analysis

After an experiment, the sample is retrieved and sectioned along axis, exposing the diffusion couple. The couple is mounted in epoxy and polished for microprobe analysis.

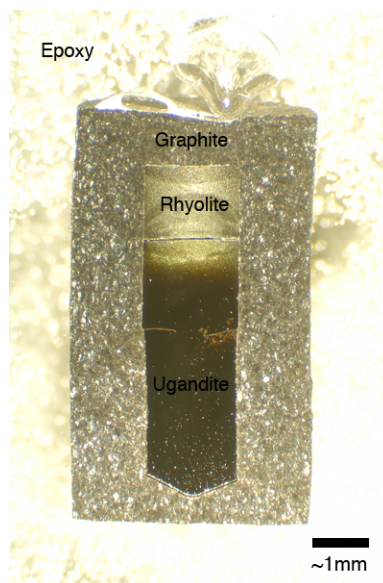


Figure A.1: Photograph of a post-run diffusion couple. The example here is from experiment DF-8.

Axis-parallel major-element profiles are measured with a Cameca SX-51 electron microprobe at UC-Berkeley. We use a 15 nA beam current rastered at 12,000X magnification ($\approx 12 \times 9 \mu\text{m}$ beam dimensions) with an accelerating voltage of 15 kV. To minimize effects of Na and K loss, these elements are measured first at each spot. On some, though not all, of the diffusion couples, multiple parallel transects were made in order to ensure that diffusion was effectively one-dimensional.

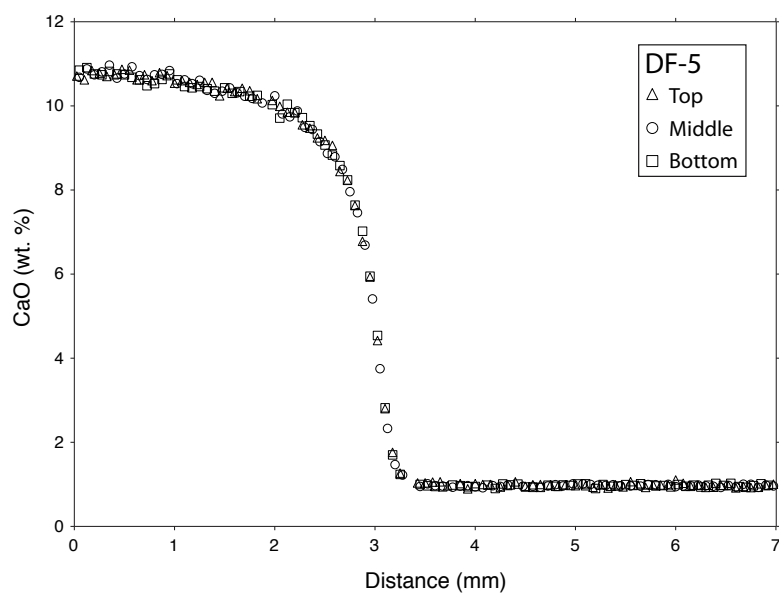


Figure A.2: Three parallel microprobe transects from DF-5 showing that chemical diffusion in our experiments can be regarded as unidimensional.

A.4 Wafering and dissolution

After microprobe analysis, diffusion couples are sectioned into wafers using a Bico diamond wafer saw with blade thickness of $165 \pm 2 \mu\text{m}$. Each wafer is $\approx 340 \pm 20 \mu\text{m}$ thick and contains enough Ca for at least two Ca isotopic analyses ($\text{Ca} \approx 10 \mu\text{g}$ total in the pure rhyolite wafers).

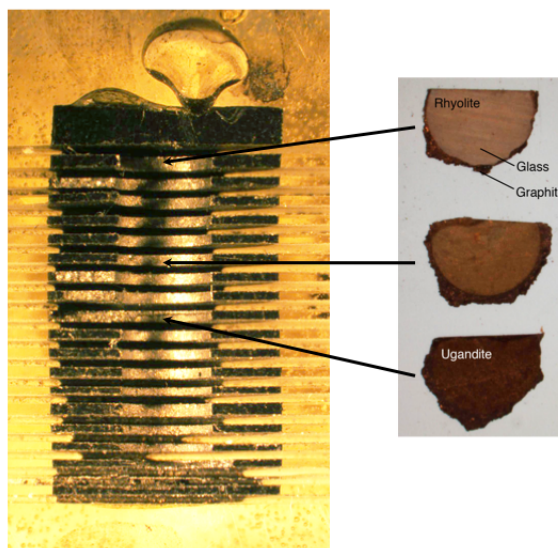


Figure A.3: Photograph of a post-run diffusion couple after sectioning. The example at left is from experiment DF-8. The wafers on the right are actually from DF-2 but are representative of typical wafers; three wafers are shown to illustrate how their physical appearance varies in going from the felsic to the mafic liquid. These three wafers still have a lot of graphite from the capsule affixed to them. Much of this graphite is removed by abrasion prior to dissolution of the silicate portion.

Samples are weighed to high precision ($\sigma \pm 0.00005 \text{ g}$), though greater uncertainty comes from the fact that weights are affected by residual graphite and/or epoxy on the samples. Sample weight uncertainties do not affect determination of isotopic ratios. Surface contamination from the saw blade and/or environment is addressed by sonicating each wafer in clean isopropyl alcohol, followed by 1.5N nitric acid, followed by two rinses of ultrapure water. Samples are dissolved in a mixture of concentrated hydrofluoric and perchloric acids in an approximate ratio of 4:1. Dissolved solutions are dried in a perchloric hood and then redissolved in 1.0N nitric acid. An appropriate amount of ^{42}Ca - and ^{48}Ca -enriched double spike is added to each sample to allow for corrections for mass discriminations produced within the mass spectrometer itself.

A.5 Cation exchange columns

The dissolved sample-spike mixtures are loaded onto cation exchange columns and eluted with 1.0N and 1.5N nitric acid in order to separate Ca from other major cations. About 3 μg of purified Ca from each sample are loaded onto a zone-refined Re filament followed by 1 μL 20% phosphoric acid.

A.6 Mass spectrometry

Ca isotope ratio measurements are carried out by thermal ionization mass spectrometry (TIMS) at UC-Berkeley on a Thermo-Finnigan Triton TI with nine moveable Faraday collectors. For each sample, 100 isotope ratio measurements are made in order to reduce within-run uncertainties to about ± 0.04 permil. For further details on within-run mass discrimination corrections, see Appendix ???. The mass-fractionation corrected ratios from the mass spectrometer are for the spike-sample mixture. The actual sample isotope ratios are determined using an iterative spike-subtraction algorithm (see Appendix ???). Sample Ca isotope ratios are reported as

$$\delta^{44}\text{Ca} = 1000 \times \left[\frac{(^{44}\text{Ca}/^{40}\text{Ca})_{\text{sample}}}{(^{44}\text{Ca}/^{40}\text{Ca})_{\text{standard}}} - 1 \right] \quad (\text{A.1})$$

where $(^{44}\text{Ca}/^{40}\text{Ca})_{\text{standard}}=0.0212076$ (Skulan et al., 1997).

Appendix B

User's guide to the Ca double spike

This section is intended as a guide to the method files of the Triton software and the spike subtraction spreadsheet that our lab group uses in order to convert data from the mass spectrometer into publishable Ca isotope ratios.

B.1 Running your sample in the mass spectrometer

Once your sample-spike mixture is loaded onto a filament and placed in the mass spectrometer, it is time to make a measurement. As you heat up the filament by passing current through it, some Ca atoms evaporate and some get ionized. The ionized fraction is sent down the flight tube toward the detectors. The detectors record counts of masses 40, 42, 43, 44, 46, and 48. During the run, the ratios of 42/48 and 40/44 ions hitting the detectors generally decreases with time because the lighter isotopes ionize more readily and therefore become increasingly depleted in the reservoir on the filament. Figure B.1 shows what some of the uncorrected data look like as a function of time.

To correct for the mass discrimination induced within the machine itself, we first choose two isotopes to be used as a normalizing ratio throughout the run. We generally use 42/48 because it represents a large mass spread. Then for each measurement within the run, the measured $(42/48)_{raw}$ is used to calculate a power law exponent α from an equation of the following form:

$$\left(\frac{42}{48}\right)_{corrected} = \left(\frac{42}{48}\right)_{raw} \left(\frac{m_{42}}{m_{48}}\right)^p, \quad (\text{B.1})$$

where m_i is the atomic mass of nuclide i . For each measurement, a value of p is calculated and applied to each of the other measured ratios. For example,

$$\left(\frac{40}{44}\right)_{corrected} = \left(\frac{40}{44}\right)_{raw} \left(\frac{m_{40}}{m_{44}}\right)^p. \quad (\text{B.2})$$

Figure B.2 is what the normalized (42/48) and corrected (40/44) data look like for a good run in which there is uniform scatter in the corrected (40/44) ratios about a mean value. Occasionally, however, you may get a "bad run" where the corrected data vary systematically with time (e.g., Figure B.3).

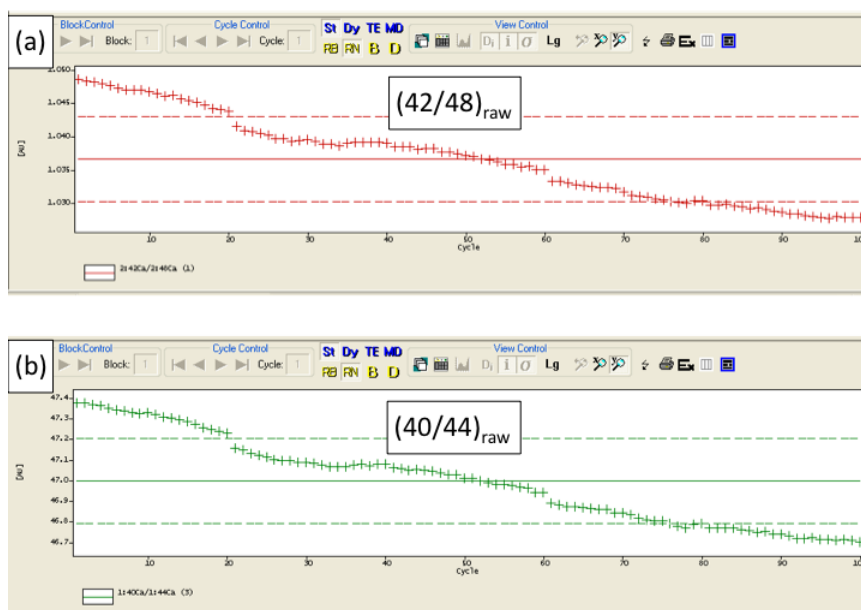


Figure B.1: Screen capture showing the raw data for two different Ca isotope ratios.

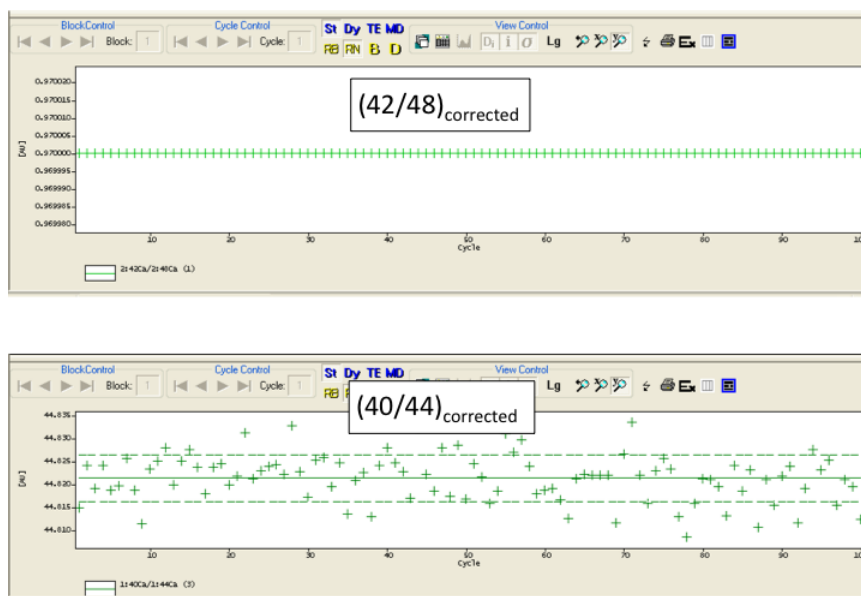


Figure B.2: Screen capture showing the corrected data for two different Ca isotope ratios. This is a "good run" in which the corrected 40/44 values show uniform scatter about a mean value.

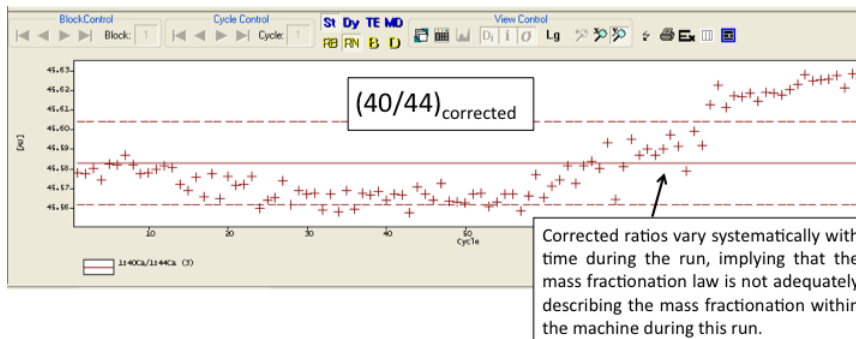


Figure B.3: Screen capture showing the corrected data for two different Ca isotope ratios. This is a "bad run" in which the corrected 40/44 values vary systematically with time.

The fact that the corrected ratio is changing with time throughout the run indicates that the power law relationship is not an adequate representation of the mass-dependence of evaporation/ionization off of the filament (for reasons that we don't understand). My suggestion is that you throw that data point out and measure a different bead from the same sample. It will probably give you a good run on the next try.

B.2 Spike subtraction

The mass-fractionation corrected ratios from the mass spectrometer are for the spike-sample mixture. The actual sample isotope ratios are determined using an iterative spike-subtraction algorithm. What follows is a summary of what the spike subtraction spreadsheet is actually doing when you input into Excel the data you collected from the mass spectrometer.

Notation used:

t =tracer (or spike)

s =sample

m =mixture (or measured)

To begin, it is assumed that the 42/48 ratio in the spike is known perfectly from the double spike calibration. Derivation of the spike subtraction algorithm then begins with:

$$\left(\frac{48}{42}\right)_m = \frac{48_s + 48_t}{42_s + 42_t} = \frac{44_s \left(\frac{48}{44}\right)_s + 48_t}{44_s \left(\frac{42}{44}\right)_s + 48_t \left(\frac{42}{48}\right)_t}. \quad (\text{B.3})$$

Rearranging equation B.3 leads to B.4, which is used to calculate a value for the $(42/48)_t$ ratio from the measured values:

$$\left(\frac{42}{48}\right)_t = \left(\frac{42}{48}\right)_m + \frac{44_s}{48_t} \left[\left(\frac{48}{44}\right)_s \left(\frac{42}{48}\right)_m - \left(\frac{42}{44}\right)_s \right]. \quad (\text{B.4})$$

Initially it is assumed that the sample has an isotopically “normal” composition. With that, the only unknown in B.4 is the $44_s/48_t$ term. An expression for this can be derived beginning with an equation similar to equation B.3:

$$\left(\frac{44}{48}\right)_m = \frac{44_s + 44_t}{48_s + 48_t} = \frac{44_s + 48_t \left(\frac{44}{48}\right)_t}{44_s \left(\frac{48}{44}\right)_s + 48_t}, \quad (\text{B.5})$$

which leads to

$$\frac{44_s}{48_t} = \frac{\left(\frac{44}{48}\right)_m - \left(\frac{44}{48}\right)_t}{1 - \left(\frac{44}{48}\right)_m \left(\frac{48}{44}\right)_s}. \quad (\text{B.6})$$

Combining B.4 and B.6, we have everything we need to calculate a first approximation for the $(42/48)_t$ ratio from the measured ratios. This value will differ from the “true” $(42/48)_t$ ratio because we used an approximation for the sample ratios (i.e., the “normal” composition). The difference is used to calculate an initial mass discrimination factor p_t in the same fashion as in equation B.1:

$$\left(\frac{42}{48}\right)_{t,\text{corrected}} = \left(\frac{42}{48}\right)_{t,\text{uncorrected}} \left(\frac{m_{42}}{m_{48}}\right)^{p_t}. \quad (\text{B.7})$$

This factor is p_t is used to correct the other measured ratios:

$$\left(\frac{40}{44}\right)_{m,\text{corrected}} = \left(\frac{40}{44}\right)_{m,\text{uncorrected}} \left(\frac{m_{40}}{m_{44}}\right)^{p_t} \quad (\text{B.8})$$

$$\left(\frac{42}{44}\right)_{m,\text{corrected}} = \left(\frac{42}{44}\right)_{m,\text{uncorrected}} \left(\frac{m_{42}}{m_{44}}\right)^{p_t} \quad (\text{B.9})$$

$$\left(\frac{48}{44}\right)_{m,\text{corrected}} = \left(\frac{48}{44}\right)_{m,\text{uncorrected}} \left(\frac{m_{48}}{m_{44}}\right)^{p_t} \quad (\text{B.10})$$

After the mass discrimination correction is applied, the desired spike-subtracted sample ratio $(40/44)_s$ is calculated from:

$$\left(\frac{40}{44}\right)_s = \left(\frac{40}{44}\right)_m + \frac{42_t}{44_s} \left[\left(\frac{44}{42}\right)_t \left(\frac{40}{44}\right)_m - \left(\frac{40}{42}\right)_t \right], \quad (\text{B.11})$$

where

$$\frac{42_t}{44_s} = \frac{\left(\frac{42}{44}\right)_m - \left(\frac{42}{44}\right)_s}{1 - \left(\frac{44}{42}\right)_t \left(\frac{42}{44}\right)_m}. \quad (\text{B.12})$$

This value for $(40/44)_s$ will differ from the “normal” value, and the difference can be used to calculate a second mass discrimination factor p_s :

$$\left(\frac{40}{44}\right)_{s,\text{corrected}} = \left(\frac{40}{44}\right)_{s,\text{uncorrected}} \left(\frac{m_{40}}{m_{44}}\right)^{p_s}, \quad (\text{B.13})$$

which is used to update the other sample ratios:

$$\left(\frac{42}{44}\right)_{s,corrected} = \left(\frac{42}{44}\right)_{s,uncorrected} \left(\frac{m_{42}}{m_{44}}\right)^{p_s} \quad (\text{B.14})$$

$$\left(\frac{48}{44}\right)_{s,corrected} = \left(\frac{48}{44}\right)_{s,uncorrected} \left(\frac{m_{48}}{m_{44}}\right)^{p_s}. \quad (\text{B.15})$$

Finally, these updated sample ratios can be used to update $(42/48)_t$ and the process is repeated until p no longer changes at the level of 1 ppm, which requires 3 to 5 iterations.

Appendix C

Additional data tables

Large spherulite			Small spherulite		
Distance (mm)	Abs	H ₂ O _{total} (wt. %)	Distance (mm)	Abs	H ₂ O _{total} (wt. %)
0.00	0.511	0.180	0.00	0.385	0.139
0.15	0.511	0.180	0.01	0.382	0.138
0.25	0.497	0.175	0.05	0.367	0.132
0.30	0.489	0.172	0.07	0.368	0.133
0.35	0.499	0.176	0.09	0.374	0.135
0.45	0.490	0.173	0.13	0.374	0.135
0.50	0.485	0.171	0.15	0.376	0.135
0.55	0.480	0.169	0.17	0.371	0.134
0.65	0.469	0.165	0.21	0.373	0.135
0.70	0.458	0.161	0.23	0.370	0.133
0.75	0.462	0.163	0.25	0.377	0.136
0.85	0.446	0.157	0.29	0.369	0.133
0.90	0.442	0.156	0.31	0.369	0.133
0.95	0.426	0.150	0.33	0.371	0.134
1.05	0.434	0.153	0.37	0.355	0.128
1.10	0.427	0.150	0.39	0.358	0.129
1.15	0.412	0.145	0.41	0.361	0.130
1.25	0.408	0.144	0.45	0.363	0.131
1.30	0.420	0.148	0.47	0.351	0.127
1.35	0.392	0.138	0.49	0.354	0.128
1.45	0.391	0.138	0.53	0.356	0.128
1.50	0.384	0.135	0.55	0.360	0.130
1.55	0.386	0.136	0.57	0.355	0.128
1.65	0.381	0.134	0.61	0.352	0.127
1.70	0.376	0.133	0.63	0.355	0.128
1.75	0.379	0.134	0.65	0.352	0.127
1.85	0.368	0.130	0.69	0.351	0.127
1.90	0.363	0.128	0.71	0.346	0.125
1.95	0.358	0.126	0.73	0.341	0.123
2.05	0.364	0.128	0.77	0.341	0.123
2.10	0.362	0.128	0.79	0.344	0.124
2.15	0.362	0.128	0.81	0.344	0.124
2.25	0.356	0.125	0.85	0.340	0.122
2.30	0.355	0.125	0.87	0.334	0.120
2.35	0.359	0.126	0.89	0.325	0.117
2.45	0.351	0.124	0.93	0.333	0.120
2.50	0.355	0.125	0.95	0.331	0.119
2.55	0.349	0.123	0.97	0.330	0.119
2.65	0.348	0.123	1.01	0.330	0.119
2.70	0.359	0.126	1.03	0.331	0.119
2.75	0.357	0.126	1.05	0.329	0.119
2.85	0.353	0.124	1.09	0.327	0.118
2.90	0.353	0.124	1.11	0.319	0.115
2.95	0.356	0.125	1.13	0.330	0.119
3.05	0.349	0.123	1.17	0.323	0.116
3.10	0.360	0.127	1.19	0.322	0.116
3.15	0.383	0.135	1.25	0.325	0.117
3.25	0.380	0.134	1.29	0.324	0.117

Table C.1: FTIR data for the two spherulitic glasses discussed in chapter 2.

DF-5

Distance (mm)	SiO ₂ (wt.%)	Al ₂ O ₃ (wt.%)	TiO ₂ (wt.%)	FeO (wt.%)	MgO (wt.%)	CaO (wt.%)	Na ₂ O (wt.%)	K ₂ O (wt.%)	MnO (wt.%)	P ₂ O ₅ (wt.%)	Total (wt.%)
0.10	47.94	12.88	2.87	12.50	10.25	10.84	2.68	0.62	0.38	-	100.96
0.23	48.10	12.89	2.93	12.28	10.17	10.76	2.63	0.61	0.30	-	100.67
0.35	48.77	13.03	2.87	12.02	10.10	10.76	2.58	0.62	0.36	-	101.11
0.48	48.87	13.08	2.86	12.18	10.03	10.77	2.53	0.64	0.29	-	101.25
0.60	47.87	12.99	2.80	12.28	9.93	10.63	2.55	0.66	0.33	-	100.03
0.73	48.81	13.17	2.84	12.29	9.91	10.66	2.51	0.65	0.30	-	101.14
0.85	47.86	13.05	2.85	11.95	10.09	10.58	2.62	0.67	0.33	-	100.00
0.98	48.17	13.08	2.92	11.83	9.68	10.46	2.46	0.68	0.34	-	99.63
1.10	49.00	13.18	2.90	12.10	9.74	10.52	2.52	0.70	0.36	-	101.01
1.23	48.21	13.23	2.91	11.87	9.66	10.51	2.55	0.75	0.37	-	100.06
1.35	48.72	13.19	2.91	11.25	9.55	10.42	2.62	0.74	0.37	-	99.77
1.48	48.27	13.27	2.88	11.52	9.49	10.54	2.63	0.77	0.30	-	99.67
1.60	49.02	13.10	2.86	11.29	9.54	10.36	2.69	0.81	0.33	-	100.00
1.73	49.44	13.01	2.81	11.38	9.27	10.43	2.81	0.87	0.30	-	100.32
1.90	50.12	13.17	2.80	10.88	9.10	10.12	2.85	0.88	0.36	-	100.27
2.10	50.71	13.34	2.62	10.93	8.87	9.91	2.85	0.96	0.31	-	100.51
2.23	51.96	13.12	2.56	10.51	8.68	9.68	2.89	1.06	0.27	-	100.74
2.35	52.65	13.36	2.49	10.19	8.35	9.59	2.91	1.12	0.33	-	101.00
2.48	53.43	13.23	2.31	9.71	7.91	9.26	3.25	1.26	0.35	-	100.71
2.60	54.90	13.34	2.12	9.19	7.38	8.83	3.30	1.45	0.27	-	100.78
2.73	56.64	13.29	1.81	8.13	6.83	8.29	3.44	1.68	0.25	-	100.36
2.88	59.66	13.06	1.50	7.14	5.72	7.02	3.79	2.12	0.23	-	100.24
3.00	65.01	12.74	1.10	5.30	4.13	5.20	4.17	2.78	0.25	-	100.68
3.13	71.15	12.36	0.58	2.87	2.10	2.74	4.14	3.50	0.19	-	99.63
3.48	72.88	13.05	0.39	1.41	0.77	1.43	4.10	4.12	0.20	-	98.36
3.63	73.20	13.00	0.40	1.58	0.71	1.43	4.02	4.10	0.20	-	98.65
3.75	72.99	13.06	0.39	1.38	0.63	1.24	4.04	4.14	0.12	-	97.99
3.93	74.02	13.16	0.38	1.26	0.51	1.14	4.11	4.22	0.17	-	98.96
4.05	74.71	13.39	0.37	1.12	0.45	1.04	4.06	4.24	0.17	-	99.56
4.18	75.32	13.33	0.39	1.14	0.38	1.00	3.97	4.31	0.14	-	99.97
4.33	74.27	13.44	0.38	1.03	0.34	1.05	4.09	4.28	0.17	-	99.05
4.45	74.43	13.45	0.37	1.13	0.31	0.98	3.96	4.35	0.22	-	99.21
4.65	73.58	13.30	0.35	1.12	0.38	0.99	3.96	4.36	0.20	-	98.23
4.78	74.10	13.51	0.38	0.88	0.30	1.02	3.96	4.36	0.11	-	98.62
4.90	74.44	13.29	0.37	1.04	0.33	1.02	3.90	4.33	0.19	-	98.92
5.03	75.42	13.28	0.36	1.06	0.29	0.92	3.94	4.36	0.15	-	99.79
5.18	74.87	13.21	0.37	1.13	0.31	0.94	3.89	4.31	0.16	-	99.19
5.30	75.28	13.48	0.38	0.96	0.33	0.98	4.02	4.31	0.12	-	99.86
5.43	75.03	13.23	0.37	1.11	0.34	0.97	4.04	4.36	0.15	-	99.60
5.55	73.12	13.46	0.39	1.04	0.32	0.90	3.89	4.36	0.18	-	97.66
5.73	73.98	13.37	0.37	0.93	0.32	0.92	4.03	4.35	0.18	-	98.44
5.85	73.27	13.39	0.37	1.00	0.31	1.00	3.91	4.37	0.17	-	97.78
5.98	73.70	13.41	0.38	1.12	0.29	0.94	3.91	4.33	0.16	-	98.24
6.10	75.07	13.59	0.37	1.10	0.31	0.93	3.88	4.33	0.13	-	99.70
6.23	74.97	13.50	0.40	1.02	0.33	1.04	3.96	4.37	0.22	-	99.80
6.35	74.01	13.53	0.38	0.96	0.33	0.93	4.00	4.36	0.24	-	98.73
6.48	74.27	13.47	0.38	1.08	0.30	0.99	3.86	4.33	0.18	-	98.85
6.60	75.52	13.35	0.37	1.08	0.31	0.94	3.87	4.29	0.21	-	99.94
6.73	75.14	13.21	0.35	1.22	0.33	0.91	4.08	4.35	0.17	-	99.75
6.85	75.52	13.25	0.37	1.08	0.32	0.99	3.96	4.31	0.20	-	100.00
6.98	75.42	13.37	0.36	1.13	0.31	0.95	3.96	4.29	0.20	-	100.00

DF-8

Distance (mm)	SiO ₂ (wt.%)	Al ₂ O ₃ (wt.%)	TiO ₂ (wt.%)	FeO (wt.%)	MgO (wt.%)	CaO (wt.%)	Na ₂ O (wt.%)	K ₂ O (wt.%)	MnO (wt.%)	P ₂ O ₅ (wt.%)	Total (wt.%)
0.14	44.84	8.87	5.15	10.76	10.85	11.22	2.67	1.86	0.20	0.59	97.01
0.30	43.53	8.87	5.14	11.52	10.74	11.26	2.72	1.88	0.22	0.56	96.44
0.46	44.73	8.57	5.07	10.84	10.70	11.20	2.71	1.90	0.22	0.40	96.34
0.64	44.74	8.79	4.95	11.27	10.65	11.11	2.81	1.89	0.21	0.42	96.84
0.82	45.58	9.06	4.94	11.21	10.61	11.02	2.88	1.95	0.11	0.51	97.87
0.98	45.00	8.90	4.96	10.82	10.51	10.99	2.73	1.98	0.09	0.40	96.39
1.16	45.45	8.88	4.91	10.41	10.40	10.88	2.83	2.01	0.28	0.47	96.52
1.34	45.38	8.95	4.93	10.70	10.32	10.94	2.81	2.00	0.08	0.50	96.61
1.50	46.69	9.02	4.83	10.83	10.41	10.80	2.89	2.05	0.11	0.48	98.12
1.67	46.09	8.92	4.70	10.99	10.41	10.94	2.92	2.06	0.15	0.42	97.60
1.83	46.99	9.12	4.67	10.52	10.16	11.06	2.94	2.15	0.22	0.40	98.23
1.99	46.82	9.11	4.53	10.13	10.05	10.51	2.96	2.09	0.24	0.40	96.84
2.17	46.88	9.09	4.45	10.04	9.98	10.72	2.98	2.19	0.08	0.43	96.85
2.35	46.91	9.23	4.37	9.93	9.96	10.39	2.91	2.23	0.31	0.42	96.66
2.51	48.07	9.30	4.33	10.22	9.83	10.45	3.01	2.30	0.13	0.47	98.11
2.69	48.23	9.41	4.21	9.80	9.77	10.48	3.02	2.34	0.22	0.39	97.87
2.85	48.19	9.24	4.11	9.77	9.64	10.21	3.07	2.36	0.23	0.28	97.10
3.01	47.94	9.33	3.98	9.50	9.42	10.12	3.13	2.49	0.15	0.39	96.45
3.17	48.24	9.68	3.87	9.24	9.34	10.04	3.17	2.58	0.16	0.30	96.62
3.33	49.39	9.50	3.73	9.57	8.92	9.48	3.30	2.62	0.27	0.39	97.17
3.49	50.46	9.77	3.58	9.13	9.00	9.68	3.18	2.72	0.26	0.39	98.16
3.65	50.61	9.93	3.40	9.24	8.76	9.61	3.25	2.85	0.15	0.29	98.08
3.81	51.53	9.89	3.27	8.80	8.48	9.22	3.40	3.01	0.23	0.27	98.10
3.97	51.55	9.82	3.09	8.59	8.25	9.02	3.44	3.07	0.23	0.24	97.30
4.13	52.88	9.86	2.93	8.51	7.93	8.78	3.47	3.20	0.21	0.30	98.07
4.31	54.47	10.15	2.69	7.75	7.50	8.32	3.43	3.51	0.13	0.23	98.18
4.47	54.85	10.33	2.47	7.57	7.17	8.00	3.61	3.67	0.12	0.19	97.98
4.63	55.86	10.56	2.26	7.08	6.93	7.30	3.82	3.90	0.20	0.14	98.05
4.79	57.06	10.87	2.04	6.56	6.41	7.29	3.76	4.06	0.15	0.16	98.35
4.95	59.16	10.85	1.80	6.19	5.90	6.63	3.73	4.39	0.07	0.12	98.84
5.11	60.26	10.98	1.56	5.71	5.39	6.02	3.92	4.69	0.13	0.08	98.73
5.27	61.97	11.28	1.27	5.40	4.64	5.21	3.95	5.03	0.00	0.05	98.80
5.43	64.66	11.44	0.91	4.23	3.80	4.29	3.89	5.56	0.09	0.02	98.88
5.59	67.29	11.67	0.60	3.50	2.97	3.31	3.88	5.96	0.04	0.00	99.23
5.75	70.52	11.88	0.34	2.51	2.04	2.36	3.70	6.30	0.00	0.00	99.66
5.91	71.99	12.33	0.09	1.71	1.08	1.51	3.51	6.49	0.01	0.03	98.75
6.07	74.41	12.74	0.09	0.91	0.50	1.05	3.31	6.71	0.02	0.02	99.76
6.24	74.01	12.44	0.12	0.72	0.23	0.88	3.30	6.88	0.07	0.02	98.66
6.40	74.80	12.78	0.08	0.56	0.12	0.76	3.26	6.75	0.06	0.01	99.17
6.56	74.67	12.86	0.12	0.66	0.10	0.74	3.26	6.78	0.00	0.03	99.21
6.80	76.67	12.25	0.09	0.58	0.10	0.67	3.32	6.70	0.03	0.01	100.41
6.96	75.45	13.14	0.11	0.67	0.09	0.75	3.13	6.70	0.03	0.03	100.10
7.12	75.39	12.89	0.10	0.74	0.10	0.69	2.89	6.58	0.03	0.00	99.41
7.28	75.26	13.02	0.09	0.75	0.11	0.63	2.90	6.55	0.00	0.00	99.32
7.44	76.07	12.62	0.10	0.80	0.11	0.70	2.95	6.44	0.05	0.01	99.85
7.60	75.60	12.92	0.09	0.88	0.11	0.68	2.82	6.39	0.07	0.10	99.66
7.76	75.96	12.90	0.08	0.76	0.09	0.73	2.83	6.36	0.13	0.01	99.84
7.92	76.77	12.98	0.10	0.90	0.12	0.76	2.83	6.26	0.08	0.05	100.84
8.08	75.47	13.31	0.11	0.68	0.12	0.71	2.80	6.18	0.07	0.04	99.49
8.24	74.91	13.22	0.09	0.79	0.13	0.72	2.73	6.22	0.00	0.02	98.83
8.40	75.49	13.26	0.12	0.64	0.09	0.82	2.80	6.20	0.08	0.03	99.54

DF-9

Distance (mm)	SiO ₂ (wt.%)	Al ₂ O ₃ (wt.%)	TiO ₂ (wt.%)	FeO (wt.%)	MgO (wt.%)	CaO (wt.%)	Na ₂ O (wt.%)	K ₂ O (wt.%)	MnO (wt.%)	P ₂ O ₅ (wt.%)	Total (wt.%)
0.11	49.01	12.59	2.67	11.11	9.33	10.73	2.13	0.59	0.21	0.20	98.56
0.26	48.91	12.62	2.75	11.01	9.37	10.70	2.11	0.61	0.19	0.24	98.49
0.41	49.41	12.59	2.73	11.00	9.34	10.78	2.24	0.62	0.19	0.22	99.12
0.58	49.41	12.71	2.72	11.00	9.17	10.58	2.18	0.63	0.22	0.31	98.92
0.73	49.27	12.64	2.67	11.00	9.03	10.67	2.09	0.65	0.21	0.22	98.46
0.89	49.38	12.71	2.74	10.91	9.11	10.52	2.21	0.64	0.20	0.28	98.70
1.04	49.60	12.73	2.69	10.27	8.91	10.50	2.16	0.66	0.13	0.22	97.88
1.19	49.91	12.74	2.73	10.72	8.88	10.62	2.17	0.69	0.15	0.23	98.84
1.35	50.43	12.67	2.64	10.54	8.85	10.36	2.33	0.70	0.15	0.24	98.91
1.50	50.78	12.79	2.57	10.43	8.75	10.34	2.33	0.74	0.14	0.27	99.14
1.65	51.14	12.70	2.58	10.39	8.69	10.31	2.36	0.77	0.25	0.24	99.44
1.81	51.39	12.72	2.53	10.38	8.62	10.30	2.47	0.80	0.20	0.27	99.68
1.96	51.65	12.58	2.53	10.02	8.45	10.22	2.43	0.86	0.14	0.26	99.14
2.11	52.02	12.70	2.52	9.83	8.29	9.98	2.47	0.87	0.17	0.20	99.05
2.26	52.37	12.76	2.29	9.83	8.13	9.80	2.58	0.93	0.18	0.19	99.05
2.42	53.00	12.72	2.20	9.60	8.02	9.68	2.48	0.99	0.19	0.21	99.07
2.57	53.90	12.64	2.15	9.32	7.73	9.45	2.61	1.08	0.13	0.20	99.21
2.72	54.59	12.79	1.98	8.94	7.45	9.11	2.84	1.18	0.15	0.15	99.17
2.88	55.56	12.71	1.83	8.68	7.16	8.92	2.85	1.25	0.15	0.25	99.34
3.03	56.82	12.65	1.70	7.95	6.66	8.48	3.05	1.48	0.14	0.18	99.11
3.18	59.16	12.14	1.49	7.11	6.20	7.75	3.01	1.68	0.19	0.14	98.87
3.46	63.91	12.25	1.00	5.69	4.48	6.03	3.65	2.35	0.10	0.08	99.55
3.61	70.13	11.96	0.49	3.66	2.80	4.01	3.76	3.04	0.02	0.05	99.93
3.81	75.06	12.67	0.09	1.32	0.83	1.75	3.97	3.92	0.07	0.06	99.74
3.98	76.59	13.01	0.09	0.84	0.23	1.17	4.11	4.13	0.01	0.01	100.20
4.13	76.98	13.14	0.12	0.79	0.15	1.04	4.16	4.29	0.04	0.00	100.71
4.30	76.28	13.08	0.11	0.77	0.10	0.92	4.05	4.16	0.04	0.04	99.55
4.47	77.26	13.20	0.13	0.83	0.11	0.90	4.10	4.24	0.07	0.03	100.86
4.62	76.94	13.19	0.12	0.87	0.10	0.88	3.96	4.16	0.08	0.03	100.32
4.79	76.92	13.20	0.09	0.81	0.10	0.87	4.04	4.23	0.02	0.00	100.28
4.96	77.35	13.18	0.10	0.92	0.10	0.88	4.08	4.30	0.07	0.03	101.02
5.11	77.33	13.21	0.10	0.82	0.10	0.85	3.91	4.16	0.05	0.03	100.55
5.26	77.39	13.06	0.11	0.82	0.11	0.88	4.15	4.19	0.03	0.04	100.78
5.42	77.54	13.11	0.09	0.89	0.10	0.92	4.16	4.21	0.02	0.01	101.05
5.57	77.55	13.12	0.11	0.85	0.12	0.90	3.98	4.29	0.06	0.05	101.02
5.72	77.29	13.07	0.11	0.82	0.10	0.89	4.12	4.17	0.02	0.06	100.65
5.88	77.64	13.08	0.11	0.82	0.11	0.87	3.88	4.24	0.02	0.02	100.79
6.03	77.58	13.11	0.12	0.89	0.12	0.85	4.01	4.28	0.02	0.04	101.02
6.18	77.39	13.17	0.09	0.96	0.10	0.93	3.96	4.25	0.10	0.02	100.97
6.33	77.40	13.09	0.09	0.90	0.11	0.90	3.98	4.16	0.04	0.00	100.68
6.49	77.30	13.07	0.12	0.88	0.10	0.89	3.78	4.20	0.04	0.00	100.39
6.64	76.92	13.03	0.10	0.80	0.12	0.88	3.83	4.17	0.09	0.06	99.99
6.79	77.19	13.12	0.09	0.80	0.11	0.83	3.91	4.22	0.06	0.01	100.34
6.95	76.73	13.14	0.11	0.86	0.10	0.85	3.88	4.22	0.00	0.04	99.94
7.10	76.44	13.07	0.12	0.87	0.11	0.84	3.81	4.28	0.03	0.04	99.61
7.25	77.44	12.93	0.13	0.82	0.12	0.89	3.69	4.24	0.01	0.00	100.26

DF-11

Distance (mm)	SiO ₂ (wt.%)	Al ₂ O ₃ (wt.%)	TiO ₂ (wt.%)	FeO (wt.%)	MgO (wt.%)	CaO (wt.%)	Na ₂ O (wt.%)	K ₂ O (wt.%)	MnO (wt.%)	P ₂ O ₅ (wt.%)	Total (wt.%)
0.13	43.47	8.38	4.97	10.42	10.07	11.05	2.69	2.05	-	-	93.10
0.28	43.55	8.53	4.94	10.54	9.97	10.92	2.78	2.06	-	-	93.29
0.42	43.92	8.46	4.90	10.39	9.74	10.88	2.77	2.07	-	-	93.12
0.57	43.99	8.52	4.88	10.57	9.65	10.99	2.68	2.03	-	-	93.30
0.71	44.25	8.47	4.78	10.47	9.84	10.89	2.73	2.14	-	-	93.57
0.86	44.08	8.63	4.78	10.57	9.66	10.81	2.74	2.15	-	-	93.41
1.00	44.24	8.61	4.77	10.12	9.62	10.73	2.82	2.12	-	-	93.02
1.15	44.32	8.55	4.69	10.20	9.54	10.83	2.74	2.23	-	-	93.10
1.29	44.49	8.67	4.58	10.29	9.52	10.58	2.76	2.20	-	-	93.09
1.44	44.45	8.61	4.59	10.15	9.32	10.62	2.77	2.27	-	-	92.77
1.58	45.16	8.65	4.37	9.78	9.25	10.59	2.79	2.26	-	-	92.85
1.73	45.17	8.67	4.43	9.78	9.26	10.32	2.92	2.31	-	-	92.85
1.87	45.49	8.78	4.33	9.75	9.02	10.39	2.92	2.37	-	-	93.05
2.02	45.82	8.86	4.10	9.44	9.08	10.24	2.88	2.46	-	-	92.88
2.16	46.10	8.90	4.05	9.55	8.97	10.07	2.89	2.45	-	-	92.98
2.31	46.91	9.01	3.89	9.12	8.83	9.79	3.04	2.63	-	-	93.22
2.45	47.21	9.11	3.79	9.00	8.37	9.49	3.51	2.54	-	-	93.02
2.65	47.95	9.16	3.59	8.97	8.32	9.47	3.13	2.78	-	-	93.38
2.80	48.38	9.27	3.42	8.60	8.19	9.30	3.26	2.92	-	-	93.34
2.94	49.39	9.40	3.24	8.40	7.85	9.15	3.32	3.04	-	-	93.79
3.09	50.55	9.55	2.92	8.28	7.61	8.72	3.38	3.25	-	-	94.27
3.23	51.78	9.72	2.79	7.91	7.22	8.23	3.58	3.39	-	-	94.63
3.42	53.03	10.00	2.48	7.49	6.80	7.73	3.64	3.71	-	-	94.87
3.57	54.15	10.24	2.12	6.81	6.27	7.36	3.66	3.98	-	-	94.59
3.71	55.60	10.38	1.87	6.51	5.89	6.52	3.80	4.29	-	-	94.87
3.86	56.89	10.56	1.55	5.39	5.15	6.03	3.84	4.63	-	-	94.04
4.00	58.97	10.67	1.22	4.93	4.38	5.13	3.95	5.08	-	-	94.33
4.15	60.95	10.94	0.87	4.11	3.56	4.02	3.91	5.48	-	-	93.84
4.29	63.46	11.00	0.52	3.10	2.62	3.03	3.92	5.86	-	-	93.51
4.44	66.57	11.46	0.23	2.09	1.60	2.03	3.72	6.23	-	-	93.92
4.58	69.30	11.86	0.10	1.34	0.79	1.31	3.52	6.51	-	-	94.74
4.73	70.56	12.31	0.11	0.89	0.33	0.92	3.52	6.58	-	-	95.21
4.87	72.18	12.47	0.10	0.71	0.15	0.79	3.44	6.59	-	-	96.43
5.02	72.43	12.58	0.10	0.77	0.09	0.70	3.41	6.63	-	-	96.71
5.16	73.03	12.51	0.12	0.82	0.09	0.68	3.34	6.47	-	-	97.05
5.31	73.57	12.66	0.13	0.82	0.09	0.68	3.25	6.45	-	-	97.64
5.45	73.43	12.70	0.10	0.85	0.08	0.68	3.25	6.30	-	-	97.39
5.60	73.84	12.70	0.09	0.76	0.11	0.68	3.21	6.17	-	-	97.55
5.74	74.15	12.78	0.08	0.77	0.10	0.67	3.10	5.94	-	-	97.60
5.89	74.74	12.81	0.11	0.79	0.10	0.71	3.10	5.89	-	-	98.24
6.03	74.70	12.86	0.09	0.77	0.10	0.76	3.03	5.72	-	-	98.02
6.18	75.14	13.01	0.13	0.73	0.10	0.77	2.94	5.74	-	-	98.58
6.32	75.81	12.96	0.09	0.89	0.08	0.79	3.00	5.65	-	-	99.27
6.47	75.97	12.96	0.12	0.73	0.11	0.88	2.83	5.48	-	-	99.07
6.61	75.90	13.00	0.10	0.88	0.12	0.89	2.97	5.52	-	-	99.38
6.76	75.51	12.87	0.11	0.88	0.12	0.89	2.97	5.49	-	-	98.83
6.90	75.49	12.88	0.09	0.88	0.10	0.84	2.95	5.40	-	-	98.64
7.05	76.34	12.90	0.12	0.78	0.10	0.85	2.92	5.42	-	-	99.42
7.12	76.32	12.74	0.09	0.72	0.11	0.87	2.80	5.49	-	-	99.15

DF-12

Distance (mm)	SiO ₂ (wt.%)	Al ₂ O ₃ (wt.%)	TiO ₂ (wt.%)	FeO (wt.%)	MgO (wt.%)	CaO (wt.%)	Na ₂ O (wt.%)	K ₂ O (wt.%)	MnO (wt.%)	P ₂ O ₅ (wt.%)	Total (wt.%)
0.16	50.03	12.75	2.48	11.05	9.51	11.03	2.17	0.47	-	0.21	99.71
0.26	48.87	12.84	2.48	10.82	9.47	11.05	2.20	0.46	-	0.27	98.47
0.46	48.83	12.66	2.54	11.05	9.54	10.95	2.05	0.48	-	0.29	98.40
0.56	48.99	12.91	2.51	11.00	9.44	11.13	2.19	0.46	-	0.27	98.91
0.76	49.39	12.82	2.43	11.04	9.44	10.96	2.21	0.47	-	0.23	98.98
0.86	49.02	12.91	2.52	11.23	9.54	11.06	2.22	0.49	-	0.28	99.28
1.06	48.69	12.96	2.34	11.02	9.60	10.93	2.22	0.44	-	0.24	98.43
1.16	48.64	12.78	2.50	10.69	9.48	10.98	2.25	0.47	-	0.26	98.06
1.35	50.33	12.80	2.54	10.90	9.39	11.02	2.22	0.50	-	0.30	100.01
1.45	49.16	12.89	2.32	11.09	9.58	10.95	2.19	0.47	-	0.29	98.93
1.65	49.34	12.87	2.62	10.92	9.49	10.89	2.19	0.53	-	0.30	99.15
1.75	49.39	12.88	2.59	10.87	9.46	11.09	2.22	0.50	-	0.22	99.22
1.95	49.02	12.96	2.62	10.91	9.46	10.90	2.18	0.51	-	0.26	98.81
2.05	49.22	13.00	2.35	10.94	9.38	11.00	2.24	0.49	-	0.29	98.92
2.25	49.92	13.06	2.49	10.95	9.48	11.03	2.19	0.47	-	0.25	99.84
2.34	49.19	12.96	2.32	11.05	9.40	10.98	2.25	0.48	-	0.24	98.86
2.54	49.22	13.00	2.39	11.01	9.51	11.02	2.17	0.48	-	0.29	99.09
2.64	49.03	12.96	2.50	10.71	9.50	10.93	2.18	0.50	-	0.25	98.56
2.84	49.78	12.98	2.39	10.95	9.48	10.93	2.25	0.50	-	0.30	99.56
2.94	49.43	12.92	2.48	10.91	9.38	10.87	2.57	0.50	-	0.24	99.30
3.14	49.70	13.01	2.49	10.92	9.43	10.97	2.21	0.47	-	0.26	99.44
3.24	49.61	13.01	2.33	11.00	9.47	10.82	2.30	0.50	-	0.31	99.35
3.43	49.81	13.03	2.45	11.08	9.38	10.73	2.26	0.48	-	0.26	99.48
3.53	49.72	13.03	2.50	11.02	9.39	10.93	2.21	0.48	-	0.24	99.53
3.73	49.34	12.92	2.40	10.82	9.34	10.83	2.27	0.48	-	0.27	98.67
3.83	49.55	12.95	2.37	10.77	9.39	10.90	2.18	0.48	-	0.25	98.84
4.03	49.79	12.94	2.49	10.82	9.35	10.89	2.24	0.46	-	0.23	99.21
4.13	49.57	12.92	2.36	10.85	9.53	10.96	2.38	0.52	-	0.28	99.38
4.33	50.07	12.85	2.30	11.05	9.47	11.02	2.24	0.48	-	0.22	99.70
4.42	49.34	13.00	2.50	10.71	9.48	10.98	2.19	0.48	-	0.21	98.91
4.62	49.16	12.95	2.47	11.15	9.48	10.83	2.15	0.48	-	0.25	98.91
4.72	49.63	13.02	2.59	10.88	9.37	10.94	2.29	0.51	-	0.24	99.48
4.92	49.82	13.00	2.50	10.78	9.49	11.11	2.22	0.49	-	0.23	99.64
5.02	49.17	12.98	2.42	11.07	9.34	11.11	2.25	0.48	-	0.23	99.04
5.22	49.20	12.97	2.44	10.89	9.43	10.92	2.23	0.48	-	0.22	98.78
5.32	49.41	12.87	2.54	10.99	9.42	11.12	2.22	0.48	-	0.26	99.30
5.51	50.02	12.89	2.38	10.74	9.39	11.11	2.27	0.49	-	0.27	99.57
5.61	49.70	12.86	2.49	10.75	9.42	11.03	2.18	0.52	-	0.24	99.20
5.81	49.55	12.96	2.38	10.97	9.54	11.08	2.32	0.48	-	0.24	99.52
5.91	49.52	12.93	2.37	10.74	9.48	11.08	2.19	0.49	-	0.21	98.99
6.11	49.42	12.94	2.53	10.64	9.51	11.08	2.25	0.51	-	0.23	99.11
6.21	49.54	12.81	2.42	10.84	9.45	10.90	2.27	0.53	-	0.24	99.01
6.41	49.36	12.91	2.43	10.81	9.53	11.02	2.24	0.52	-	0.29	99.12
6.51	49.69	13.09	2.51	10.83	9.52	10.83	2.20	0.49	-	0.27	99.43
6.70	49.43	12.95	2.42	10.84	9.47	11.14	2.31	0.47	-	0.24	99.27
6.80	49.49	13.00	2.77	10.61	9.55	10.87	2.27	0.48	-	0.24	99.29
7.00	49.78	13.01	2.42	10.80	9.65	11.07	2.24	0.49	-	0.27	99.72
7.10	49.76	13.17	2.58	10.77	9.60	11.09	2.18	0.49	-	0.21	99.85

ABAN-2

Distance (mm)	SiO ₂ (wt.%)	Al ₂ O ₃ (wt.%)	CaO (wt.%)	Na ₂ O (wt.%)	FeO (wt.%)	Total (wt.%)
0.06	63.65	22.07	3.08	9.81	0.14	98.75
0.18	64.22	22.06	3.09	9.90	0.20	99.47
0.30	64.28	22.10	3.08	9.86	0.17	99.48
0.42	63.68	22.29	3.15	9.88	0.21	99.20
0.54	63.39	21.87	3.07	9.76	0.17	98.26
0.66	63.90	22.03	3.09	9.96	0.24	99.22
0.78	63.73	22.11	3.03	9.85	0.23	98.94
0.90	63.97	22.37	3.00	9.79	0.21	99.35
1.02	63.51	21.62	3.02	9.52	0.30	97.97
1.14	63.24	22.00	2.95	9.69	0.19	98.07
1.26	64.13	22.25	3.04	9.74	0.21	99.37
1.38	63.79	22.11	3.05	9.82	0.22	98.98
1.50	63.77	22.27	3.01	9.94	0.22	99.21
1.62	63.74	22.13	2.96	9.81	0.24	98.88
1.74	63.84	22.08	2.86	9.87	0.20	98.85
1.86	64.01	22.08	2.91	9.86	0.19	99.06
1.98	63.54	22.29	2.78	9.79	0.20	98.60
2.10	64.00	22.35	2.76	10.10	0.20	99.41
2.22	63.87	22.18	2.71	10.27	0.21	99.24
2.34	63.74	22.27	2.70	10.18	0.18	99.07
2.46	63.94	22.25	2.52	10.19	0.18	99.07
2.64	64.49	22.18	2.52	10.24	0.22	99.74
2.76	64.39	22.13	2.44	10.30	0.18	99.44
2.88	64.55	21.96	2.38	10.33	0.19	99.40
3.00	64.32	22.03	2.15	10.45	0.20	99.15
3.12	65.52	21.40	1.91	10.41	0.14	99.39
3.24	66.87	20.21	1.61	10.13	0.16	98.98
3.36	68.02	19.63	1.40	10.13	0.16	99.33
3.48	68.20	19.41	1.24	10.24	0.07	99.16
3.60	68.24	19.66	1.12	10.28	0.13	99.42
3.72	67.75	19.54	0.98	10.28	0.13	98.69
3.84	67.88	19.47	0.88	10.36	0.13	98.72
3.96	68.28	19.63	0.74	10.40	0.10	99.16
4.08	68.37	19.67	0.71	10.56	0.16	99.47
4.20	68.14	19.61	0.58	10.57	0.11	99.01
4.32	68.42	19.66	0.49	10.59	0.17	99.33
4.44	67.95	19.55	0.46	10.68	0.18	98.82
4.56	68.05	19.62	0.44	10.71	0.16	98.98
4.68	67.89	19.64	0.42	10.61	0.10	98.65
4.80	68.38	19.64	0.37	10.71	0.08	99.18
4.92	68.46	19.80	0.36	10.67	0.08	99.35
5.04	68.39	19.69	0.36	10.69	0.09	99.22
5.16	67.89	19.75	0.35	10.83	0.12	98.95
5.28	68.23	19.63	0.33	10.78	0.14	99.10
5.40	68.05	19.79	0.32	10.84	0.14	99.15
5.52	68.10	19.87	0.35	10.79	0.11	99.21
5.64	68.07	19.90	0.31	10.52	0.08	98.88
5.76	67.96	19.83	0.32	10.71	0.14	98.95
5.88	68.22	19.80	0.31	10.47	0.17	98.97
6.00	68.17	19.93	0.34	10.43	0.14	99.00
6.18	68.02	19.79	0.29	10.81	0.14	99.05
6.30	68.32	19.65	0.33	10.74	0.11	99.16

ABDI-4						
Distance (mm)	SiO ₂ (wt.%)	Al ₂ O ₃ (wt.%)	CaO (wt.%)	Na ₂ O (wt.%)	MgO (wt.%)	Total (wt.%)
0.00	66.10	16.92	3.91	9.54	2.70	96.47
0.06	66.10	16.96	3.78	9.67	2.60	96.52
0.18	65.80	17.04	3.81	9.73	2.60	96.38
0.30	66.10	17.15	3.75	9.69	2.60	96.69
0.42	66.30	16.95	3.80	9.58	2.60	96.63
0.54	66.40	16.72	3.74	9.69	2.60	96.56
0.66	65.30	16.65	3.70	9.63	2.60	95.28
0.78	66.20	16.68	3.82	9.76	2.60	96.46
0.90	66.20	16.97	3.70	9.72	2.60	96.58
1.02	65.90	16.84	3.68	9.67	2.70	96.09
1.14	65.90	16.93	3.71	9.73	2.70	96.27
1.26	65.80	16.96	3.71	9.68	2.60	96.15
1.38	66.00	16.82	3.72	9.70	2.60	96.24
1.50	66.30	16.82	3.54	9.67	2.60	96.33
1.62	65.80	16.71	3.58	9.64	2.60	95.73
1.74	65.50	16.58	3.47	9.80	2.60	95.35
1.86	65.90	16.61	3.46	9.86	2.50	95.84
1.98	66.10	16.90	3.36	9.75	2.60	96.12
2.10	66.10	16.97	3.18	9.77	2.50	96.03
2.22	66.10	16.97	3.09	9.86	2.40	96.02
2.34	66.80	17.17	2.72	9.95	2.20	96.64
2.46	67.00	17.34	2.53	9.98	1.90	96.85
2.58	67.40	17.65	2.20	10.20	1.50	97.45
2.70	67.20	18.43	1.87	10.38	1.20	97.88
2.82	66.90	18.83	1.57	10.66	0.90	97.95
2.94	67.40	19.22	1.33	10.81	0.60	98.75
3.06	67.60	19.29	1.14	10.71	0.50	98.74
3.18	67.70	19.33	0.92	10.76	0.30	98.70
3.30	67.50	19.41	0.80	10.66	0.30	98.38
3.42	67.70	19.46	0.68	10.89	0.30	98.74
3.54	67.40	19.49	0.61	10.87	0.20	98.37
3.66	67.60	19.48	0.55	10.93	0.30	98.57
3.78	67.90	19.31	0.51	10.91	0.30	98.63
3.90	68.00	19.26	0.47	10.99	0.30	98.71
4.02	67.30	19.11	0.44	10.86	0.20	97.71
4.14	67.70	19.30	0.41	10.97	0.20	98.37
4.26	67.80	19.35	0.40	10.96	0.30	98.52
4.38	67.40	19.35	0.40	10.77	0.30	97.92
4.50	67.50	19.40	0.41	11.01	0.30	98.31
4.62	66.90	19.21	0.43	10.99	0.30	97.53
4.74	67.20	19.10	0.40	10.87	0.30	97.57
4.86	67.50	19.00	0.38	11.02	0.30	97.89
4.98	67.70	19.10	0.39	10.89	0.30	98.08
5.10	67.70	19.31	0.37	10.84	0.30	98.22
5.22	67.90	19.34	0.38	10.90	0.30	98.52
5.34	68.00	19.32	0.37	10.96	0.20	98.65
5.46	67.70	19.23	0.39	10.87	0.30	98.19
5.58	67.90	19.14	0.39	10.96	0.30	98.39

Bibliography

- Baker, D., 1989. Tracer versus trace element diffusion: Diffusional decoupling of sr concentration from sr isotope composition. *Geochimica et Cosmochimica Acta* 53, 3015–3023.
- Birch, A., LeComte, P., 1960. Temperature-pressure plane for albite composition. *American Journal of Science* 258, 209–217.
- Bottinga, W., Weill, D., 1972. The viscosity of magmatic silicate liquids: A model for calculation. *American Journal of Science* 272, 438–475.
- Bourg, I., Sposito, G., 2007. Molecular dynamics simulations of kinetic isotope fractionation during the diffusion of ionic species in liquid water. *Geochimica et Cosmochimica Acta* 71 (23), 5583–5589.
- Bourg, I., Sposito, G., 2008. Isotopic fractionation of noble gases by diffusion in liquid water: Molecular dynamics simulations and hydrologic applications. *Geochimica et Cosmochimica Acta* 72, 2237–2247.
- Calas, G., Henderson, G., Stebbins, J., 2006. Glasses and melts: Linking geochemistry and materials science. *Elements* 2, 265–268.
- Carmichael, I., Turner, F., Verhoogen, J., 1974. *Igneous Petrology*. McGraw-Hill, New York, 739 pages.
- Castro, J., Beck, P., Tuffen, H., Nichols, A., Dingwell, D., Martin, M., November-December 2008. Timescales of spherulite crystallization in obsidian inferred from water concentration profiles. *American Mineralogist* 93 (11-12), 1816–1822.
- Castro, J., Manga, M., Martin, M., 2005. Vesiculation rates of obsidian domes inferred from H₂O concentration profiles. *Geophysical Research Letters* 32 (L21307).
- Chakraborty, S., Dingwell, D., Rubie, D., 1995. Multicomponent diffusion in ternary silicate melts in the system K₂O-Al₂O₃-SiO₂: II, mechanisms, systematics, and geological applications. *Geochimica et Cosmochimica Acta* 59 (2), 265–277.
- Chopard, B., Droz, M., 1998. *Cellular Automata and Modeling of Physical Systems*, Monographs and Texts in Statistical Physics. Cambridge University Press, 353 pages.
- Cooper, A., 1965. Model for multi-component diffusion. *Phys. Chem. Glasses* 6, 55–61.

- Cross, W., 1891. Constitution and origin of spherulites in acid eruptive rocks. *Philosophical Society of Washington Bulletin* 11, 411–449.
- Cullinan, H., 1965. Analysis of flux equations of multicomponent diffusion. *Industrial and Engineering Fundamentals* 4 (2), 133–139.
- Davis, B., McPhie, J., 1996. Spherulites, quench fractures and relict perlite in a late devonian rhyolite dyke, queensland, australia. *Journal of Volcanology and Geothermal Research* 71, 1–11.
- der Laan, S. V., Zhang, X., Kennedy, A., Wyllie, P., 1994. Comparison of element and isotope diffusion of K and Ca in multicomponent silicate melts. *Earth and Planetary Science Letters* 123, 155–166.
- Dingwell, D., 1990. Effects of structural relaxation on cationic tracer diffusion in silicate melts. *Chemical Geology* 82, 209–216.
- Dingwell, D., 2006. Transport properties of magmas: diffusion and rheology. *Elements* 2, 281–286.
- Dingwell, D., Webb, S., 1989. Structural relaxation in silicate melts and non-newtonian melt rheology in geologic processes. *Physics and Chemistry of Minerals* 16, 508–516.
- Fenn, P., 1977. The nucleation and growth of alkali feldspars from hydrous melts. *Canadian Mineralogist* 15, 135–161.
- Freer, R., 1981. Diffusion in silicate minerals and glasses: A data digest and guide to the literature. *Contributions to Mineralogy and Petrology* 76, 440–454.
- Frisch, U., Hasslacher, B., Pomeau, Y., 1986. Lattice gas automata for the navier-stokes equations. *Physical Review Letters* 56, 1505–1508.
- Ghiorso, M., 1987. Chemical transfer in magmatic processes III: Crystal growth, chemical diffusion and thermal diffusion in silicate melts. *Contributions to Mineralogy and Petrology* 96, 291–313.
- Ghiorso, M., Carmichael, I., Rivers, M., Sack, R., 1983. The gibbs free-energy of mixing of natural silicate liquids - an expanded regular solution approximation for the calculation of magmatic intensive variables. *Contributions to Mineralogy and Petrology* 84 (2-3), 107–145.
- Ghiorso, M., Hirschmann, M., Reiners, P., Kress, V., 2002. The pMELTS: A revision of MELTS for improved calculation of phase relations and major element partitioning related to partial melting of the mantle to 3 Gpa. *Geochemistry, Geophysics, Geosystems* 3 (10.1029/2001GC000217).
- Gonnermann, H., Manga, M., 2003. Explosive volcanism may not be an inevitable consequence of magma fragmentation. *Nature* 426, 432–435.

- Granasy, L., Pusztai, T., Gyorgy, T., Warren, J., Douglas, J., 2005. Growth and form of spherulites. *Physical Review E* 72 (011605).
- Halter, W., Mysen, B., 2004. Melt speciation in the system $\text{Na}_2\text{O-SiO}_2$. *Chemical Geology* 213, 115–123.
- Hardy, E., Zygar, A., Zeidler, M., 2001. Isotope effect on the translational and rotational motion in liquid water and ammonia. *Journal of Chemical Physics* 114 (7), 3174–3181.
- Henderson, G., Calas, G., Stebbins, J., 2006. The structure of silicate glasses and melts. *Elements* 2, 269–273.
- Hess, P., 1995. Thermodynamic mixing properties and the structure of silicate melts. *Reviews in Mineralogy and Geochemistry* 32 (1), 147–189.
- Hofmann, A., Magaritz, M., 1977. Diffusion of Ca, Sr, Ba, and Co in a basalt melt: implications for the geochemistry of the mantle. *Journal of Geophysical Research* 82, 5432–5440.
- Holz, M., Mao, X., Seiferling, C., 1996. Experimental study of dynamic isotope effects in molecular liquids: Detection of translation-rotation coupling. *Journal of Chemical Physics* 104 (2), 669–679.
- Huang, F., Chakraborty, P., Lundstrom, C., Holmden, C., Glessner, J., Kieffer, S., Leshner, C., 2010. Isotope fractionation in silicate melts by thermal diffusion. *Nature* 464, 396–399.
- Huang, F., Lundstrom, C., Glessner, J., Ianno, A., Boudreau, A., Li, J., Ferré, E., Marshak, S., DeFrates, J., 2009. Chemical and isotopic fractionation of wet andesite in a temperature gradient: experiments and models suggesting a new mechanism of magma differentiation. *Geochimica et Cosmochimica Acta* 73, 729–749.
- Huber, C., Parmigiani, A., Chopard, B., Manga, M., Bachmann, O., 2008. Lattice boltzmann model for melting with natural convection. *International Journal of Heat and Fluid Flow* 29 (5), 1469 – 1480.
- Hui, H., Zhang, X., 2007. Toward a general viscosity equation for natural anhydrous and hydrous silicate melts. *Geochimica et Cosmochimica Acta* 71, 403–416.
- Judd, J., 1888. On the volcanic phenomena of the eruption, and on the nature and distribution of the ejected materials. part I. In: Symons, G. (Ed.), *The Eruption of Krakatoa*. Committee of the Royal Society. Harrison and Son, London, pp. 1–46.
- Keith, H., Padden, F., 1963. A phenomenological theory of spherulitic crystallization. *Journal of Applied Physics* 34 (8), 2409–2421.
- Keith, H., Padden, F., 1964a. Spherulitic crystallization from the melt. I. fractionation and impurity segregation and their influence on crystalline morphology. *Journal of Applied Physics* 35 (4), 1270–1285.

- Keith, H., Padden, F., 1964b. Spherulitic crystallization from the melt. II. influence of fractionation and impurity segregation on the kinetics of crystallization. *Journal of Applied Physics* 35 (4), 1286–1296.
- Kirkpatrick, R., 1975. Crystal growth from the melt: a review. *American Mineralogist* 60 (9-10), 798–814.
- Kress, V., Ghiorso, M., 1993. Multicomponent diffusion in MgO-Al₂O₃-SiO₂ and CaO-MgO-Al₂O₃-SiO₂. *Geochimica et Cosmochimica Acta* 57, 4453–4466.
- Kubicki, J., Muncill, G., Lasaga, A., 1990. Chemical diffusion in melts on the CaMgSi₂O₆-CaAl₂Si₂O₈ join under high pressures. *Geochimica et Cosmochimica Acta* 54, 2709–2715.
- Kyser, T., Leshner, C., Walker, D., 1998. The effects of liquid immiscibility and thermal diffusion on oxygen isotopes in silicate liquids. *Contributions to Mineralogy and Petrology* 133, 373–381.
- Langer, J., 1980. Instabilities and pattern formation in crystal growth. *Reviews of Modern Physics* 52 (1).
- Lee, S., Stebbins, J., 2006. Disorder and the extent of polymerization in calcium silicate and aluminosilicate glasses: O-17 NMR results and quantum chemical molecular orbital calculations. *Geochimica et Cosmochimica Acta* 70, 4275–4286.
- Leshner, C., 1986. Effects of silicate liquid composition on mineral-liquid element partitioning from Soret diffusion studies. *Journal of Geophysical Research* 91 (B6), 6123–6141.
- Leshner, C., 1990. Decoupling of chemical and isotopic exchange during magma mixing. *Nature* 344, 235–237.
- Leshner, C., 1994. Kinetics of sr and nd exchange in silicate liquids: Theory, experiments, and applications to uphill diffusion, isotopic equilibration, and irreversible mixing of magmas. *Journal of Geophysical Research* 99 (5), 9585–9604.
- Leshner, C., Walker, D., 1986. Solution properties of silicate liquids from thermal diffusion experiments. *Geochimica et Cosmochimica Acta* 50, 1397–1411.
- Lewis-Kenedi, C., Lange, R., Hall, C., Delgado-Grenados, H., 2005. The eruptive history of the Tequila volcanic field, western Mexico: ages, volumes, and relative proportions of lava types. *Bulletin of Volcanology* 67, 391–314.
- Liang, Y., 1994. Models and experiments for multicomponent chemical diffusion in molten silicates. Ph.D. thesis, University of Chicago.
- Liang, Y., Richter, F., Watson, E., 1996. Diffusion in silicate melts: II. Multicomponent diffusion in CaO-Al₂O₃-SiO₂ at 1500^{circ}c and 1 Gpa. *Geochimica et Cosmochimica Acta* 60 (24), 5021–5035.
- Lofgren, G., 1971a. Experimentally produced devitrification textures in natural rhyolite glass. *Geological Society of America Bulletin* 82, 553–560.

- Lofgren, G., 1971b. Spherulitic textures in glassy and crystalline rocks. *Journal of Geophysical Research* 76, 5635–5648.
- Lundstrom, C., 2009. Hypothesis for the origin of convergent margin granitoids and Earth's continental crust by thermal migration zone refining. *Geochimica et Cosmochimica Acta* 73, 5709–5729.
- MacArthur, A., Cas, R., Orton, G., 1998. Distribution and significance of crystalline, perlitic and vesicular textures in the Ordovician Garth Tuff (Wales). *Bulletin of Volcanology* 60, 260–285.
- Manley, C., 1992. Extended cooling and viscous flow of large, hot rhyolite lavas: implications of numerical modeling results. *Journal of Volcanology and Geothermal Research* 53, 27–46.
- Manley, C., Fink, J., 1987. Internal textures of rhyolite flows as revealed by research drilling. *Geology* 15, 549–552.
- Martin, M., McKinney, W., 1988. Spherulites in the Spring Branch Rhyolite, Western Saluda County, South Carolina. *South Carolina Geology* 32, 21–25.
- Martin, M., McKinney, W., 1998. The first synchrotron infrared beamlines at the advanced light source: Microspectroscopy and fast timing. *Proceedings of the Material Research Society* 524, 11.
- McLaughlin, E., 1960. Transport coefficient ratios for isotopically substituted molecules in the liquid phase and the transport mechanism. *Physica* 26, 650–652.
- McMillan, P., Wolf, G., 1995. Vibrational spectroscopy of silicate liquids. *Reviews in Mineralogy and Geochemistry* 32 (1), 247–315.
- Mills, R., Harris, K., 1976. The effect of isotopic substitution on diffusion in liquids. *Chemical Society Reviews* 5, 215–231.
- Mullins, W., Sekerka, R., 1963. Morphological stability of a particle growing by diffusion or heat flow. *Journal of Applied Physics* 34, 323–329.
- Mysen, B., Richet, P., 2005. *Silicate glasses and melts: Properties and structure*. Elsevier Press, 544 pages.
- Navrotsky, A., Ziegler, D., Oestrike, R., Maniar, P., 1989. Calorimetry of silicate melts at 1773 K: measurement of enthalpies of fusion and of mixing in the systems diopside-anorthite-albite and anorthite-forsterite. *Contributions to Mineralogy and Petrology* 101, 122–130.
- Newman, S., Stolper, E., Epstein, S., 1986. Measurement of water in rhyolitic glasses: calibration of an infrared spectroscopic technique. *American Mineralogist* 71, 1527–1541.
- Qian, Y., D'Humières, D., Lallemand, P., 1992. Lattice BGK models for the Navier-Stokes equation. *Europhysics Letters* 17, 479–484.

- Richter, F., Davis, A., DePaolo, D., Watson, E., 2003. Isotope fractionation by chemical diffusion between molten basalt and rhyolite. *Geochimica et Cosmochimica Acta* 67, 3905–3923.
- Richter, F., Liang, Y., Davis, A., 1999. Isotope fractionation by diffusion in molten oxides. *Geochimica et Cosmochimica Acta* 63, 2853–2861.
- Richter, F., Mendybaev, R., Christensen, J., Hutcheon, I., Williams, R., Sturchio, N., 2006. Kinetic isotope fractionation during diffusion of ionic species in water. *Geochimica et Cosmochimica Acta* 70 (2), 277–289.
- Richter, F., Watson, E., Mendybaev, R., Dauphas, N., Georg, B., Watkins, J., Valley, J., 2009. Isotopic fractionation of the major elements of molten basalt by chemical and thermal diffusion. *Geochimica et Cosmochimica Acta* 73, 4250–4263.
- Richter, F., Watson, E., Mendybaev, R., Teng, F., Janney, P., 2008. Magnesium isotope fractionation in silicate melts by chemical and thermal diffusion. *Geochimica et Cosmochimica Acta* 72, 206–220.
- Riehle, J., Miller, T., Bailey, R., 1995. Cooling, degassing and compaction of rhyolitic ash flow tuffs: a computational model. *Bulletin of Volcanology* 57, 319–336.
- Rothman, S., Peterson, N., 1965. Isotope effect and divacancies for self-diffusion in copper. *Physica Status Solidi* 35 (1), 305–312.
- Ryan, M., Sammis, C., 1981. The glass transition in basalt. *Journal of Geophysical Research* 86, 9515–9535.
- Schoen, A., 1958. Correlation and the isotope effect for diffusion in crystalline solids. *Physical Review Letters* 1 (4), 138–140.
- Skulan, J., DePaolo, D., Owens, T., 1997. Biological control of calcium isotopic abundances in the global calcium cycle. *Geochimica et Cosmochimica Acta* 61, 2505–2510.
- Smith, R., Tremallo, R., Lofgren, G., 2001. Growth of megaspherulites in a rhyolitic vitrophyre. *American Mineralogist* 86, 589–600.
- Stebbins, J., 1995. Dynamics and structure of silicate and oxide melts; nuclear magnetic resonance studies. *Reviews in Mineralogy and Geochemistry* 32 (1), 191–246.
- Stevenson, R., Briggs, R., Hodder, A., 1994. Physical volcanology and emplacement history of the Ben Lomond rhyolite lava flow, Taupo Volcanic Centre, New Zealand. *New Zealand Journal of Geology and Geophysics* 37, 345–358.
- Stolper, E., 1982. Water in silicate glasses: An infrared spectroscopic study. *Contributions to Mineralogy and Petrology* 81, 1–17.
- Succi, S., 1991. *The lattice boltzmann Equation, for Fluid Dynamics and Beyond*. Oxford University Press, London, 288 pages.

- Swanson, S., 1977. Relation of nucleation and crystal-growth rate to the development of granitic textures. *American Mineralogist* 62, 966–978.
- Swanson, S., Naney, M., Westrich, H., Eichelberger, J., 1989. Crystallization history of Obsidian Dome, Inyo Domes, California. *Bulletin of Volcanology* 51, 161–176.
- Trial, A., Spera, F., 1994. Measuring the multicomponent diffusion matrix: Experimental design and data analysis for silicate melts. *Geochimica et Cosmochimica Acta* 58 (18), 3769–3783.
- Watkins, J., DePaolo, D., Huber, C., Ryerson, F., 2009. Liquid composition-dependence of calcium isotope fractionation during diffusion in molten silicates. *Geochimica et Cosmochimica Acta* 73 (24), 7341–7359.
- Watson, E., 1982. Basalt contamination by continental crust: Some experiments and models. *Contributions to Mineralogy and Petrology* 80, 83–87.
- Watson, E., Muller, T., 2009. Non-equilibrium isotopic and elemental fractionation during diffusion-controlled crystal growth under static and dynamic conditions. *Chemical Geology* 267, 111–124.
- Watson, E., Wark, D., Price, J., Van Orman, J., 2002. Mapping the thermal structure of solid-media pressure assemblies. *Contributions to Mineralogy and Petrology* 142, 640–652.
- Weingartner, H., Holz, M., Sacco, A., Trotta, M., 1989. The effect of site-specific isotopic substitutions on transport coefficients in liquid methanol. *Journal of Chemical Physics* 91 (4), 2568–2574.
- Westrich, H., Stockman, H., Eichelberger, J., 1988. Degassing of rhyolitic magma during ascent and emplacement. *Journal of Geophysical Research* 93, 6503–6511.
- Zhang, X., 2008. *Geochemical Kinetics*. Princeton University Press, 631 pages.
- Zhang, Y., Behrens, H., 2000. H₂O diffusion in rhyolitic melts and glasses. *Bulletin of Volcanology* 169, 243–262.
- Zhang, Y., Belcher, R., Ihinger, P., Wang, L., Xu, Z., Newman, S., 1997. New calibration of infrared measurement of dissolved water in rhyolitic glasses. *Geochimica et Cosmochimica Acta* 63 (15), 3089–3100.